國立臺灣大學理學院地質科學系

碩士論文

Department of Geosciences

College of Science

National Taiwan University

Master Thesis

多種類指標重建全新世古環境變化:以台南科學園區為例

Multi-proxy reconstruction of Holocene paleo-environmental changes: Examples from the Tainan Science Park region

楊翔宇

Hsiang-Yu Yang

指導教授：羅 立 博士

Advisor: Li Lo, Ph.D.

中華民國 112 年 8 月

August 2023

doi:10.6342/NTU202302306

國立臺灣大學碩士學位論文
口試委員會審定書
MASTER'S THESIS ACCEPTANCE CERTIFICATE
NATIONAL TAIWAN UNIVERSITY

多種類指標重建全新世古環境變化:以台南科學園區為例

Multi-proxy reconstruction of Holocene paleo-environmental changes: Examples from the Tainan Science Park region

本論文係 楊翔宇（R10224212）在國立臺灣大學 地質科學研究所 完成之碩士學位論文，於民國 112 年 07 月 03 日承下列考試委員審查通過及口試及格，特此證明。

The undersigned, appointed by the Department / Institute of Geoscience on 03.07.2023 have examined a Master's thesis entitled above presented by Hsiang Yu Yang (R10224212) candidate and hereby certify that it is worthy of acceptance.

口試委員 Oral examination committee:

（指導教授 Advisor）

doi:10.6342/NTU202302306

致謝

我一直都覺得如果我是果實能力者的話，我應該是吃到貴人果實。謝謝你們對我的支持，讓我對於任何挑戰都有信心能達成；也謝謝你們的陪伴，提醒我不能忘記生活享受過程。最後，也謝謝我自己，應該是沒有太讓各位失望吧哈哈哈。

首先感謝的是我的家人，放任我把家裡餐桌的椅子全部都丟滿我的衣物(我收完了)，並給予我相當大的生活空間可以享受這段過程。而你們也總是適時的給我意見，並鼓勵我不要害怕犯錯，我想我長大也想成為這樣的父母，謝謝你們。

再來感謝的當然是這兩年願意花時間指導我包容我的羅立老師，給予我一個在計畫中學習的機會，讓我看到身為一個研究者的熱情以及視野，也讓我知道身為計畫人員所要背負的責任與義務。很謝謝老師在討論的過程中時不時塞一些我從沒想過的觀念，跟老師不管是討論研究或是未來每次都讓我滿載而歸。也很謝謝老師的教導可以讓我在研究以外的事也能以正確的心態面對。

接著謝謝在研究上幫助我的郁豫學姐、峻誌學長、依璇學姐、韋竹學姐、包包學姊、翊展學長、伯鈞學長、淑俐學姐、子惟學長，還有南科計劃的柏霖跟書屹，真的很謝謝你們的幫助，沒有你們的協助我的實驗不可能這麼順利。吃飯好快樂的 Lancer 組、領巾沒到齊過的 Loop 團、實驗室的好夥伴易辰洪毅婉彤、系籃的浩庭易諭政熹崇毓等等、學術生涯一直幫我的童學姊、腦力激盪丟梗的子桓，還有特別是在碩二開始出現在羅斯福路，讓我每個禮拜都能回味大學生活時光的科維跟紅蟳，還有好多好多人，謝謝大家沒有讓我變成無聊的人。

最後謝謝蘭達，我想這個階段沒有妳我無法完成。而我們之後也還有許多要一起完成的計劃，希望再次回首時這裡已經是一個小點了，再請妳多多指教拉。

很開心終於到了一個存檔點，這是我目前求學生涯中最棒的一趟旅程，心境隨時都在轉變，時間上從一個月前到變兩天前的決定可以做得更好。這條路上我曾經以為摩托車夠用了，但當開始開車之後我才發現有飛機的影子。而曾經設立的目標已經變成過程，我會帶著這些善意往前走向下個目標，在這條路上繼續享受旅途。

doi:10.6342/NTU202302306

中文摘要

自全新世以來，台灣西南部的海岸線快速地變遷，廣闊的嘉南平原所保存的沉積物不僅紀錄了環境變遷的歷史，甚至可以在其東側的台南科學園區一帶發掘出距今 4800 年以來豐富的人類活動。而了解人類與環境相互作用之間複雜的關係對於幫助人類社會應對當前氣候變化的影響至關重要。本研究使用鑽探於台南科學園區西側的五根沉積物岩芯（50-100 米，回收率>95%）與多種類沉積物-地球化學指標來建立早全新世以來台南科學園區一帶的環境變遷紀錄，透過加速器質譜儀碳十四定年建立年代框架後，進行 1 毫米解析度的 X 光螢光分析（X-ray fluorescence, XRF）為岩芯提供高解析度的元素組成資訊，並配合岩相分析來區分不同的沉積環境。此外，岩芯沉積物中所測得的總有機碳（total organic carbon, TOC）、總氮（total nitrogen, TN）、碳酸鈣含量與粒徑分析也同時一起進行後續的討論。

我們發現 Log(Ca/Ti)可以作為指示海相沉積環境的代用指標，與總無機碳（碳酸鈣含量）呈現良好的相關性（$r = 0.64, p < 0.0001$）。而 Log(Zr/Rb)則是與沉積物粒徑組成有著良好的相關性。其中，泥（$r = -0.69, p < 0.0001$）和粉砂（$r = -0.72, p < 0.0001$）有著顯著的負相關性，另外與砂（$r = 0.76, p < 0.0001$）也有著強烈的正相關。其中在五根岩芯中皆出現了 Log(Ca/Ti)的平穩的訊號，指示出了一段從 9300 到 7300 年前的穩定海相沉積環境，推測為可能代表早全新世海進時期的溢浪三角洲相。除此之外，較高的 TOC/TN 也可以被發現在富含有機質的細顆粒泥質沉積物中，提供判斷沼澤相很好的依據。

早全新世以來的古河口-濱海沉積環境可以被此研究中的多種類指標健全地重建。XRF 元素對數比可以以非破壞性的方式獲得建立環境指標，元素分析和雷射粒徑分析則可以得到特定層位的組成信息。因此，一個全面的沉積相判識方法可以透過與岩相相互驗證後被確立，並提供此地區後續研究可以被進行比對的參考。

關鍵詞：中全新世、沉積相、XRF 岩心掃描、環境代用指標、台江內海

doi:10.6342/NTU202302306

Abstract

Since the Holocene, the coastline of southwestern Taiwan has undergone rapid changes, and the sediment deposits preserved in the extensive Chianan Plain not only record the history of environmental changes but also reveal rich human activities from 4,800 cal BP in the Tainan Science Park region. Disentangling the complex relationship between humans and the environment is crucial for helping human society respond to the impacts of current climate change. Five long and continuous sedimentary cores (50-100 m penetration with >95% recovery rate) from the newly developed Tainan science park region have been retrieved in this study. We aim to apply multi-proxy methods to provide comprehensive environmental information in Tainan science park region since the early Holocene. The 1-millimeter resolution X-ray fluorescence (XRF) element profile offered enriched compositional information in the sediment cores that can support the lithofacies analysis to distinguish different sedimentary environments. Besides, the sedimentary composition of total organic carbon (TOC), total nitrogen (TN), and grain size analyses are applied with a well-established age model based on accelerator mass spectrometry radiocarbon dating.

We find Ca/Ti ratio can serve as an indicator of the marine environment, which also has a positive correlation with the total inorganic carbon, which can represent the calcium carbonate content ($r = 0.64$, $p < 0.0001$). While the Zr/Rb proxy is linked with the

doi:10.6342/NTU202302306

variation of grain sizes, showing a significant negative correlation with clay ($r = -0.69$, $p < 0.0001$), silt ($r = -0.72$, $p < 0.0001$), and a positive correlation with sand ($r = 0.76$, $p < 0.0001$). Relatively constant Ca/Ti ratio in these five cores suggests a stable marine sediment supply during 9.3-7.3 kyr BP, which is inferred to represent washover fan facies during a transgressive phase. Furthermore, higher TOC/TN ratios are found in organic-rich fine-grained mud sediments, providing a reliable indicator for identifying marsh and lagoon facies.

The early Holocene paleo-estuarine to nearshore depositional environment can be robustly reconstructed using the multi-proxy employed in this study. XRF logarithm ratios offer non-destructive method to establish environmental proxy, while elemental and grain size analyses provide compositional information for specific intervals. Therefore, a comprehensive sedimentary facies identification method can be established through cross-validation with lithofacies data, offering a comparable reference for other research in this region.

Keywords: Middle Holocene, Sediment facies, XRF core scanning, Environmental proxies, Taijiang Inner Sea

doi:10.6342/NTU202302306

Contents

doi:10.6342/NTU202302306

doi:10.6342/NTU202302306

Figures

doi:10.6342/NTU202302306

doi:10.6342/NTU202302306

doi:10.6342/NTU202302306

Tables

doi:10.6342/NTU202302306

1 Introduction

1.1 The interaction between rapid environmental changes and prehistoric humans since the middle Holocene

The coastal region around the world has been early-developed and densely populated, for example, the population settled in Mekong Delta is larger than 20 million(Erban et al., 2014). Moreover, in the United States, property valued at over one trillion dollars is situated within around 215 m of the coastline (Fleming et al., 2018). However, the changeable climate change in recent years urges these low-lying coastal communities to take more comprehensive information to address rising sea levels (Neumann et al., 2015) and other impacts of climate change.

The Chianan Plain, located in southwestern Taiwan coastal plain with no exception, is the largest plain in the country, encompassing approximately one-seventh of Taiwan's population. Not only that, this region began to exhibit traces of prehistoric human habitation around 6000 years ago. Numerous archaeological sites ranging from the Neolithic period to the 17th and 18th centuries have been discovered in the vicinity of the Tainan Science Park (Tsang et al., 2004; Tsang et al., 2007). These sites not only inform us about the suitability of this area for human settlement in the past but also reflect how prehistoric humans adapted to the rapid coastline changes since the mid-Holocene. In

doi:10.6342/NTU202302306

essence, understanding the interaction between human societies and the paleoenvironment is indispensable to address the challenges faced by coastal regions today.

According to the archaeological site distribution and the geology study (Sun, 1964; Chen, 1993; Huang, 2001; Chen et al., 2004), environmental changes can be divided into 4 stages (Kaim et al., 2010). The first stage was the bay-forming stage around 6000 to 5000 BP (Figure 1.1), the continuously rising sea level reached the Xinhua Hills, the whole southwestern Taiwan was covered by seawater. People of the early Neolithic Tapengkeng Culture had already arrived in the southwestern coastal region, with settlements mostly located near the hills.

During the second stage, the coastline was moving stably westward around 5000 to 4000 BP (Figure 1.2), people had more living space due to the expansion of the coastal plain. During this period, the dominant culture is known as the Niuchoutzu culture. However, in the northern region of the Zengwen River, there is an area where the cultural characteristics slightly differ from the Niuchoutzu culture. Scholars have tentatively referred to this phase as the Red Cord-marked Pottery phase. Additionally, due to the activity of the Hsiaokangli Fault, the Tainan Plain has gradually uplifted, forming the ancient Tainan Island.

doi:10.6342/NTU202302306

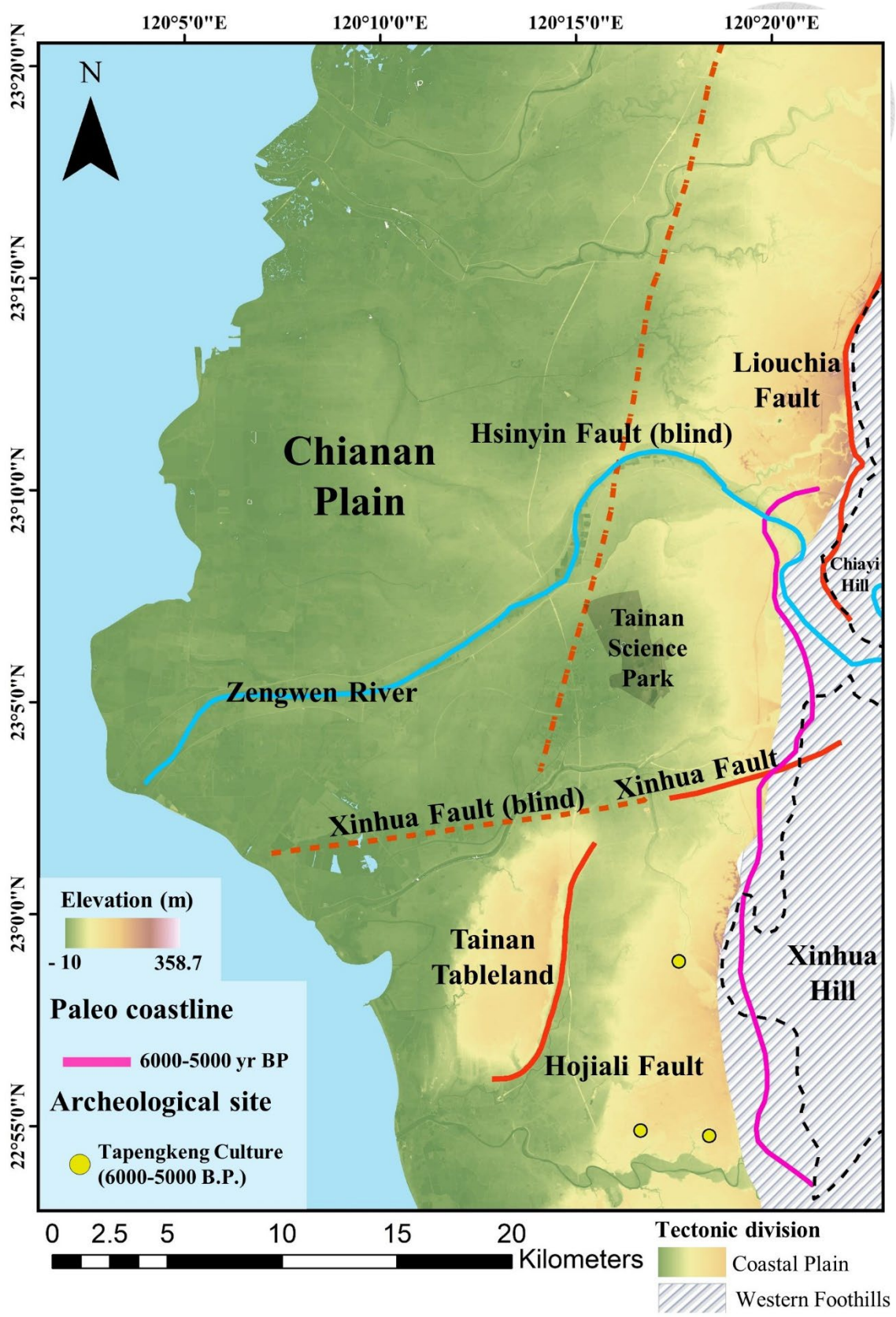

Figure 1.1 During the first stage, the coastline transformation and the distribution of archaeological site. The tectonic divisions are adopted from Yu et al. (1997), a 5 m

doi:10.6342/NTU202302306

resolution digital elevation model (DEM) provided by Satellite Survey Center (SSC) is utilized to represent the elevation changes in the Coastal Plain, while diagonal textures are used to distinguish the Western Foothills. The terrain is further subdivided into Chianan Plain, Xinhua Hill, and Chiayi Hill, following the classification provided by the Information of Land Subsidence Prevention in Taiwan. The data for the Zengwen River is provided by the Water Resources Agency, Ministry of Economic Affairs (MOEA), and is represented by light blue lines. The fault locations are adopted from Chen et al. (2004) and depicted in red lines (dashed lines indicating blind faults). The black polygon represents the present Tainan Science Park. Additionally, the location of Tainan Tableland, the 6000-5000 cal BP coastline is represented by pink line, and yellow points represent the distribution of Tapenkeng archaeological sites are adopted from Kaim et al. (2010).

doi:10.6342/NTU202302306

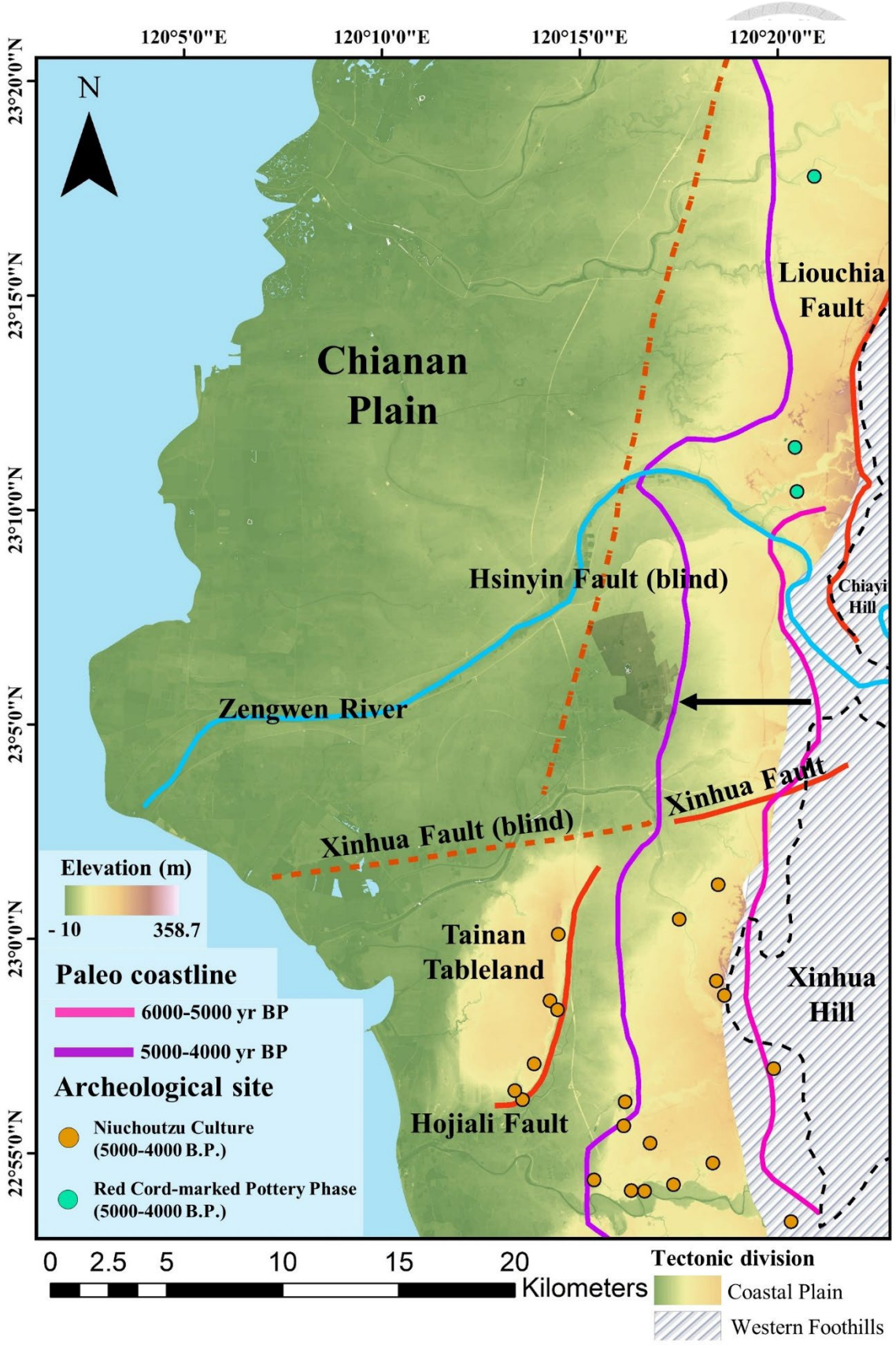

Figure 1.2 During the second stage, the coastline transformation and the distribution of

doi:10.6342/NTU202302306

archaeological site. The tectonic divisions are adopted from Yu et al. (1997), a 5 m resolution DEM provided by SSC is utilized to represent the elevation changes in the Coastal Plain, while diagonal textures are used to distinguish the Western Foothills. The terrain is further subdivided into Chianan Plain, Xinhua Hill, and Chiayi Hill, following the classification provided by the Information of Land Subsidence Prevention in Taiwan. The data for the Zengwen River is provided by the Water Resources Agency, MOEA, and is represented by light blue lines. The fault locations are adopted from Chen et al. (2004) and depicted in red lines (dashed lines indicating blind faults). The black polygon represents the present Tainan Science Park. Additionally, the location of Tainan Tableland, the 6000-5000 cal BP coastline is represented by pink line, the 5000-4000 cal BP coastline is represented by purple line, the orange points and points in aqua color each represent the distribution of Niuchoutzu and Red Cord-marked Pottery Phase archaeological sites are adopted from Kaim et al. (2010).

doi:10.6342/NTU202302306

The third stage was the Taijiang Inland Sea formed around 3000 to 2000 BP (Figure 1.3), the sediment carried by the Tsengwen River formed a delta that separated the former inner bay into two inland seas, and the Taijiang Inland Sea was south of Tsengwen River. The archaeological site of this Tahu Culture period was concentrated in the current Tainan Science Park, which was located on the edge of the ancient Taijiang Inland Sea, and there were also shell mounds accumulated by a large number of shellfish in the site, which shows the use of sea resources by the prehistoric people.

The fourth stage was the stable period of the Taijiang Inland Sea from around 2000 BP to the 17th and 18th centuries (Figure 1.4), the coastline remained stable and was located near the Hsinyin Fault just like stage three, indicating that the sediment supply rate did not exceed the subsidence rate of the coastal plain on the footwall. The culture during this stage was the Niaosung Culture, which exhibited a distribution similar to that of the Tahu Culture due to the relatively stable coastline(Chen et al., 2004).

doi:10.6342/NTU202302306

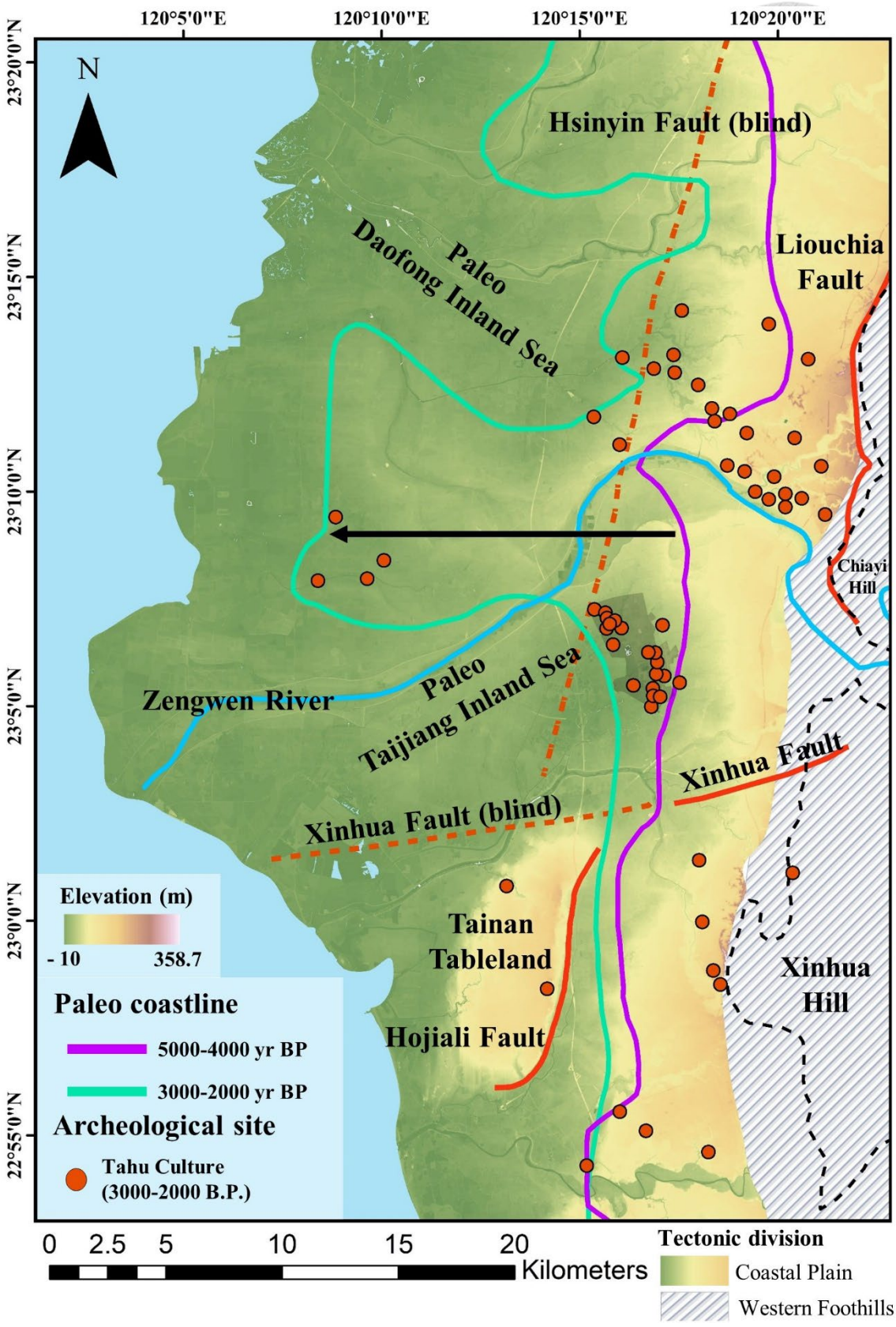

Figure 1.3 During the third stage, the coastline transformation and the distribution of archaeological site. The tectonic divisions are adopted from Yu et al. (1997), a 5 m

doi:10.6342/NTU202302306

resolution DEM provided by SSC is utilized to represent the elevation changes in the Coastal Plain, while diagonal textures are used to distinguish the Western Foothills. The terrain is further subdivided into Chianan Plain, Xinhua Hill, and Chiayi Hill, following the classification provided by the Information of Land Subsidence Prevention in Taiwan. The data for the Zengwen River is provided by the Water Resources Agency, MOEA, and is represented by light blue lines. The fault locations are adopted from Chen et al. (2004) and depicted in red lines (dashed lines indicating blind faults). The black polygon represents the present Tainan Science Park. Additionally, the location of Tainan Tableland, the 5000-4000 cal BP coastline is represented by purple line, the 3000-2000 cal BP coastline is represented by cyan line, the red points represent the distribution of Tahu archaeological sites are adopted from Kaim et al. (2010).

doi:10.6342/NTU202302306

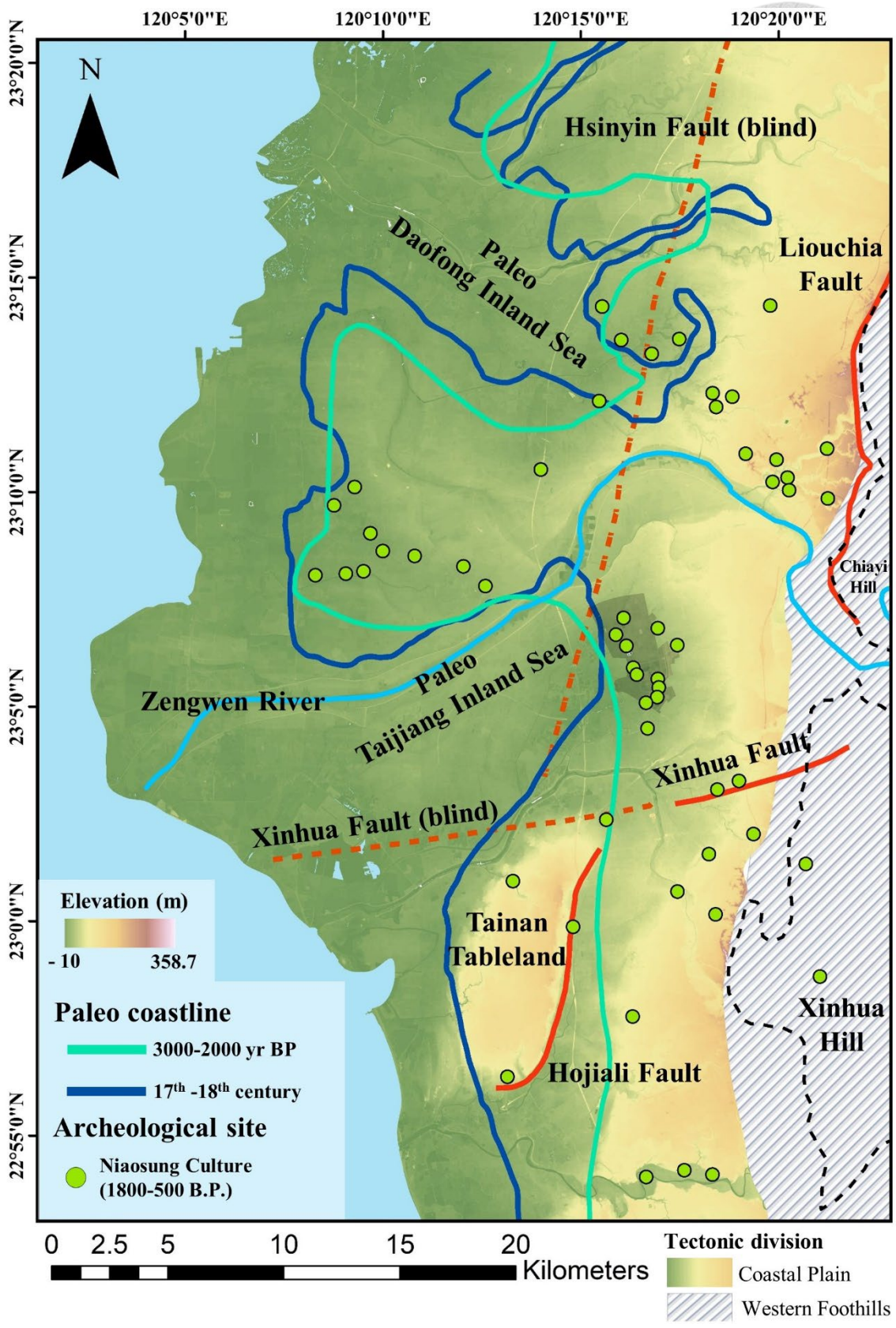

Figure 1.4 During the fourth stage, the coastline transformation and the distribution of archaeological site. The tectonic divisions are adopted from Yu et al. (1997), a 5 m

doi:10.6342/NTU202302306

resolution DEM provided by SSC is utilized to represent the elevation changes in the Coastal Plain, while diagonal textures are used to distinguish the Western Foothills. The terrain is further subdivided into Chianan Plain, Xinhua Hill, and Chiayi Hill, following the classification provided by the Information of Land Subsidence Prevention in Taiwan. The data for the Zengwen River is provided by the Water Resources Agency, MOEA, and is represented by light blue lines. The fault locations are adopted from Chen et al. (2004) and depicted in red lines (dashed lines indicating blind faults). The black polygon represents the present Tainan Science Park. Additionally, the location of Tainan Tableland, the 3000-2000 cal BP coastline is represented by cyan line, the 17^{th}-18^{th} century coastline is represented by blue line, the lime points represent the distribution of Niaosung archaeological sites are adopted from Kaim et al. (2010).

doi:10.6342/NTU202302306

1.2 The aim of this study

The geographical location of the Tainan Science Park and the abundance of archaeological sites in the area both indicate the research potential within the rapidly deposited sediments during the Holocene. However, previous studies have primarily focused on observing the entire Chianan Plain region (Huang, 2001; Chen et al., 2004; Kaim et al., 2010, Yang, 2016), lacking high-resolution data specifically for the Tainan Science Park. Furthermore, this region also requires high-resolution sediment core analysis methods to further reconstruct the paleoenvironments.

This study utilizes five selected long cores from the area of the Tainan Science Park AO region drilling project for 1 mm X-ray fluorescence (XRF) scanning to obtain non-destructive, high-resolution elemental signals. Combined with total organic carbon (TOC), total nitrogen (TN), and grain size analysis, a multi-proxy method is employed to assist lithofacies analysis and identify different sedimentary facies. The aim is to reconstruct the complex environmental changes in this area with finer data and a more comprehensive perspective, establishing a record of paleoenvironmental changes since the mid-Holocene.

doi:10.6342/NTU202302306

2 Literature Review

2.1 The application of XRF analysis in environmental science

XRF core scanners have rapidly advanced, widely used in Earth and environmental sciences in the past two decades. Their non-destructive and high-resolution characteristics have allowed researchers to scale down their investigations to annual or even sub-annual resolutions (Rothwell et al., 2015b). Two of the most commonly used core scanning instruments are AVAATECH and ITRAX (Rothwell et al., 2015a). In this study, the ITRAX core scanner is utilized. It combines elemental signals with optical and radiographic images, providing a more intuitive approach to studying sedimentary materials (Croudace et al., 2006).

However, there are limitations in using the raw data because the elemental intensities are obtained solely by scanning the surface of the core. This is different from the quantitative concentrations obtained through techniques such as mass spectrometry (Gregory et al., 2019). Factors such as matrix effects, which result from the mutual interference between elements caused by the variable water content or organic matter (Franzini et al., 1972; Kido et al., 2006; Löwemark et al., 2011), as well as specimen effects arising from sample inhomogeneity and undulating sample elevations (Hennekam & De Rick, 2012), all indicate the uncertainties associated with semi-quantitative measurements. Therefore, these raw data need to be corrected or calibrated (Longman et al., 2019; Zhang et al.,

doi:10.6342/NTU202302306

2020).

The purpose of calibration is to convert the intensity into concentrations (Weltje & Tjallingii, 2008). Previous calibration equations (De Vries & Vrebos, 2002) used for single-element conversion included uncertainties related to specimen effects, requiring further quantitative analytical methods for more robust calibration. Fortunately, the advances in statistical interpretation of compositional data (Aitchison, 1982; Aitchison & Egozcue, 2005) allow us to perform log-ratio calibration as a proxy to obtain relative concentrations (Equation 1). In this log-ratio calibration eauqtion, W_{ij} represents the weight proportion (concentration) of element j in specimen i, and W_{iD} represents the concentration composition of specimen i consisting of D elements. I_{ij} represents the intensity of element j in specimen i, and I_{iD} represents the intensity composition of specimen i consisting of D elements. α & β means the empirical calibration coefficient, representing the matrix effect and detection efficiency in XRF scanning. Therefore, this log-ratio intensity transform can provide the relative changes in the chemical concentration (Weltje & Tjallingii, 2008; Weltje et al., 2015).

$$\ln\left(\frac{W_{ij}}{W_{iD}}\right) = \alpha_{jD} \ln\left(\frac{I_{ij}}{I_{iD}}\right) + \beta_{jD} \quad (1)$$

Since these proxies typically do not have universal standards, they can vary depending on the region (Bloemsma et al., 2012). For example, there is a unique situation in West Africa where Fe/Ti can be used to differentiate sediment sources. In this region,

doi:10.6342/NTU202302306

Ti represents the dust from the Sahara Desert, while changes in hydrology can be identified through variations in Fe (Itambi et al., 2010). Therefore, it is necessary to understand the role of elements in the environment and utilize statistical methods such as principal component analysis to enhance the applicability of these geochemical proxy as environmental indicators (Weltje et al., 2015; Croudace et al., 2019; Mark et al., 2022).

Looking at the application of Ca in different study regions, it can be a significant indicator for marine environments. Rothwell et al. (2006) found a strong correlation between Ca and particles larger than 32 μm, suggesting a possible link between Ca and the presence of foraminifera. Wolters et al. (2010) compared XRF results with pollen experiments and found that the increased Ca in perimarine wetlands was not only related to calcium carbonate but also synchronized with an increase in reed taxa in the pollen record, representing the initial marine conditions. Richter et al. (2006) differentiated lithostratigraphic units by the relative abundance of Ca and Fe, representing biogenic calcium carbonate and terrigenous sediment, respectively.

Ti can indicate terrestrial sediment in the lithostratigraphic record. Harff et al. (2011) observed an increase in Ti in the Baltic Sea Basin when more terrigenous sediments entered the basin. This increase could be further explained as different sedimentary facies through combining with lithology and diatom analysis. In coastal lakes, Balascio et al. (2011) found that Ti could be used as an indicator of detrital input, with peaks appearing

doi:10.6342/NTU202302306

predominantly in clay minerals, and categorized as PC1 in principal component analysis (PCA).

The association of Ca with marine environments and the regional background values indicated by Ti (Cohen, 2003) make Ca/Ti a suitable proxy for observing variations in biogenic calcium carbonate. In addition, other elements suitable for normalization, like Al and Fe, are sometimes limited in practical applicability due to insufficient recorded counts of Al (Davies et al., 2015) and the influence of redox conditions and diagenetic processes on the geochemical behavior of Fe (Boyle, 2001). Therefore, the use of stable Ti is more effective (Shala et al., 2014). Ingram et al. (2010) compared Ca/Ti with nannofossil biostratigraphy and identified different layers, observing that higher Ca/Ti coincides with a greater abundance of calcareous fossils. Kylander et al. (2011) also suggested that Ca/Ti can serve as an indicator of carbonate precipitation.

Another proxy, Zr/Rb,is often used to indicate variations in grain size (Turner et al., 2015). This is because Rb tends to occur in clay minerals with finer grain sizes (Dypvik & Harris, 2001), while Zr is typically associated with coarser particles (Chen et al., 2006; Kylander et al., 2011). Additionally, Rb can be used as a normalizing element (Davies et al., 2015). Zr/Rb finds wide application in different environments. Chen et al. (2006) demonstrated the potential of Zr/Rb as a proxy for winter monsoon intensity on the Loess Plateau, showing similar variations to the mean grain size of quartz particles (MGSQ)

doi:10.6342/NTU202302306

and indicating specific loess-paleosol sequences. Wang et al. (2011) used the increasing values of Zr/Rb to indicate recorded flood events in river sediments due to the influx of coarser particles during floods. Chawchai et al. (2013) found correlations between Zr and coarser grains, suggesting that the increase in Zr/Rb was related to higher runoff and rainfall, resulting in the transport of more coarse particles into lakes. Wu et al. (2020) compared Zr/Rb with inductively coupled plasma-mass spectrometry (ICP-MS) in a Southern Ocean sediment core and found a good correlation, with lower values during glacials and higher values during interglacials.

Therefore, based on the robust proxy comparisons and their applicability to the environment, this study will use Ca/Ti and Zr/Rb as proxies to observe the influence of marine and terrestrial environments as well as variations in grain size in the study area.

2.2 Geological background

The Tainan Science Park is located on the eastern side of the Chianan Plain in southwestern Taiwan, and it belongs to the alluvial plain along the southern bank of the Tsengwen River. The eastern side is adjacent to the Xinhua Hills and Chiayi Hills, and it is close to the Western Foothills, resulting in higher terrain. The western side is adjacent to the Tainan Terrace and the paleo Taijiang Inland Sea, presenting lower terrain. The northern side is influenced by sediments carried by the Tsengwen River, leading to rapid accumulation and higher elevation. The topography of the area shows higher terrain on

doi:10.6342/NTU202302306

the eastern, northern, and southern sides, with lower terrain on the western side, resembling a scoop-shaped morphology. Therefore, the rivers mostly flow westward from the surrounding areas, causing the water systems to have a northeast-southwest orientation, forming parallel river systems that converge and flow southwest into the paleo Taijiang Inland Sea (Figure 2.1). However, many of the river channels have been improved and regulated, and some no longer follow their original course (Chen et al., 2004b). The interpretation of old river channels often relies on the Taiwan maps from the Japanese Occupation Period.

The sea level in our study area had gradually risen due to climate warming since the last glacial period, consistent with global trends (Chen & Liu, 1996). Around 6000 cal BP, the sea level had already reached a level close to the recent and remained stable (Rohling et al., 1998; Church et al., 2001). Additionally, previous studies based on aerial photography, stratigraphic comparison, and abandoned river channels suggest that the Chianan Plain has experienced two episodes of marine transgression and regression since the Holocene, known as the Tainan Phase and the Tahu Phase (Sun, 1964, 1970). By analyzing the locations of shell mounds and radiocarbon dating, it has been determined that the earlier Tainan Phase transgression occurred between 6500 and 5000 cal BP, during which the sea level reached approximately 35-40 meters above the present contour, around the Xinhua and Danei areas. Subsequently, the sea level receded westward until

doi:10.6342/NTU202302306

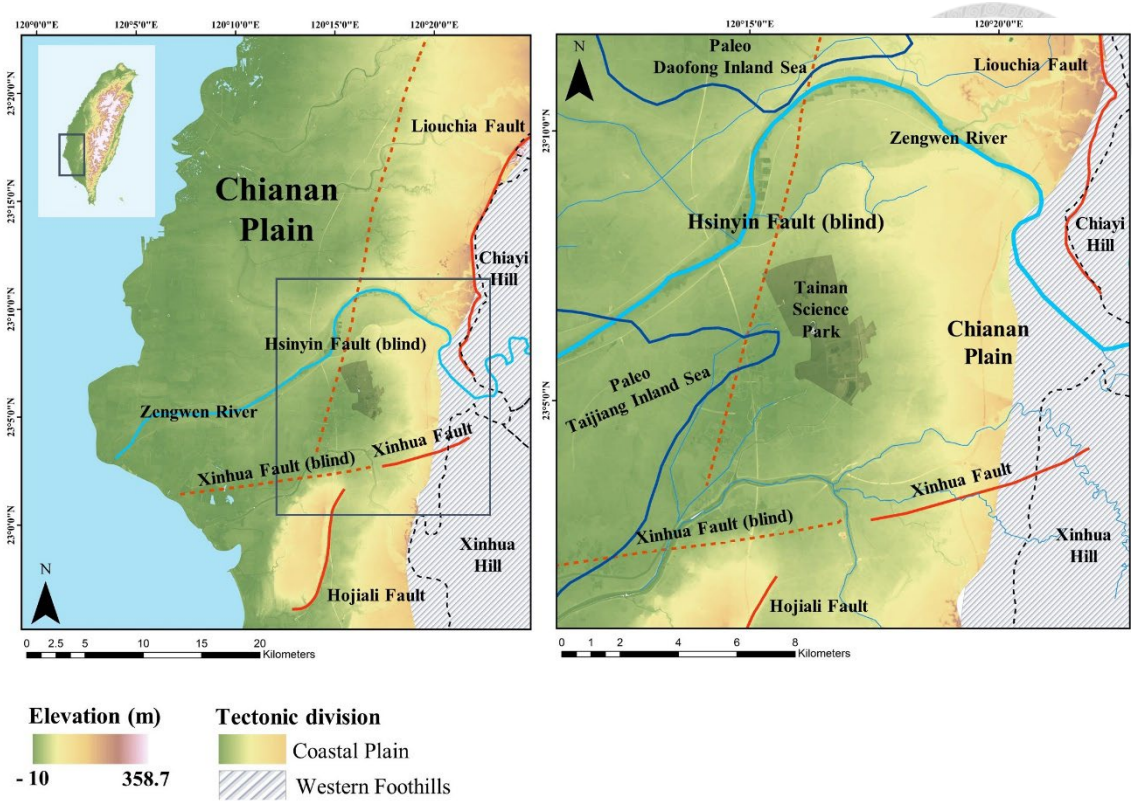

Figure 2.1 Geographic setting of Tainan Science Park. The tectonic divisions are adopted from Yu et al. (1997), a 5 m resolution DEM provided by SSC is utilized to represent the elevation changes in the Coastal Plain, while diagonal textures are used to distinguish the Western Foothills. The terrain is further subdivided into Chianan Plain, Xinhua Hill, and Chiayi Hill, following the classification provided by the Information of Land Subsidence Prevention in Taiwan. River data is provided by the Water Resources Agency, MOEA, and Zengwen River is represented by the light blue bold lines. The fault locations are adopted from Chen et al. (2004) and depicted in red lines (dashed lines indicating blind faults). The black polygon represents the present Tainan Science Park. In addition, the boundary of Taijiang Inland Sea and Daofong Inland sea are adopted from Chang et al. (1996).

doi:10.6342/NTU202302306

approximately 4000-3500 cal BP when it rose again due to global warming, leading to the so-called Tahu Phase transgression. The coastline of this transgression was situated around the Dalin, Minxiong, Chiayi, Dongshan, Madou, Jiali, Anding, and Shanhua areas, with a contour elevation of approximately 7-10 meters (Lin, 1961, 1966). However, the viewpoint of these two transgressive and regressive episodes continues to be debated. Chen (1993) based on geological drilling and core stratigraphy analysis, and by comparing new radiocarbon dating data, proposed that there has been only one transgression and regression since the Holocene. According to this view, the eastern transgression of the Tainan area began approximately 10,000 cal BP and ended around 6500 cal BP. Huang (2001) through analysis of sedimentary sequences in the Chianan Plain area, concluded that from approximately 9000 to 7000 cal BP, the entire Chianan Plain was part of a larger estuary system and subsequently experienced ongoing landward processes for the following 7000 years. Yang (2016) through an environmental comparison of the southern section of the Yun-Chia-Nan Plain (south of Jishuei River to the north of Yanshuei River), discovered that approximately 9500 cal BP, this region had already reached its maximum marine inundation, 1000 years earlier than the central section of the Yun-Chia-Nan Plain (south of Puzih River to the north of Tsengwen River). It is suggested that this discrepancy is due to the slower increase rate of sedimentary space compared to the supply rate of sediment from the Zengwen River, pointing out the

doi:10.6342/NTU202302306

importance of Tsengwen River.

Since the late Pleistocene, the Chianan Plain can be divided into the western subsiding foreland basin, which is bounded by the Hsinyin blind fault, and the eastern uplifted fold-thrust belt (Chen et al, 2004b; Yang, 2007). Due to the structural differences between the eastern and western sides, the hanging wall area (eastern side) of the Xinying Fault exhibits aggradation and progradation, while the footwall area mainly experiences aggradation due to subsidence. As a result, the coastline has shown minimal changes near the Tainan Science Park area adjacent to the fault from 3300 years ago to the 17th and 18th centuries (Chen et al., 2009).

The deceleration of sea-level rise and the uplift of the eastern region caused by the Hsinyin blind fault has resulted in the shallowing of the sedimentary basin. Furthermore, with the accumulation of sediment towards the sea since approximately 6000 years ago, the coastline rapidly moved westward (Chen et al., 2004a). In the 17th century, the changing course of the Tsengwen River led to continuous oscillation in its lower reaches, resulting in the continuous expansion of land area and westward expansion of the coastline (Shih, 1979; Chang et al, 1996). This process is also evident in the gradual westward reduction of lagoonal sandbars in the southwestern part of Taiwan Island between 1904 and 1999 (Wang, 2009).

doi:10.6342/NTU202302306

3 Materials and Methods

3.1 Sediment cores

The five sediment cores AO690, AO691, AO692, AO699 and AO700 used for this study was collected during the November 7th 2021 to January 18th 2022 from AO region of Tainan Science Park drilling project. This region is located on the alluvial plain of the southern bank of the Zengwen River, eastern Chianan Plain. The recovery length for Core 690 was 50 m, Core 691 was 50.5 m, Core 692 was 52 m, Core 699 was 101.7 m, and 101.3 m for Core 700.

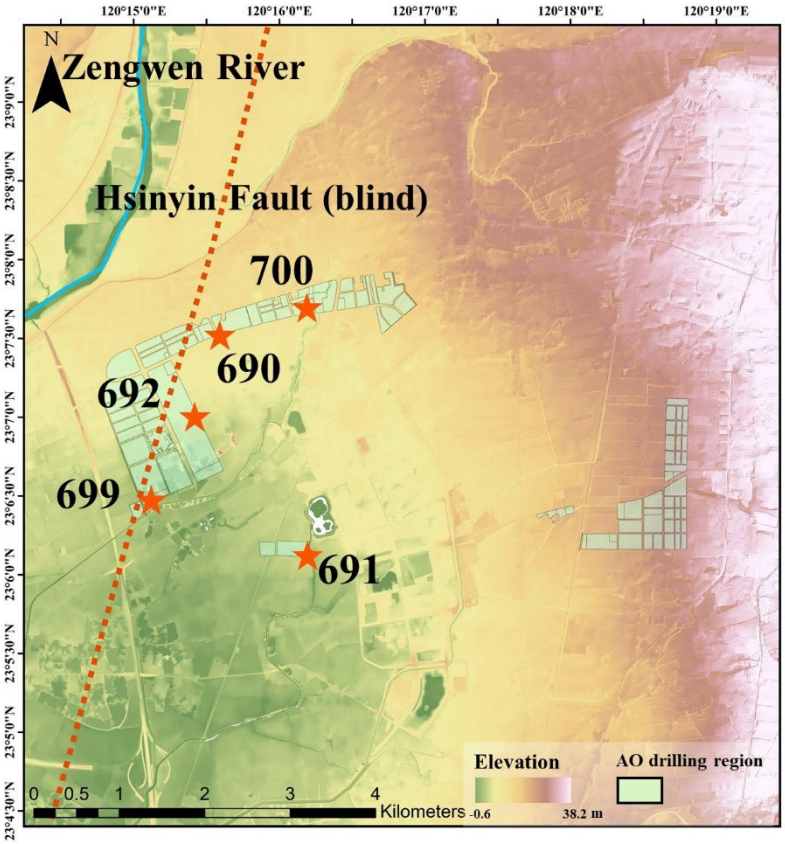

Figure 3.1 Locations of the sediment core using in this study. A 5 m resolution DEM provided by SSC is utilized to represent the elevation changes around the Tainan Science

doi:10.6342/NTU202302306

Park. The green polygons represent the drilling area in the AO region, and the cores for analysis are marked as red stars. Hsinyin Fault across the drilling region is adopted from Chen et al. (2004), represented by the red dashed line, and the bold light blue line depicts the Zengwen River.

3.2 Radiocarbon dating

The radiocarbon dating was measured by Accelerator Mass Spectromrtry (AMS) through the Beta Analytic® AMS Lab dating services and follow their procedure. The process of AMS measurement utilizes a cobalt catalyst to facilitate the hydrogen reduction of the CO_2 sample, ultimately yielding graphite. The CO_2 required for the analysis is acquired through the combustion of the sample at temperatures exceeding 800°C in an oxygen-rich environment. Subsequently, the generated CO_2 is first dried with methanol/dry ice, followed by its collection in liquid nitrogen for subsequent graphitization. To ensure the reliability and consistency of the analytical process, identical reactions are carried out on reference standards, internal quality assurance (QA) samples, and background samples, thus ensuring systematic chemistry.

The obtained analytical results are based on the measurement of the $^{14}C/^{13}C$ ratio in the sample relative to the $^{14}C/^{13}C$ ratio in Oxalic Acid II (NIST-4990C), using one of Beta Analytic's particle accelerators equipped with SNICS ion source.

Furthermore, the AMS results are adjusted for total isotopic fractionation by

doi:10.6342/NTU202302306

referencing the machine graphite $\delta^{13}C$. The $\delta^{13}C$ value reported for the sample is determined using different methods depending on the nature of the sample material. Solid organics are sub-sampled and converted to CO_2 using an elemental analyzer (EA), while water and carbonates undergo acidification in a gas bench to produce CO_2. Both the EA and the gas bench are directly connected to an isotope-ratio mass spectrometer (IRMS), which performs the separation and measurement of the CO_2 masses (44, 45, and 46) and calculates the sample's $\delta^{13}C$ value.

3.3 Multi-proxy method

The high-resolution and non-destructive XRF analysis is utilized to obtain 1 mm resolution elemental intensities. Therefore, in addition to the core description aiding in sampling, we can also refer to the elemental data to target specific intervals. For avoiding the replicate measurement of the samples with the same characteristics and increasing the efficiency of the experiments, 2 samples in 1 m were taken, and a total of 404 samples were conducted for the TOC, TN, and grain size analysis. Lastly, the appropriate proxy will be selected through these analyses for further discussions.

3.3.1 XRF analysis

The XRF scanning, X-ray radiographic images, optical images, and magnetic susceptibility were measured by Itrax XRF core scanner (Itrax) at the Itrax-XRF Core

doi:10.6342/NTU202302306

Scanner Lab. Sediment cores were analyzed using the 3 kW Mo target. The XRF measurements were analyzed at 30 kV, 50 mA, 1 mm resolution with 2 s exposure time. For sample pretreatment, spatulas were used to scrape out a new surface of samples and made the surface smooth and even that can let Itrax detect the freshest signal.

After sample was pretreated, sediment core was moved and executed surface scan for estimating the scanning route of XRF detector, optical images were also taken through this process. However, the topography of the core surface fluctuated due to the cracks and collapse within the core, deviation was recorded through the surface scan, this deviation can cause a crash between core and the XRF detector. For lowering the risk of destructing the XRF detector, thin tape was used to establish the smooth surface. Besides, water content of sediment core was lost during the scanning, for maintaining moisture, ultra-thin plastic wrap was used to film over the sample. After checking the status of sample, scanning will be ready after setting the radiographic and XRF parameters (Löwemark et al., 2019).

During the operation, the X-ray irradiated by Mo tube excites the inner shell electron of atom and ejects the electron to the outer shell. The unstable open position of the inner shell will fill by an electron from the outer shell and characteristic fluorescence is emitted (Jenkins & De Vries, 1970). This characteristic fluorescence is accepted by the XRF detector and can correspond to a specific element from aluminum to uranium (Guyard et

doi:10.6342/NTU202302306

al., 2007). To ensure data quality, duplicate measurements will be conducted every 10 meters to assess the reproducibility of the intensity of elements. Elements with a reproducibility greater than 0.6 will be designated as the main components for further data processing, which are Si, K, Ca, Ti, Mn, Fe, Zn, Rb, Sr, Zr.

3.3.2 Elemental carbon and nitrogen analysis

The percentage of TOC and TN were measured by Elemental Analyzer (EA). For sample preparation, the water contained in the samples was removed by the vacuum freeze dryer and ground into fine-grained powder to avoid inhomogeneity. Fine-grained samples (ca. 50 mg) were filled into ceramic cups and analyzed by an Elementar soli TOC® cube EA. All samples were divided into sets of five, one standard sample was added for ensuring the stability of the instrument, and two empty ceramic cups were placed respectively at the beginning and the end of the sample set for calculating the system blank of the instrument.

During the operation, samples were combusted with oxygen to form carbon dioxide and nitric oxide gases, and gases were detected respectively by an infrared detector and an electrochemical detector. For separating organic and inorganic carbon, three-step temperature programming during combustion was needed: First, starting around 100 – 550 °C (holding time 400 s), second, 550 – 600 °C (holding time 120 s); these two steps were for TOC measurements. Lastly, combustion was executed around 600 – 900 °C

doi:10.6342/NTU202302306

(holding time 150 s) for total inorganic carbon (TIC) measurement. Data was collected by Elementar soli TOC program and fitted with the calibration curves constructed from the Leco soil standard (r^2>0.9999 for TC; r^2>0.9995 for TN).

3.3.3 Grain size analysis

The grain size was measured by Malvern Mastersizer 2000 laser diffraction particle size analyzer (SPSA). For sample preparation, the sample (ca. 1 g) was weighed into a 50 ml centrifuge tube and mixed with 10 ml 30 % hydrogen peroxide (H_2O_2) and 10 ml DI water for removing the organic matter that might affect the measurement. After the reaction had been done, Centrifuge (3500RPM, 10 min) was used to remove the waste from the upper layer, 10 ml DI water was added to oscillate with Ultrasonicator to clean up the residue of H_2O_2, and Centrifuge was executed again to remove the waste. The sample was sieved in 600 μm mesh for removing the matters that are not the component of sediment and lowering the risk of exceeding the detection limit. For removing the calcium carbonate, 10 ml 30 % hydrochloric acid (HCl) and 10 ml DI water were added. After the reaction of hydrochloric acid had been done, centrifuging was executed to remove the waste from the upper layer, and 10 ml DI water was added to oscillate with Ultrasinicator to remove the residue of HCl, and Centrifuge was executed again to remove the waste. This step needs to be repeated three times for ensuring cleaned up completely. For dispersing the particle, 5 ml 0.05 M dispersant ($(NaPO_3)_6$) and 5 ml Milli-Q were

doi:10.6342/NTU202302306

added to oscillate with Ultrasonicator for 15 minutes. After the particle was dispersed, the experiment can be started.

The scattering phenomenon was observed during the experiment when a He-Ne laser was combined with a blue laser and directed towards the particle sample. Subsequently, the scattered light passes through a set of inverse Fourier lenses and images on the focal plane equipped with multiple detectors. The energy distribution of the scattered light directly correlates with the diameter of the particles, allowing for the determination of the particle size distribution.

3.3.4 Lithofacies analysis

Sediments have different grain size, the grain size between 1/16 mm to 2 mm called sand, between 1/16 mm to 1/256 mm called silt, finer than 1/256 mm called clay (Wentworth, 1922). According to different combination of lithology, lithology can be divided into three crucial lithofacies: sand lithofacies (the percentage of sand > 90%), interbeds of sand and mud lithofacies (the proportion of sand and mud ranges between 30~70%), and mud lithofacies (including silt and clay). In addition, sedimentology structure, calcium fossil, calcareous concretion, and bioturbation can further subdivide the lithofacies into 16 sub-lithofacies (Table 3.1).

Table 3.1 Lithofacies code

doi:10.6342/NTU202302306

Lithofacies Code		Sedimentary Characteristics	Formation Mechanism
Sand lithofacies	Su	Upward-fining sequence, occasional mud clasts, gravel, nodules	Flow drag
	Sm	Well-sorted, no stratification	High-energy flow
	Sx	Well-sorted, cross-stratified, thin mud layers	High-energy flow and suspension sedimentation interaction
	Sh	Well-sorted, parallel stratification, thin mud layers	High-energy flow and suspension sedimentation interaction
	Sr	Well-sorted, ripple stratification, thin mud layers	Low-energy flow and suspension sedimentation interaction
	Sf	Rich in fossils	High-energy flow, wave action
	Sc	Rich in carbonaceous debris	Swamp, levee, or floodplain sedimentation
	Ss	Sedimentary structures deformed during deposition	Gravity sliding, rapid deposition, loading, dehydration
Sand-mud interbed lithofacies	SMr	Mud interlaced, wavy, or lenticular stratification	Periodic tidal action, alternating dynamic and static flows
	Sme	Erosion surface overlain by parallel or low-angle cross stratification, occasional shell fragments	Suspension sedimentation and intermittent high-energy events interaction (storm action)

doi:10.6342/NTU202302306

Mud lithofacies	Mm	Well-sorted, no sedimentary structures	Suspension sedimentation, intense bioturbation or none
	Mb	Irregular residual stratification	Suspension sedimentation, moderate bioturbation
	Mr	Ripple stratification	Suspension sedimentation, occasional low-energy flow action, mild bioturbation
	Mf	Contains autochthonous fossils	Suspension sedimentation, in-situ biological growth
	Mc	Rich in mud carbon, plant debris, organic matter	Swamp, levee, or floodplain sedimentation
	Mmt	Mottled structure, plant roots, calcareous concretions (CC)	Exposed water surface, soil formation influence

3.3.4.1 Fining-upward sand (Su)

The thickness of this lithofacies ranges from several tens of centimeters to several meters, exhibiting a lithology comprising of very fine sand to coarse sand. It is a sandstone unit displaying a distinct upward fining trend and an erosive base, and the base is often characterized by abundant small pebbles or irregular mud clasts. This lithofacies is interpreted as having been deposited by the drag effect and is commonly found in a terrestrial fluvial braid plain or deltaic depositional system (Miall, 1977, 1978; Thomas

doi:10.6342/NTU202302306

et al., 1987).

3.3.4.2 Massive sand (Sm)

The thickness of this lithofacies ranges from several tens of centimeters to several meters, exhibiting a lithology comprising of very fine sand to coarse sand. The sand layer lacks sedimentary structures and is minimally disturbed by bioturbation, suggesting it was formed by high-energy water flow (Reineck & Singh, 1980; Dott & Bourgeois, 1982). A typical characteristic of this facies can be found in narrow channels formed due to the collapse of banks (Miall, 1996).

3.3.4.3 Cross-bedded sand (Sx)

The thickness of this lithofacies ranges from several tens of centimeters to several meters, exhibiting a lithology comprising of very fine sand to medium sand. This sand layer involves planar cross-stratification, trough cross-stratification, or low-angle cross-stratification, with minimal bioturbation and often occurs together with horizontally bedded sand lithofacies (Sh). It was deposited by high-energy water flow, and is typically associated with environments such as foreshores or offshore areas dominated by wave and storm action (Clifton et al., 1971; Reineck & Singh, 1980; Dott & Bourgeois, 1982; Harms et al., 1982).

doi:10.6342/NTU202302306

3.3.4.4 Horizontally bedded sand (Sh)

The thickness of this lithofacies ranges from several tens of centimeters to several meters, exhibiting a lithology comprising of very fine sand to medium sand. The sand layer bears some residual mud or silt lamination, with barely any bioturbation. It was deposited by the interaction with high-energy water flow and low-energy suspended deposition (Reineck & Singh, 1980), and typically exists in environments such as foreshores or offshore areas dominated by wave and storm action (Clifton et al., 1971; Reineck & Singh, 1980; Dott & Bourgeois, 1982; Harms et al., 1982).

3.3.4.5 Ripple cross-laminated sand (Sr)

The thickness of this lithofacies is around several tens of centimeters, exhibiting a lithology comprising of very fine sand to medium sand. The ripple movement generate different internal formation in the sand layer. The slow sedimentation rate of migrating ripple from suspension results in ripples that erode each other (Miall, 1996), and typically exist in environments such as foreshores or offshore areas dominated by wave and storm action (Clifton et al., 1971; Reineck & Singh, 1980; Dott & Bourgeois, 1982; Harms et al., 1982).

3.3.4.6 Fossil-bearing sand (Sf)

The thickness of this lithofacies is around several tens of centimeters, exhibiting a

doi:10.6342/NTU202302306

lithology comprising of very fine sand to medium sand. The sand layer bears the calcium fossils that indicate the salty environment and is often accompanied by other sand lithofacies. High-energy water flow forms this lithofacies, and it is also affected by the wave action (Reineck & Singh, 1980; Dott & Bourgeois, 1982).

3.3.4.7 Carbon-bearing sand (Sc)

The thickness of this lithofacies is around several tens of centimeters, exhibiting a lithology comprising of very fine sand. The sand layer bears the carbon debris, which often exist in backswamps or floodplain.

3.3.4.8 Sigmoidal cross-laminated sand (Ss)

The thickness of this lithofacies is around several tens of centimeters, exhibiting a lithology comprising of silt to fine sand. This lithofacies has a load structure and slumping structure in sandstone, barely any bioturbation, often accompanied by horizontally bedded sand (Sh) and ripple cross-laminated sand (Sr). It typically exists in the rapid deposition of delta foreland.

3.3.4.9 Rhythmic sand-mud interbed (SMr)

The thickness of this lithofacies is around several centimeters. This lithofacies has sand with flaser, wavy, or lenticular bedding, interbedded with thin mud or silt. It existed in an environment dominated by the tidal effect, typically formed under a different water

doi:10.6342/NTU202302306

flow strength (Reineck & Wunderlich, 1968; Klein, 1971; Reineck & Singh, 1980; Dalrymple et al., 1992; Longhitano et al., 2012)

3.3.4.10 Erosional sand-mud interbed (Sme)

The thickness of this lithofacies is around several centimeters, and it is the interbed of sand and mud ot silt and mud in erosive contact at the bottom. This lithofacies forms when suspended sediments under normal action alternate with intermittent rapid deposition with storm events, and often appear in the estuary (Dott & Bourgeois, 1982; Swift et al., 2009) or the offshore environment above the storm-weather wave base (Dott & Bourgeois, 1982; Swift et al., 1983).

3.3.4.11 Massive mud (Mm)

The thickness of this lithofacies is around several tens of centimeters, exhibiting a lithology comprising of silt or mud. It was produced by suspended deposition in a quiet environment (Chun & Chough, 1995) or formed by the severe bioturbation that destructed the original sedimentary structures (Walker & Plint, 1992).

3.3.4.12 Bioturbated mud (Mb)

The thickness of this lithofacies ranges from several tens of centimeters to several meters, it has the characteristic of bioturbation in the mudstone or siltstone and existed in a quiet environment (Reineck & Singh, 1980).

doi:10.6342/NTU202302306

3.3.4.13 Ripple cross-laminated mud (Mr)

The thickness of this lithofacies is around several tens of centimeters. The mudstone has climbing ripples and wave ripples, which involve mild to moderate bioturbation. The lithofacies mostly in quiet environments with suspended deposition, and wavy ripples existed due to the occasional water flow (Reineck & Singh, 1980).

3.3.4.14 Fossil-bearing mud (Mf)

The thickness of this lithofacies is around several tens of centimeters. This lithofacies bears the calcium fossils in siltstone or mudstone and were mostly in quiet environments with suspended deposition.

3.3.4.15 Carbon-bearing mud (Mc)

The thickness of this lithofacies is around several tens of centimeters. It can be interpreted as a plant going through the process of deposition in a marsh environment that forms an organic-rich mudstone(Frey & Basan, 1985).

3.3.4.16 Mottled massive mud (Mmt)

The thickness of this lithofacies ranges from several tens of centimeters to several meters. It has a mottling structure and bears calcareous concretion in the siltstone or mudstone. This lithofacies is frequently existed in floodplain and marsh environments,

doi:10.6342/NTU202302306

which can be explained by the weathering of sediments (Bown & Kraus, 1987; Kraus, 1987; Kraus & Aslan, 1993).

doi:10.6342/NTU202302306

4 Results

4.1 Radiocarbon dating

A total of 24 samples, comprising shells, wood, calcareous concretions and peat obtained from each core, were collected to conduct radiocarbon dating. Cores 690, 691, and 692 provide chronological information for the upper 48 meters, whereas cores 699 and 700 provide it for the depth interval of 48 to 100 meters.

Table 4.1 Radiocarbon dating result

Core	Depth (m)	sample	Conventional radiocarbon age
690	13.8	Shells	3620 ± 30 BP
	34.5	Shells	7470 ± 30 BP
	41.4	Shells	8010 ± 30 BP
	46.2	Shells	8470 ± 30 BP
691	5.4	Calcareous concretions	5360 ± 30 BP
	11.1	Shells	4200 ± 30 BP
	18.8	peat	14100 ± 40 BP
	22.9	Wood	6440 ± 30 BP
	36.7	Shells	7490 ± 30 BP
	44.6	Shells	8330 ± 30 BP
692	4.7	peat	12420 ± 40 BP
	14.6	peat	14700 ± 50 BP
	19.8	Wood	5730 ± 30 BP
	29.8	Wood	6480 ± 30 BP
	44.1	Shells	8240 ± 30 BP
699	48.9	Shells	8480 ± 30 BP
	71.7	Shells	9870 ± 40 BP

doi:10.6342/NTU202302306

	77.4	Wood	9520 ± 40 BP
	84.5	Shells	10260 ± 40 BP
700	48.6	Wood	8220 ± 30 BP
	56.3	Wood	8820 ± 30 BP
	60.6	Shells	9320 ± 30 BP
	63.5	Shells	9530 ± 30 BP
	79.9	Wood	10000 ± 30 BP

4.2 Multi-proxy sediment analysis

Different proxies have been selected for comparison with the stratigraphic column. Through the proxy demonstrated by previous studies, and the trends of the elements observed by the PCA on XRF data, The logarithm ratios of Ca/Ti and Zr/Rb have been chosen to indicate the relative influences of marine and terrestrial environments and variations in grain size. Additionally, organic matter in sediments can provide valuable information for reconstructing paleoenvironments and climate. We have selected TOC and TOC/TN as our proxy, which can indicate the amount of the organic matter and its sources. For example, vascularized plants have compounds rich in carbon, such as cellulose, while algae are mainly composed of proteins that are rich in nitrogen (Meyers, 1997). Grain size distributions are also indispensable to enhance the interpretation of different environments, percentage was used to observe the variation of clay, silt, very fine sand (Vfs) to fine sand (Fs), and the particle larger than medium sand (Ms). Moreover, it can be further compared with the Zr/Rb logarithm ratio.

doi:10.6342/NTU202302306

4.2.1 Core 690

In core 690, the lowest Log(Ca/Ti) value can reach approximately -1.25, while the highest can reach around 2.5. From the core top to a depth of 13.0 m, the values continuously rise from -1.25 to around 1, and suddenly increase to 2 between 13.0 and 14.1 m, suggesting a relatively marine environment. After 14.1 m, the values abruptly drop to around 0 and steadily increase to approximately 1.5 near 19.4 m. From 19.4 to 22.5 m, values fluctuate between 1 and 2, and finally rise to 2.5, representing the most marine-influenced interval in the core. Subsequently, the values rapidly decrease to below 1 and continue to rise to around 1.5 at 24.4 m. Following 25.2 m, the values decrease to around 1 and remain stable until 28.3 m, with a short drop to 0 around 26.1 m, indicating a rapid transition between marine and terrestrial environments. Between 28.3 and 32.5 m, the values decline to a range of 0.5 to 1, and in the 32.5-41.0 m interval, a stable signal appears, with values mostly around 0.3, occasionally reaching 0.5, suggesting a transitional zone influenced by both marine and terrestrial factors, resulting in stable values. Finally, more significant fluctuations are observed from 41.0 to 50.0 m, with values exceeding 1 between 43.0 and 43.4 m and dropping as low as -0.5 between 45.0 and 46.8 m.

In the Log(Zr/Rb) signal, the lowest value is approximately -0.5, while the highest can reach 1.25. From the core top to 4.0 m, the values mostly remain below 0.25. Besides,

doi:10.6342/NTU202302306

the range of Log(Zr/Rb) from 0 to -2.5 can be observed in 0.5-1 m and 2.4-3.8 m. At 3.0 m, the values even drop below -0.25, indicating relatively finer particle sizes. From 4 to 14.1 m, the values range between 0.25 and 0.75, with occasional values below 0.25 observed at 5.8-6.2 m, 7.0-7.4 m, and 13.8-13.9 m. Between 14.1 and 18.3 m, there is a gradual increase in values, rising from the lowest value of -0.5 in the entire core to 0.75. The Log(Zr/Rb) values range between 0.25 and 0.75 until 22.5 m, then sharply decrease to -0.25. Between 22.5 and 27.9 m, two sequences show an increase from -0.25 to nearly 1. Notably, from 27.9 to 50.0 m, rhythmic variations occur, with values ranging from the lowest value of -0.5 to the highest value of 1.25, and then dropping back to -0.5.

The particle size composition can be obtained through laser grain size analysis, where the clay fraction can reach approximately 25% at the finest part, and particles larger than medium sand can account for up to 50% at the coarsest interval. Observing the particle size distribution along the entire core, two intervals with higher clay proportions can be identified: around 14.2-14.3 m, the clay content can reach close to 25%, and around 38.3-38.4 m, it can approach 20%. Additionally, several intervals with higher proportions of particles larger than medium sand can be identified: in the 9.6-13.9 m, the sand content is greater than 25%, with the 13.8-13.9 m segment exceeding 40%. Between 18.7 and 28.2 m, intermittent intervals show higher proportions of medium sand, with the 20.7-20.8 m and 22.5-22.6 m segments reaching a percentage of 50%. Finally, in the 41.3-41.4

doi:10.6342/NTU202302306

m and 43.2-43.3 m intervals, the proportion can reach approximately 20%. It is worth noting that in the 20.3-26.2 m interval, where there are more particles larger than medium sand, there is also an approximate 10% presence of clay, suggesting the occurrence of some clay clasts within this sand interval.

In terms of the elemental carbon analysis, lower TOC can be found in most data points, larger than 1 % only at 31.8-31.9 m. For TOC/TN ratio, most data points are below 8, with values exceeding 12 only at 1.1-1.2 m and 31.8-31.9 m.

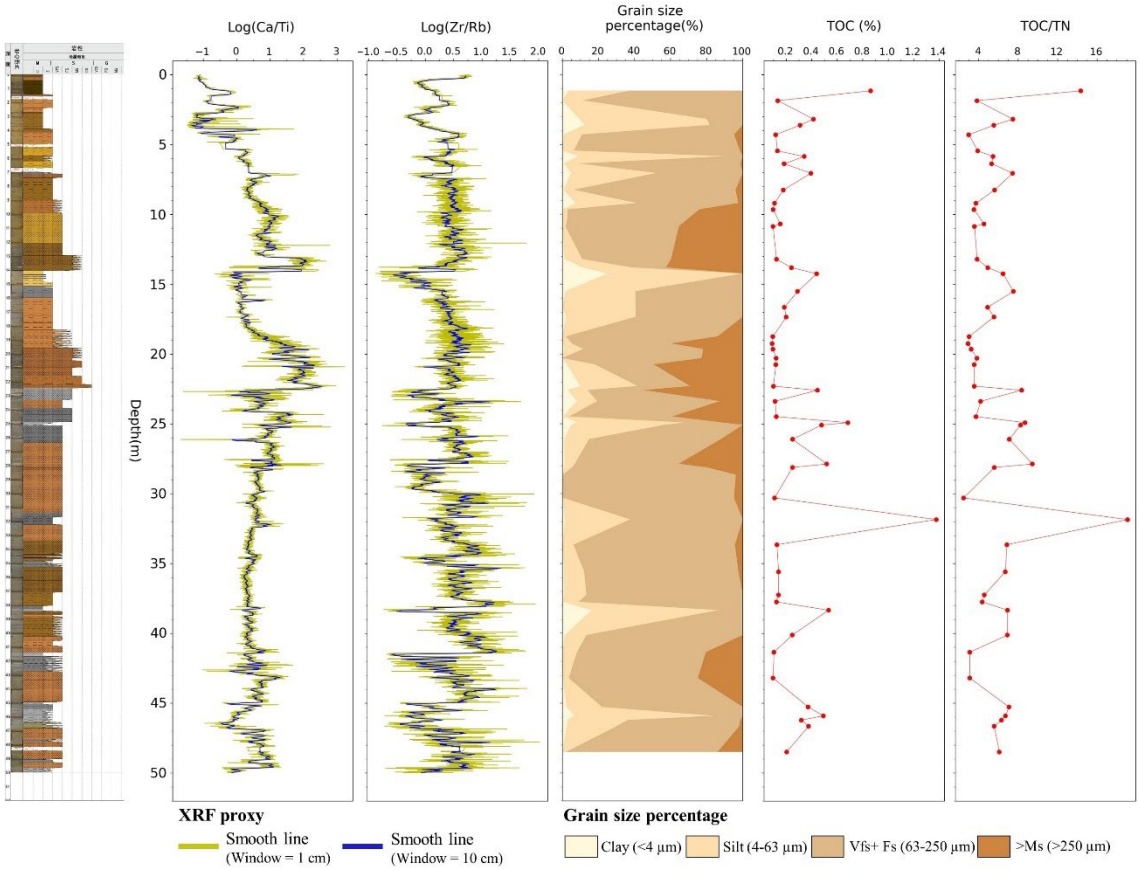

Figure 4.1 Multi-proxy profile of core 690, including XRF proxy Ca/Ti and Zr/Rb in logarithm form, grain size percentage, TOC and TOC/TN. The smooth window with 1 cm and 10 cm are represented by yellow line and blue line. The color gradient from light

doi:10.6342/NTU202302306

to dark orange is used to represent the gradation from fine to coarse grain sizes. The sediment is classified into the following categories: clay, silt, the combination of Vfs and Fs, and grain sizes larger than Ms.

4.2.2 Core 691

In core 691, the Log(Ca/Ti) can reach a maximum of approximately 2 and a minimum of -2. From the core top to 5.1 m, the values are relatively low, approaching -1.5. There is an increase to around 0 at 4.3-4.6 m, but it remains a relatively low value. From 5.1 to 18.8 m, the values fluctuate around 0, with a drop to around -2 at 12.7-14.9 m. Values below -1 are also observed at 6-6.2 m, 9.2-9.3 m, and 11.8-12.0 m, suggesting a predominantly terrestrial environment for this interval. Between 18.8 and 21.8 m, there is a sudden increase to nearly 2, suggesting a rapid environmental change. After reaching the higher values, the Log(Ca/Ti) starts to decrease, reaching approximately -1.5 at 22.4-23 m. It then gradually increases to 1 and stabilizes around 0.75 at 26.8 m. This is followed by a relatively stable signal that persists until 36.8 m, maintaining a value of around 0.5. This suggests a balanced influence between marine and terrestrial. Between 36.8 and 43.1 m, there is a more pronounced fluctuation, with an overall increasing trend and reaching a maximum value of 1.5. Finally, from 43.1 to 50.6 m, the values return to lower levels, with an increase to nearly 1 only at 44.9-46.6 m, while the majority of values remain below 0, with a drop to -2 at 49.4-49.6 m.

doi:10.6342/NTU202302306

Regarding the Log(Zr/Rb) signal, the lowest value is -0.75, and the highest value is 1.5. From the core top to 18.8 m, Log(Zr/Rb) rarely exceeds 0.5 and is predominantly below 0. At 18.8 m, the value suddenly increases from -0.25 to around 0.75 and remains stable until 22.1 m. Subsequently, the value drops sharply to -0.5 and rises rapidly to the highest value of 1.5 at 22.4-23.9 m. From 23.9 to 33.7 m, the values fluctuate mostly between 0.25 and 0.5, indicating a relatively stable particle size interval. In the following interval of 33.7-42.8 m, larger oscillations are observed, with values ranging from -0.25 to 1.25, without a clear rhythm. Finally, until 50.6 m, the amplitude of fluctuations decreases, with values generally ranging from -0.25 to 0.5, suggesting smaller variations in particle size compared to the previous interval.

The analysis of particle size distribution revealed that the clay fraction reached approximately 25% at its finest part, while particles classified as medium sand and coarser accounted for 30% at its coarser part. Examination of the particle size distribution across the entire core identified two intervals with relatively high clay proportions. These intervals were found at 4.6-4.7 m and 22.4-22.5 m, with clay percentages approaching 25%. Additionally, significant proportions of medium sand and coarser particles were observed in several intervals. These intervals, located at 13.8-14.8 m, 18.7-21.3 m, 31.4-31.5 m, and 46.4-46.5 m, exhibited proportions close to 20%. Furthermore, two intervals within the range of 41.3-42.8 m exhibited proportions exceeding 20%, with the highest

doi:10.6342/NTU202302306

proportion of approximately 30% observed at 25.6-26.6 m. A relatively stable particle size composition was observed in the interval of 23.6-36.7 m, suggesting a relatively quiescent environment. In this interval, approximately 80% of the particles consisted of very fine sand and fine sand.

In terms of the elemental carbon analysis, lower TOC can be found in most data points, larger than 1 % only at 8.5-8.6 m and 47.6-47.7 m. For TOC/TN ratio, the majority of data points were below 8. Only at 8.5-8.6 m, 45.7-45.8 m, and 47.6-47.7 m were values observed that approached or exceeded 12.

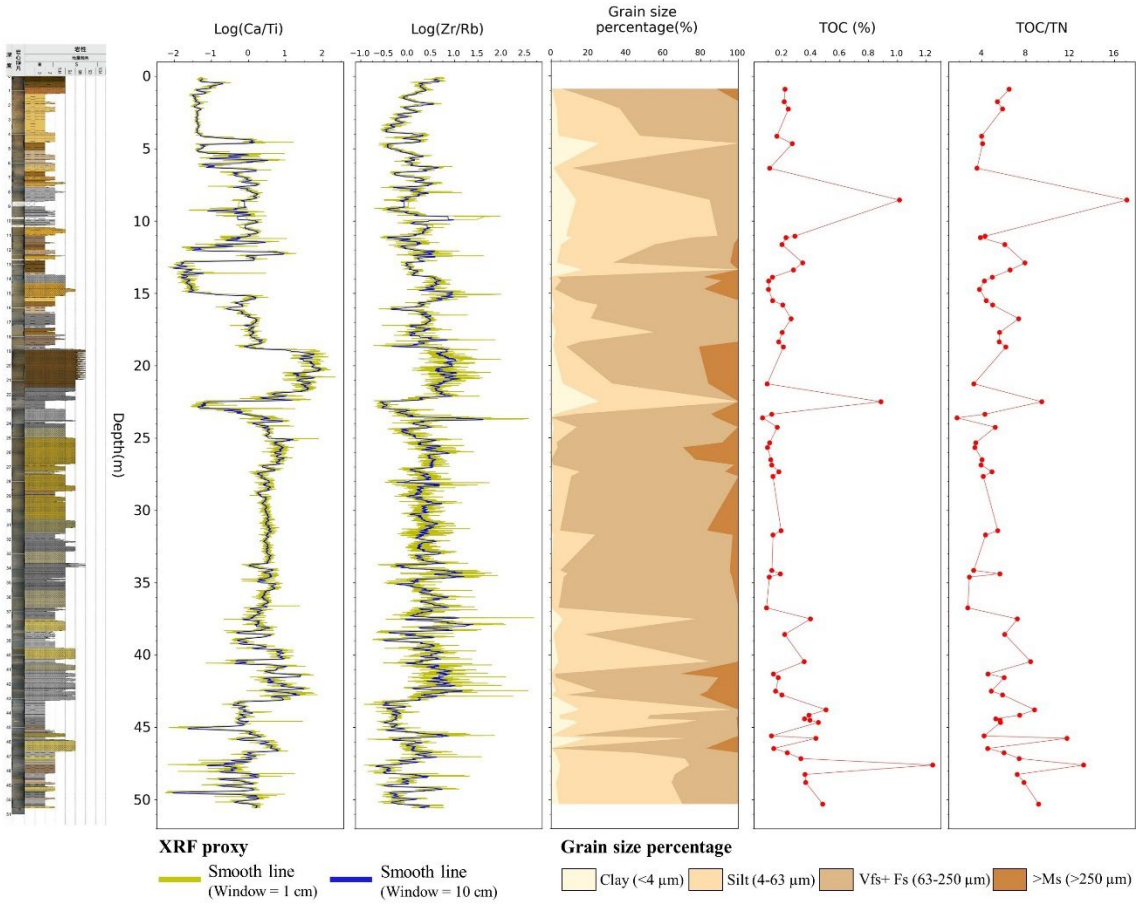

Figure 4.2 Multi-proxy profile of core 691, including XRF proxy Ca/Ti and Zr/Rb in logarithm form, grain size percentage, TOC and TOC/TN. The smooth window with 1

doi:10.6342/NTU202302306

cm and 10 cm are represented by yellow line and blue line. The color gradient from light to dark orange is used to represent the gradation from fine to coarse grain sizes. The sediment is classified into the following categories: clay, silt, the combination of Vfs and Fs, and grain sizes larger than Ms.

4.2.3 Core 692

In core 692, the Log(Ca/Ti) ranges from approximately -1.75 to a maximum of around 1.5. From the core top to a depth of 4.3 m, the ratio increases from -1.5 to 1.25, with a more rapid increase observed at 2.7 m. Between 4.3 m and 8.0 m, the values drop back to around -0.5 and gradually rise to 1. In the interval of 8.0 m to 19.0 m, the values generally remain below 0, with multiple intervals showing values around -1.5, indicating a predominantly terrestrial environment. From 19.0 m to 29.0 m, there is an upward trend, with the ratio ranging from -1.75 to nearly 1.5.

Notably, a stable signal observed earlier in other cores also appears between 30.7 m and 42.8 m in core 692, with values ranging from approximately 0.25 to 0.5. After the stable interval, the Log(Ca/Ti) ratio continues to rise to its maximum value in the entire core, reaching around 1.5 between 44.0 m and 44.1 m. It then quickly drops back to around 0.5, exhibiting fluctuations between -0.5 and 1 in the interval of 44.1 m to 52.0 m. This suggests an environment influenced by both marine and terrestrial factors, with alternating dominance of sediment composition in this interval.

doi:10.6342/NTU202302306

Regarding the Log(Zr/Rb) signal, the lowest value is around -0.75, while the highest value can exceed 1.5. From the core top to 4.5 m, the Log(Zr/Rb) ratio gradually rises from -0.25, reaching its peak value of 1 around 2.4-2.7 m and 3.8-3.9 m, indicating the presence of coarser particles. In the interval of 4.7 m to 15.2 m, the signal fluctuates between 0 and 0.5, with a peak around 11 m. From 15.2 m to 25.3 m, the values slightly decrease, ranging from -0.5 to 0.25, suggesting finer particle sizes compared to the previous interval.

Between 25.3 m and 27.5 m, the values gradually increase from 0.25 to 1, with a peak exceeding 1.5, indicating a complex variation in particle size rather than a simple coarsening. After this interval, the values gradually decline and reach a low point of -0.25 between 29.0 m and 29.5 m, followed by a gradual increase. From around 31.5 m to 31.9 m, the values can exceed 1. Larger values persist until around 42.6 m, with most of the signal above 0.5, and a process of increasing values from 0 to over 1.5 can be observed between 40.8 m and 42.2 m. Finally, from 42.6 m to the bottom of the core, the signal noticeably decreases overall, mostly ranging below 0.5 and occasionally reaching as low as -0.5, with values exceeding 0.75 only observed between 51.1 m and 51.6 m.

The analysis of particle size distribution revealed that the clay fraction is approximately 20% at its finest part, while particles classified as medium sand and coarser accounted for 55% at its coarser part. Analyzing the particle size distribution throughout

doi:10.6342/NTU202302306

the entire core, although the clay content is not particularly high, intervals with clay exceeding 5% exhibit a significant proportion of silt-sized particles, especially in the range of 13.4 m to 21.3 m, where silt-sized particles account for nearly 80% of the composition. The proportion of particles classified as medium sand or above shows less continuity in the data, with more distinct peaks observed. These peaks occur at 4.1-4.2 m (45%), 7.8-7.9 m (30%), 22.6-22.7 m (25%), and reach a maximum of 55% at 28.5- 28.6 m. Additionally, there is a gradual increase in the proportion of medium sand or coarser particles observed in the interval of 47.5 m to 51.4 m.

In terms of the elemental carbon analysis, lower TOC can be found in most data points, larger than 1 % only at 19.9-20.0 m. For TOC/TN ratio, most data points fall between 4 and 8. However, values exceeding 12 can be observed in intervals of 19.9-20.0 m and 47.5-47.6 m. Furthermore, there are intervals with values below 4, specifically at 4.0-4.2 m, 7.8-8.9 m, 28.2-28.6 m, and 41.6-43.3 m.

doi:10.6342/NTU202302306

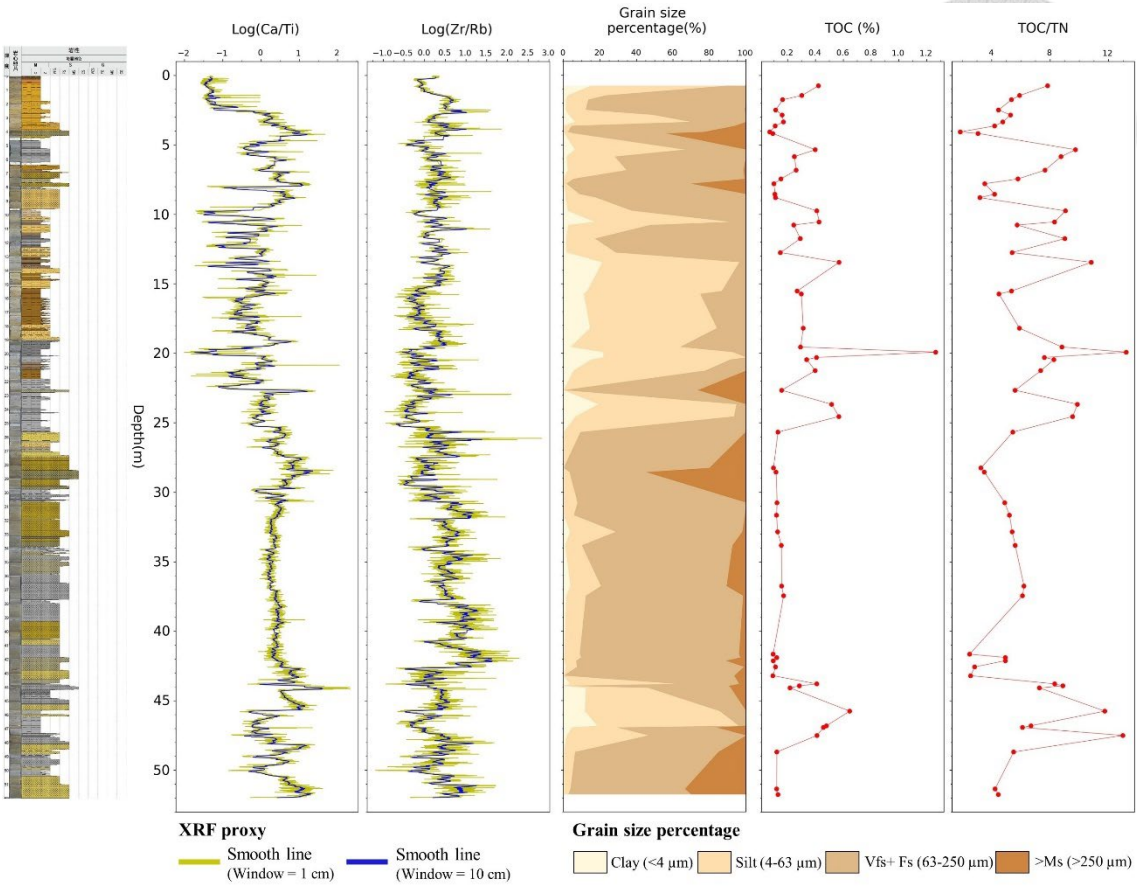

Figure 4.3 Multi-proxy profile of core 692, including XRF proxy Ca/Ti and Zr/Rb in logarithm form, grain size percentage, TOC and TOC/TN. The smooth window with 1 cm and 10 cm are represented by yellow line and blue line. The color gradient from light to dark orange is used to represent the gradation from fine to coarse grain sizes. The sediment is classified into the following categories: clay, silt, the combination of Vfs and Fs, and grain sizes larger than Ms.

4.2.4 Core 699

In core 699, the Log(Ca/Ti) can reach a maximum value of approximately 2.5 and a minimum value of -2. From the core top to a depth of 5.7 m, the ratio gradually increases

doi:10.6342/NTU202302306

from around -1.5 to 0.5. The following section exhibits larger fluctuations, within the short interval of 5.7-7.3 m, the Log(Ca/Ti) rapidly oscillates between -1.75 and nearly 2.5. This suggests the occurrence of rapid environmental changes during this period. Beyond 7.3 m, the values mostly remain below 0.25, persisting until 15.7 m. Subsequently, within the interval of 15.7-26.0 m, the Log(Ca/Ti) sharply drops to its lowest value of -2 and gradually rises to 1.5. This indicates a gradual influence of the marine environment on the sediment.

Notably, similar to other 50 m cores, a stable signal with values ranging from 0.3 to 0.5 appears between depths of 29.3 m and 44.9 m. In the interval of 44.9-65.1 m, the values predominantly fluctuate between 0 and 0.5, exhibiting a higher frequency of variation. Subsequently, the signal rapidly decreases to -1.75 within the 65.1-65.9 m range, followed by a quick return to a high value of 1.75. From there, until 77.4 m, except for occasional lower values, the entire section remains mostly within the range of 0-0.5. Within the interval of 77.4-84.6 m, the values gradually rise from 0.5 to 1.75. However, within the 84.6-96.2 m range, two similar signal variations occur, both showing significant fluctuations from values close to 2 to -2. Towards the bottom of the core, there is an overall higher signal, with Log(Ca/Ti) mostly exceeding 0.5 and reaching 2 within the depth range of 97.0-98.6 m.

In terms of the Log(Zr/Rb) signal, the minimum value approaches -1, while the

doi:10.6342/NTU202302306

maximum value can reach approximately 2. From the core top to a depth of 17.2 m, the values are relatively low, with Log(Zr/Rb) mostly below 0.25 and occasionally as low as -0.75, indicating a relatively fine-grained interval. Within the 17.2-23.5 m range, there is a significant fluctuation from around -0.25 to 1.75, indicating a period of rapid grain size variation. Two gradual increases can be observed in the 23.5-35.0 m interval, where Log(Zr/Rb) rises from around -0.5 to 0.75. Subsequently, the Log(Zr/Rb) signal does not exhibit sudden fluctuations, suggesting a slow upward or downward trend. At 41.7 m, Log(Zr/Rb) exceeds 1.5 and steadily decreases to nearly -0.75 at 65.9 m. It then gradually rises again, surpassing 1.25 at 69.3 m, followed by a declining trend within the 69.3-78.0 m interval, returning to around -0.75. In the 78.0-101.8 m range, there are distinct instances of both upward and downward trends, from 78.0 to 83.2 m, Log(Zr/Rb) rises from -0.75 to around 0.75, while from 89.1 to 94.1 m, the value drops from 1.25 to -0.75.

Observing the grain size composition, particles larger than medium sand constitute a relatively small proportion in this core. Only three intervals exceed 20%: 19.7-22.5 m (with a maximum of up to 45%), 25.6-25.7 m (35%), and 82.6-82.7 m (30%). On the other hand, clay can reach a maximum of 30% in this core. When considering silt along with clay, it is evident that from the surface to 17.7 m and from 73.9 m to 80.9 m, the particle composition is dominated by particles smaller than fine sand. Additionally, in the 86.3-96.5 m interval, rapid changes in grain size composition can be observed, suggesting

doi:10.6342/NTU202302306

the presence of sand-mud interbedding.

In terms of the elemental carbon analysis, lower TOC can be found in most data points, and only 3 data points have a value greater than 1 %, but there exists a high value of about 2 % at 16.6-16.7 m. For TOC/TN ratio, the signal can be divided into the upper half (0-47.7 m) and the lower half (47.7-101.8 m). In the upper half, the values mostly remain below 8, with only one occurrence of a value exceeding 12 at 24.6-24.7 m. In the lower half, four intervals exhibit values exceeding 12: 48.8-58.5 m, while three intervals show values above 12, including one instance surpassing 30 at 71.2-71.3 m. Overall, the lower half exhibits more significant variations in TOC/TN ratio, providing better differentiation of organic matter from different sources. Notably, the high values in TOC are not consistent with the peak in TOC/TN, which means the higher TOC/TN in this core is dominated by lower TN.

doi:10.6342/NTU202302306

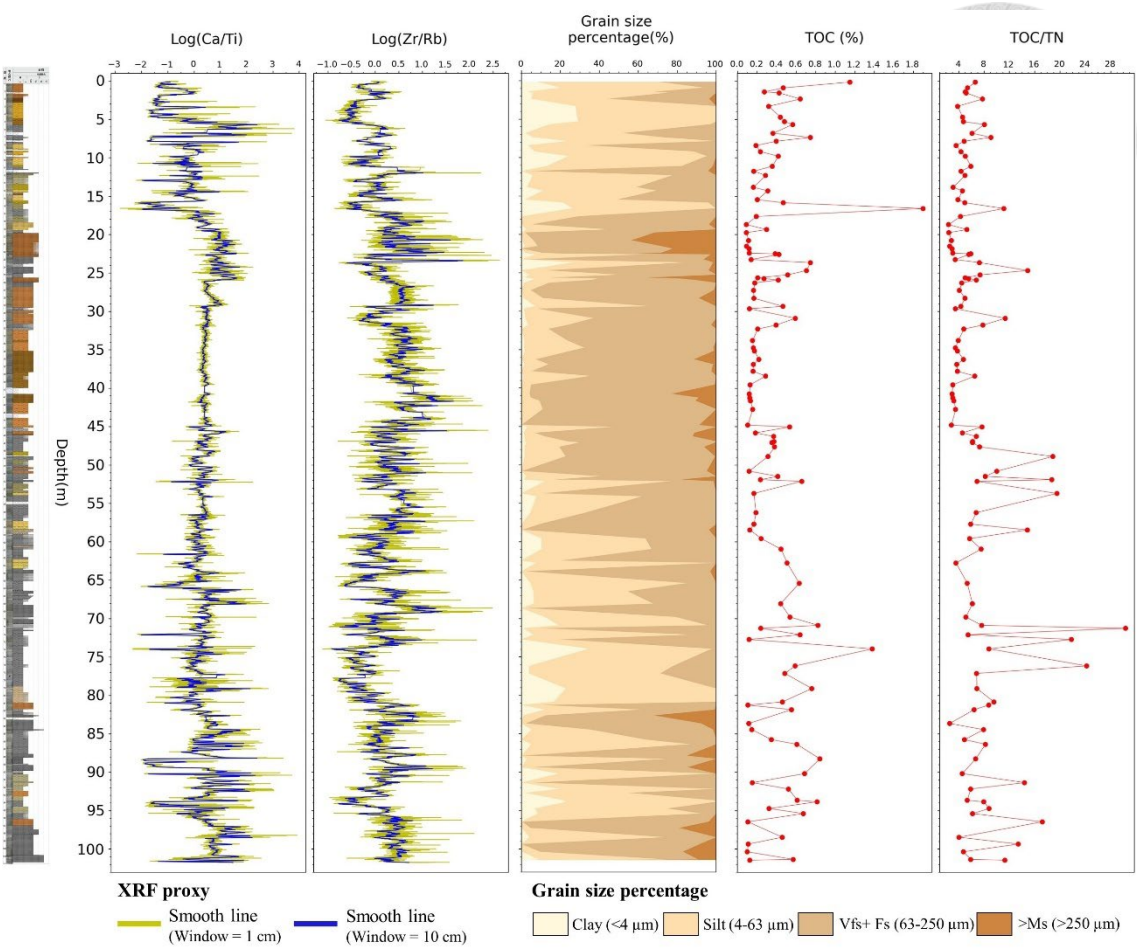

Figure 4.4 Multi-proxy profile of core 699, including XRF proxy Ca/Ti and Zr/Rb in logarithm form, grain size percentage, TOC and TOC/TN. The smooth window with 1 cm and 10 cm are represented by yellow line and blue line. The color gradient from light to dark orange is used to represent the gradation from fine to coarse grain sizes. The sediment is classified into the following categories: clay, silt, the combination of Vfs and Fs, and grain sizes larger than Ms.

4.2.5 Core 700

In core 700, the Log(Ca/Ti) can reach a maximum of approximately 3.25 and a minimum of -2. The signal exhibits significant fluctuations from the core top to 6.7 m,

doi:10.6342/NTU202302306

with a sudden increase from -1.5 to 0.75. Gradual increases in values can be observed from 6.7 m to 13.7 m, where Log(Ca/Ti) rises slowly from -1.5 to 2, suggesting a transition from terrestrial to marine conditions. Subsequently, three sequences with increasing values appear between 13.7 m and 25.0 m. The first two sequences are quite similar, starting from 1 and reaching 2, while the third sequence exhibits larger fluctuations, with an increase from 0 to 2. A relatively stable signal persists until 37.0 m, ranging between 0.3 and 0.75. This core exhibits higher Log(Ca/Ti) values compared to the interval of stable signal in other cores.

From 37.0 m to 51.5 m, the values fluctuate mostly between -0.5 and 1, with only a few intervals showing values below -1. Following that, a short period of lower values occurs from 51.5 m to 53.0 m, mostly below 0 and reaching a minimum of -1.75, indicating a transition to a more terrigenous environment. From 53.0 m to 60.1 m, the Log(Ca/Ti) gradually increases to 1.5, indicating the gradual influence of marine conditions. The signal behavior between approximately 60.1 and 75.0 m is similar to the 37.0-51.5 m interval, ranging mostly between -0.5 and 1. In the 75.0-81.7 m interval, there is a trend of two segments dropping from around 1.5 to -0.5, followed by a pattern similar to 53.0-60.07 m, indicating a gradual increase. Beyond 87.3 m, the signal exhibits a different behavior, characterized by larger fluctuations over a wider range. It quickly fluctuates between the highest and lowest values throughout the entire core, suggesting

doi:10.6342/NTU202302306

the presence of rapidly changing environmental conditions.

In the Log(Zr/Rb) signal, the minimum value can reach approximately -1, while the maximum value can reach 1.5. From the core top to a depth of 12.7 m, the value increases from -0.5 to around 0.75, indicating a gradual coarsening of grain size. In 12.7-16.2 m, the value initially decreases to 0 and then slowly rises to nearly 0.75. Subsequently, a relatively stable value range can be observed from 16.2 m to 21.4 m, with values ranging between 0.25 and 0.5. From 21.4 m to 37.3 m, there is an overall increasing trend in the Log(Zr/Rb) signal, rising approximately from -0.75 to 1.25. However, abrupt low values around -0.75 are observed at depths of 24.7-25.1 m and 33.9-34.2 m, suggesting the occurrence of specific sedimentary events that led to sudden changes in grain size.

Around 37.7-46.0 m, two similar sequences are observed, both showing an increase from approximately -0.25 to around 1. Subsequently, in 46.0-53.0 m, there is a larger and rhythmic variation in grain size, with values ranging from -0.75 to relatively high values of 1. Between 53.0 m and 58.3 m, the Log(Zr/Rb) signal exhibits a smaller range of fluctuations, mostly between 0.25 and 0.75. This is followed by a drop in values observed from 58.3 m to 65.2 m, where the value decreases from 0.75 to nearly -0.75.

The variations in the Log(Zr/Rb) signal between 65.2 m and 72.2 m are similar to those observed in the depth interval of 46.0-53.0 m. From 72.2 m to 75.3 m, the Log(Zr/Rb) value drops from 1 to -0.5, and it shows a similar trend to the preceding

doi:10.6342/NTU202302306

interval of 65.2-72.2 m. In 75.3-81.3 m, relatively smaller fluctuations are observed, ranging between 0 and 0.5. Finally, towards the bottom of the core, two segments are identified where the Log(Zr/Rb) value decreases from 0.75 to -0.75. The first segment, from 84.4 m to 91.5 m, exhibits a more linear decline, while the second segment, from 91.5 m to 100.2 m, experiences a relatively rapid decrease between 93.6 m and 95.2 m.

The results of the grain size analysis reveal that the clay fraction can reach up to 35% at its finest, while particles larger than medium sand can account for nearly 40% at their coarsest. Observing the grain size distribution at different depths of the entire core, we find that the interval from 11.6 m to 21.4 m is characterized by a higher proportion of particles larger than medium sand, with values consistently exceeding 20%. Conversely, the interval from 60.5 m to 71.5 m is dominated by particles finer than fine sand, with proportions consistently exceeding 70%. Additionally, a rapid transition in grain size is observed at 88.3-98.4 m, where there is a sudden increase in the proportion of particles larger than medium sand, previously dominated by particles finer than fine sand. This suggests a relatively rapid environmental change during that interval.

In terms of the elemental carbon analysis, lower TOC can be found in most data points, and greater than 1 % only at 80.5-80.6 m, 88.3-88.4 m, 90.3-90.4 m, and 91.4-91.5 m. For TOC/TN ratio, the signals can also be divided into two halves like core 699. The upper half (0-46.8 m) and the lower half (46.8-100.2 m). In the upper half, the values

doi:10.6342/NTU202302306

remain below 8, with no values exceeding 12. In contrast, the lower half exhibits greater variability. Values exceeding 20 are observed at 47.8-54.3 m, 61.3-61.4 m, 68.7-75.3 m, and 79.6-81.9 m. Additionally, a value exceeding 12 is also observed at 93.7-93.8 m. Similar to the pattern of core 699, the high values in TOC are not consistent with the peak in TOC/TN, the synchronized trends only appear at 80.5-80.6 m, which means the higher TOC/TN in this core is dominated by lower TN.

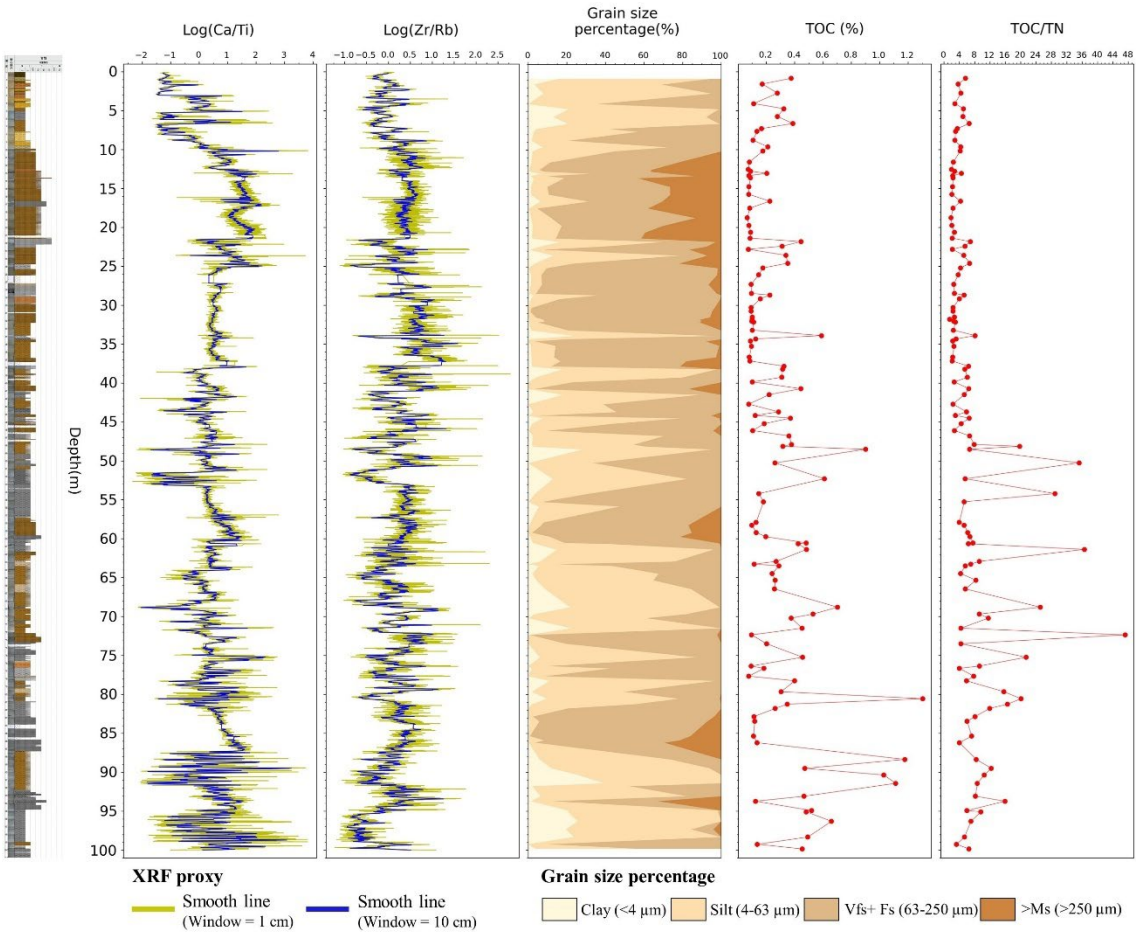

Figure 4.5 Multi-proxy profile of core 700, including XRF proxy Ca/Ti and Zr/Rb in logarithm form, grain size percentage, TOC and TOC/TN. The smooth window with 1 cm and 10 cm are represented by yellow line and blue line. The color gradient from light

doi:10.6342/NTU202302306

to dark orange is used to represent the gradation from fine to coarse grain sizes. The sediment is classified into the following categories: clay, silt, the combination of Vfs and Fs, and grain sizes larger than Ms.

4.3 Sedimentary facies identification

In the five cores where we conducted XRF scanning, the Log(Ca/Ti) values mostly range from around -2 to 2, while the Log(Zr/Rb) values range from around -1 to 1.5 (see Appendix 3-12). The consistent behavior of the elemental signals confirms the applicability of these proxies in our study area, allowing us to classify and compare the signals in different cores (Bloemsma et al., 2012; Davies et al., 2015).

The initial sedimentary facies identification primarily according to lithofacies analysis. Subsequently, we examine whether the preliminary sedimentary facies can be correlated with the characteristic features observed in the Log(Ca/Ti) signals. For example, even within the same massive mud facies (Mm), there may be differences in values that could influence the accuracy of sedimentary facies classification. Furthermore, the sedimentary facies inferred from the Log(Ca/Ti) values are strengthened by incorporating additional proxy such as elemental carbon and grain size proxy.

Ultimately, we suggested that the paleoenvironment in this area underwent a transition from a shallow marine barrier island depositional system to a terrestrial fluvial depositional system. Based on the signals, we classified the sedimentary facies into eight

doi:10.6342/NTU202302306

categories: floodplain, fluvial channel, tidal creek, marsh, lagoon, tidal flat, washover fans, and tidal inlet.

4.3.1 Terrestrial fluvial system facies

4.3.1.1 Floodplain facies

The sediment primarily consists of massive mud (Mm) and mottled massive mud (Mmt), occasionally with a small amount of massive sand (Sm) present. The sandy deposits are likely associated with crevasse splays, while the mud content is derived from abandoned river channels and backswamps (cf. Miall, 1977, 1996). In the Log(Ca/Ti) data, apart from occasional increases due to calcareous concretions within the mud, the values generally remain low. They typically fall below 0, with values below -1 observed in the mottled massive mud, reflecting a predominantly terrestrial environment. In terms of TOC, only the deep brown mud layer shows a higher value of 0.8 %, while the rest are below 0.4%. Similarly, the TOC to TN ratio follows the same trend as TOC, with a noticeable increase above 12 at the 0.8 % layer, indicating a more terrestrial environment.

doi:10.6342/NTU202302306

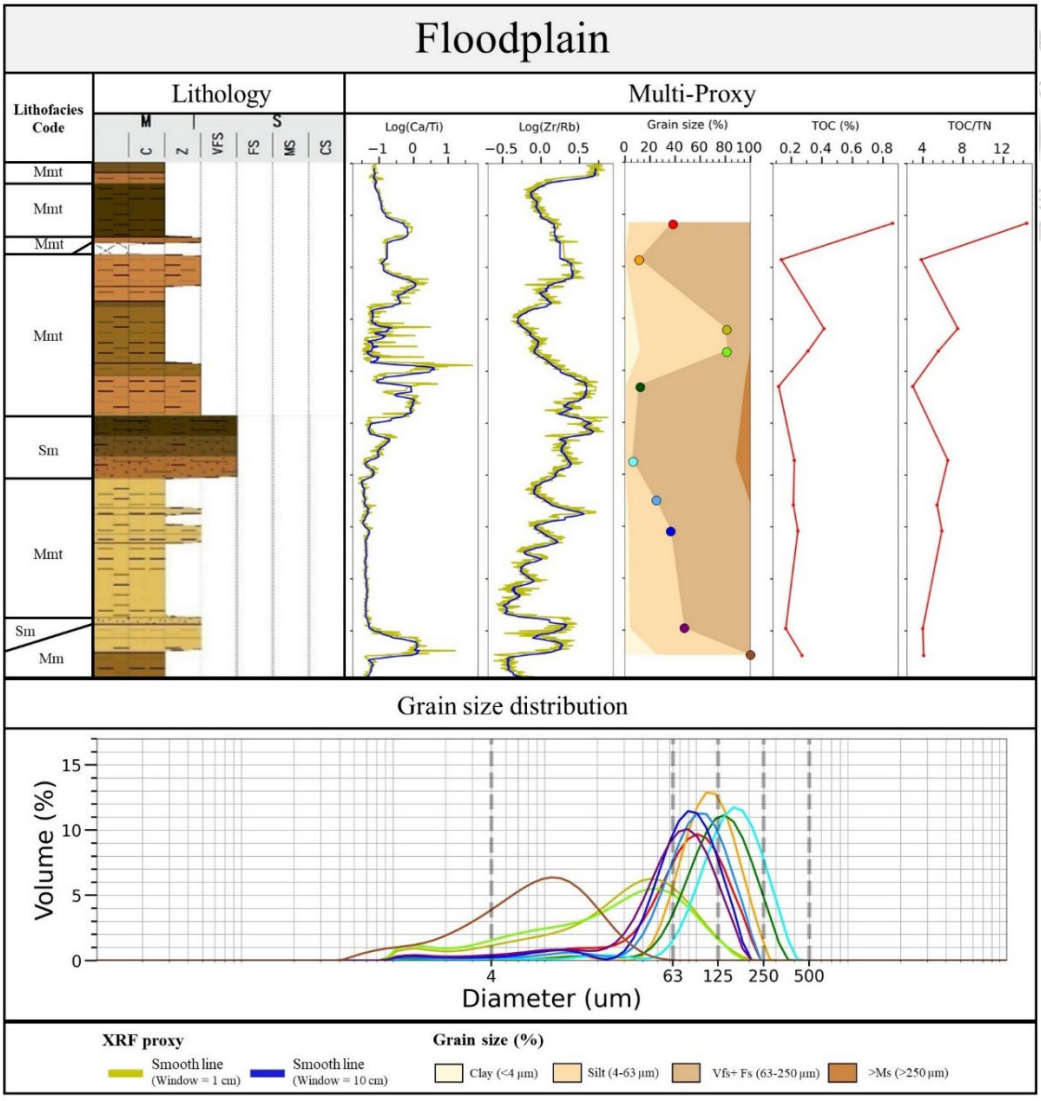

Figure 4.6 Floodplain facies. From left to right, the columns represent the lithofacies code, lithology, Log(Ca/Ti), Log(Zr/Rb), grain size percentage (%), TOC (%), and TOC/TN. The different colors in the grain size distribution chart below the table correspond to the grain size percentage (%) at various points on the graph. The smooth window with 1 cm and 10 cm are represented by yellow line and blue line. The color gradient from light to dark orange is used to represent the gradation from fine to coarse grain sizes. The sediment is classified into the following categories: clay, silt, the combination of Vfs and Fs, and grain sizes larger than Ms.

doi:10.6342/NTU202302306

4.3.1.2 Fluvial channel facies

The sediment primarily consists of fining-upward sand (Su), horizontally bedded sand (Sh), massive sand (Sm), and ripple cross-laminated sand (Sr), with occasional interbeds of cross-bedded sand (Sx). Notably, the lithofacies Su might indicate the channel or sandbank environment (Walker, 1984). In the Log(Ca/Ti) data, values typically range from 0 to 1, with higher values observed in floodplain deposits. The grain size proxy reveals similar fining-upward sequences as the lithology, with Log(Zr/Rb) transitioning from around 0.5 to 0, and an increasing proportion of silt and clay in the grain composition. Regarding TOC, the values are consistently low, all below 0.2 %. Similarly, the TOC/TN ratio also remains relatively low, with the maximum value not exceeding 5.

doi:10.6342/NTU202302306

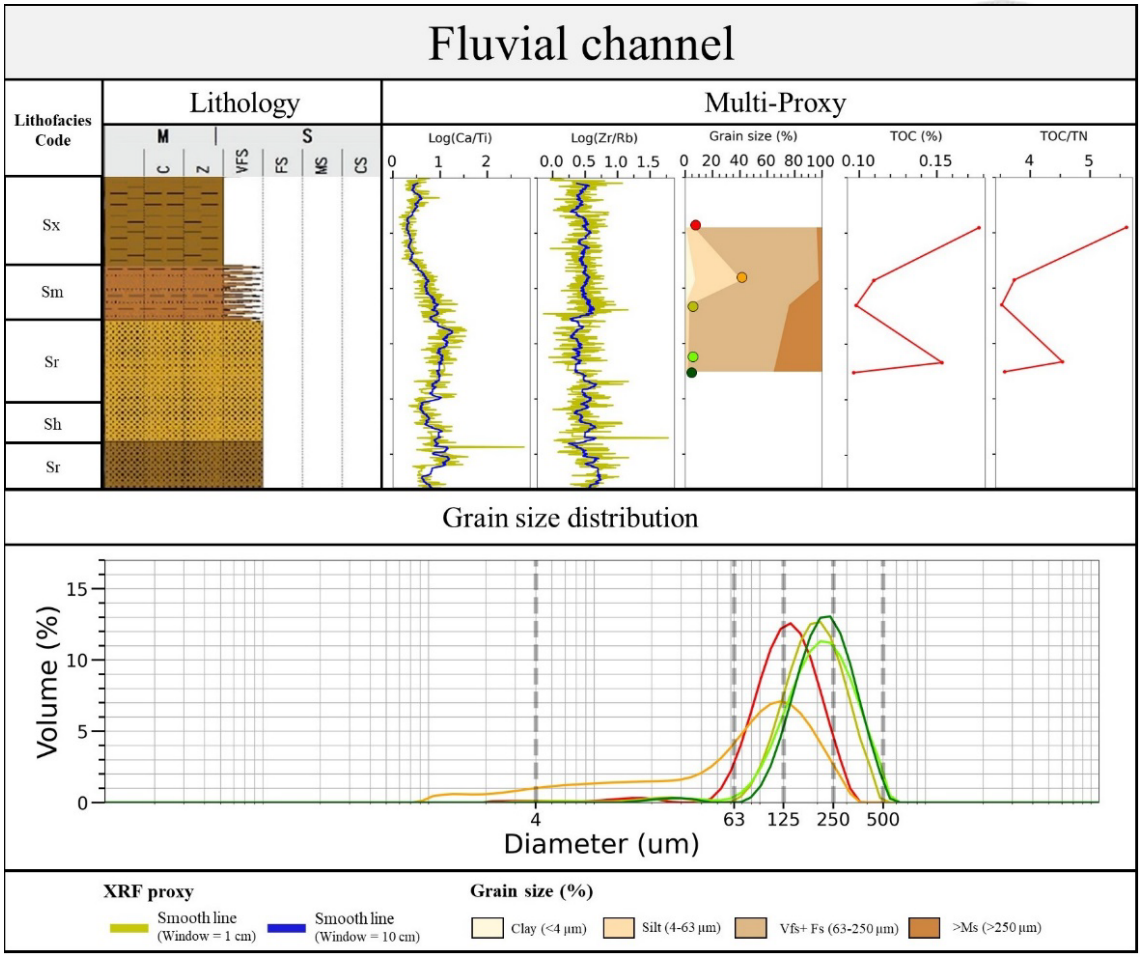

Figure 4.7 Fluvial channel facies. From left to right, the columns represent the lithofacies code, lithology, Log(Ca/Ti), Log(Zr/Rb), grain size percentage (%), TOC (%), and TOC/TN. The different colors in the grain size distribution chart below the table correspond to the grain size percentage (%) at various points on the graph. The smooth window with 1 cm and 10 cm are represented by yellow line and blue line. The color gradient from light to dark orange is used to represent the gradation from fine to coarse grain sizes. The sediment is classified into the following categories: clay, silt, the combination of Vfs and Fs, and grain sizes larger than Ms.

doi:10.6342/NTU202302306

4.3.2 Barrier island system facies

4.3.2.1 Tidal creek (or tidal channel)

The sediment primarily consists of horizontally bedded sand (Sh), massive sand (Sm), cross-bedded sand (Sx), and fossil-bearing sand (Sf), with occasional bioturbated mud (Mb) and erosional sand-mud interbed (SMe). This facies closely resembles fluvial deposits but the presence of biogenic fossils indicates a more marine-influenced environment. Intermittent high-energy erosional sand-mud interbeds (SMe), commonly associated with tidal flats are present. They often occur adjacent to terrestrial floodplain or coastal marsh facies (cf. Olsen et al., 1999). In the Log(Ca/Ti) data, there is a relatively discontinuous relationship with the fluvial facies, and the values in this section can rapidly reach 2. In the grain size proxy, Log(Zr/Rb) exhibits larger fluctuations and can exceed 0.5 when entering the fine sand range but exhibit greater noise. Indicating that the trend doesn't correlate well with the lithology or grain size distribution above the fine sand level, indicating insensitivity to particles larger than fine sand.

The grain size composition shows a higher proportion of medium sand and above, reaching up to 55%. The dark green point displays a uniform grain size composition, corresponding to a diverse grain size distribution. This suggests the influence of tidal action and the presence of multiple lithological components. In terms of TOC, it is

doi:10.6342/NTU202302306

estimated that the marine environment is entered, with values below 0.2 %. Similarly, the TOC/TN ratio does not exceed 4.

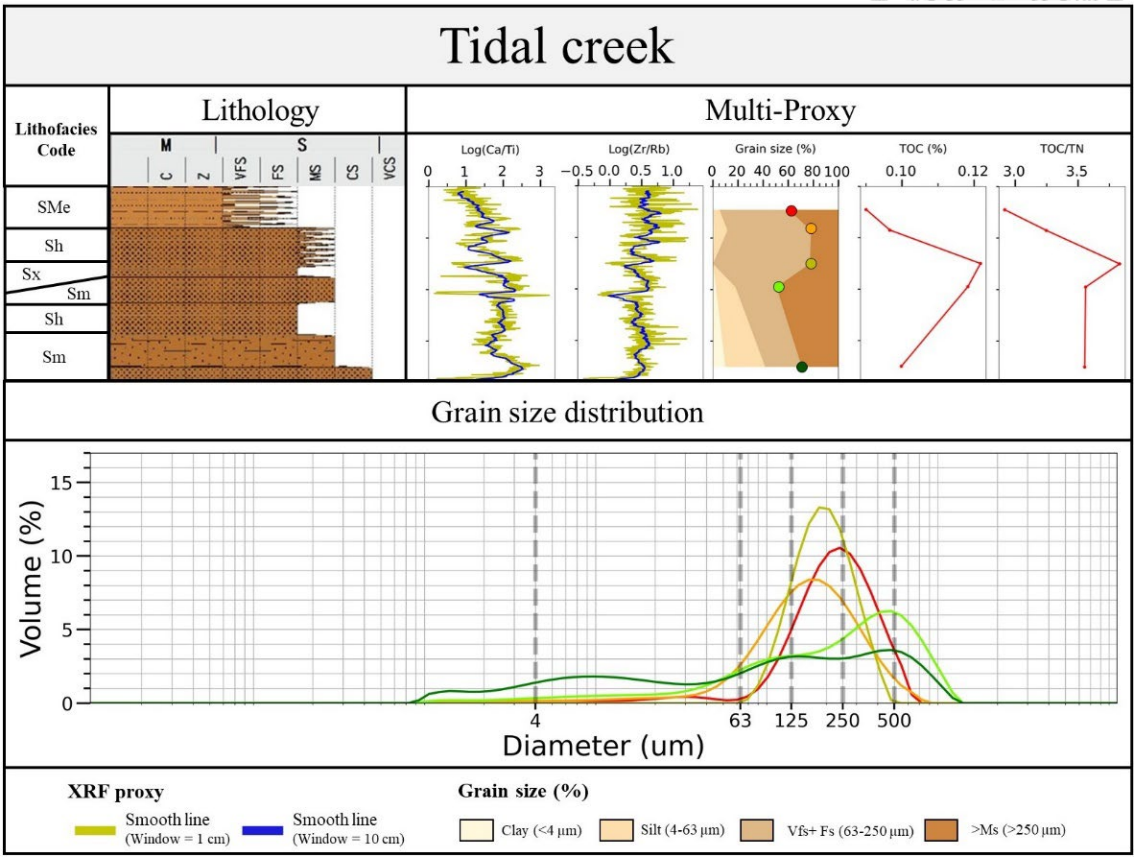

Figure 4.8 Tidal creek facies. From left to right, the columns represent the lithofacies code, lithology, Log(Ca/Ti), Log(Zr/Rb), grain size percentage (%), TOC (%), and TOC/TN. The different colors in the grain size distribution chart below the table correspond to the grain size percentage (%) at various points on the graph. The smooth window with 1 cm and 10 cm are represented by yellow line and blue line. The color gradient from light to dark orange is used to represent the gradation from fine to coarse grain sizes. The sediment is classified into the following categories: clay, silt, the combination of Vfs and Fs, and grain sizes larger than Ms.

doi:10.6342/NTU202302306

4.3.2.2 Marsh

The sediment is primarily composed of carbon-bearing mud (Mc), massive mud (Mm), and bioturbated mud (Mb), with occasional interbeds of fossil-bearing mud (Mf) and ripple cross-laminated mud (Mr). This facies is typically found above the tidal flat and along the margins of the lagoon. Being situated more inland or sheltered by barrier islands allows for the development of marshes (Reineck & Singh, 1980). In the Log(Ca/Ti) data, values for the marsh facies are mostly below 0 and sometimes even reach -1, indicating a sedimentary environment closer to the terrestrial realm. In the grain size proxy, Log(Zr/Rb) tends to be lower, around -0.5, indicating finer particles. Furthermore, Log(Zr/Rb) maintains good sensitivity in the silt-mud interbed layer, clearly demonstrating grain size transitions. The grain size composition is similar to floodplain deposits, with mud and silt accounting for nearly 80%. Elevated TOC and TOC/TN values can also be observed, suggesting higher organic content in the organic-rich mud.

doi:10.6342/NTU202302306

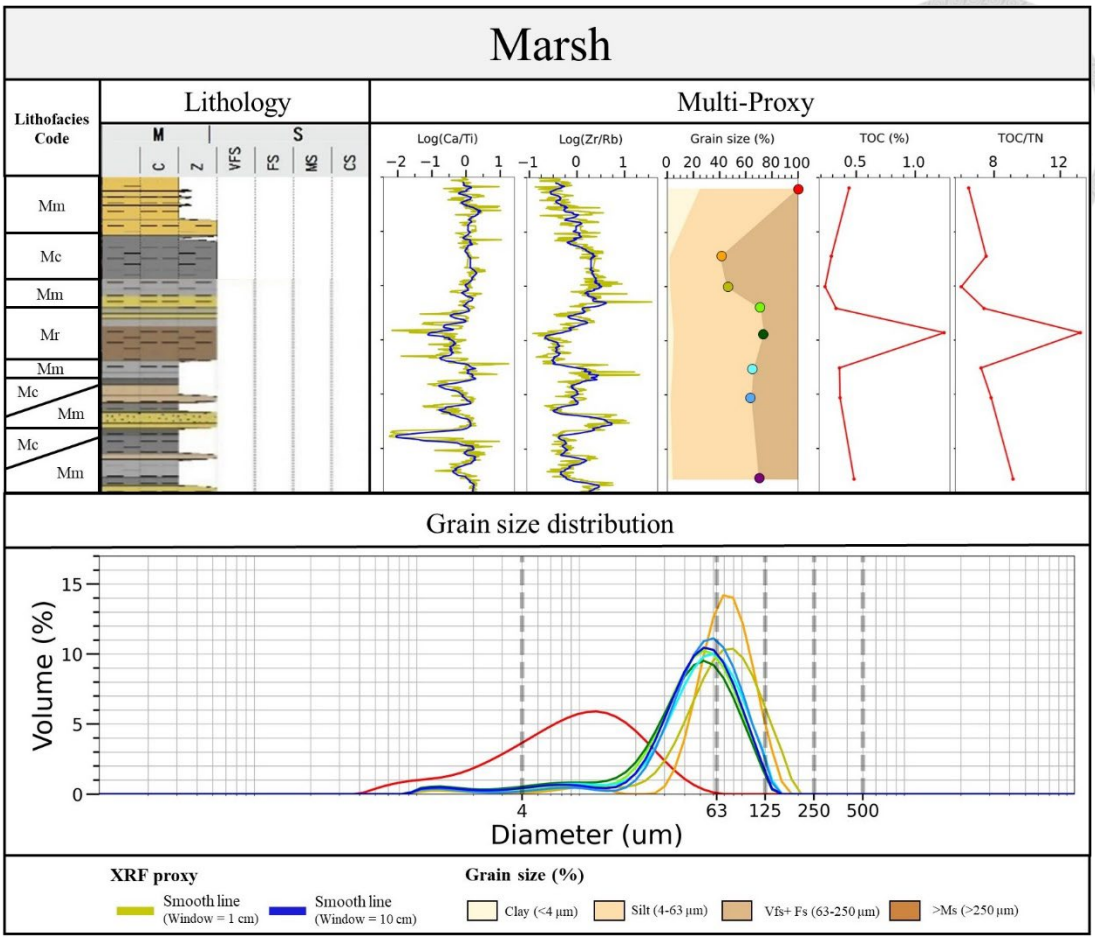

Figure 4.9 Marsh facies. From left to right, the columns represent the lithofacies code, lithology, Log(Ca/Ti), Log(Zr/Rb), grain size percentage (%), TOC (%), and TOC/TN. The different colors in the grain size distribution chart below the table correspond to the grain size percentage (%) at various points on the graph. The smooth window with 1 cm and 10 cm are represented by yellow line and blue line. The color gradient from light to dark orange is used to represent the gradation from fine to coarse grain sizes. The sediment is classified into the following categories: clay, silt, the combination of Vfs and Fs, and grain sizes larger than Ms.

doi:10.6342/NTU202302306

4.3.2.3 Lagoon

The sediment primarily consists of massive mud (Mm), bioturbated mud (Mb), ripple cross-laminated mud (Mr), with occurrences of fossil-bearing mud (Mf), massive sand (Sm), ripple cross-laminated sand (Sr), and erosional sand-mud interbed (SMe). This facies represents deposition in a relatively quiet environment with moderate bioturbation. Additionally, lagoon facies often exhibit overlaps with various environmental settings, including the sand flats and washover fans deposits for the sandy component, mud flats and organic-rich marsh deposits for the muddy component (cf. Boothroyd et al., 1985; Hennessy & Zarillo, 1987). In the Log(Ca/Ti) data, values for the lagoon facies are predominantly below 0, even reaching as low as -1.5. For Log(Zr/Rb), values tend to be above 0, suggesting the dominance of clayey silt or silty clay sediments. Notably, an evident increase in Log(Zr/Rb) occurs in intervals with silt and very fine sand interbed. By observing the grain size composition, it is evident that clay and silt dominate the lagoon facies, accounting for nearly 70% in most intervals. This suggests that the lower Log(Ca/Ti) values are likely a result of the predominance of muddy sediments derived from marshes closer to the landward side. Regarding total organic carbon (TOC), no significantly high values are observed, with most values below 0.4 %. However, where TOC exceeds 0.4% can coincide with finer-grained intervals, and has a relatively higher TOC/TN value around 10.

doi:10.6342/NTU202302306

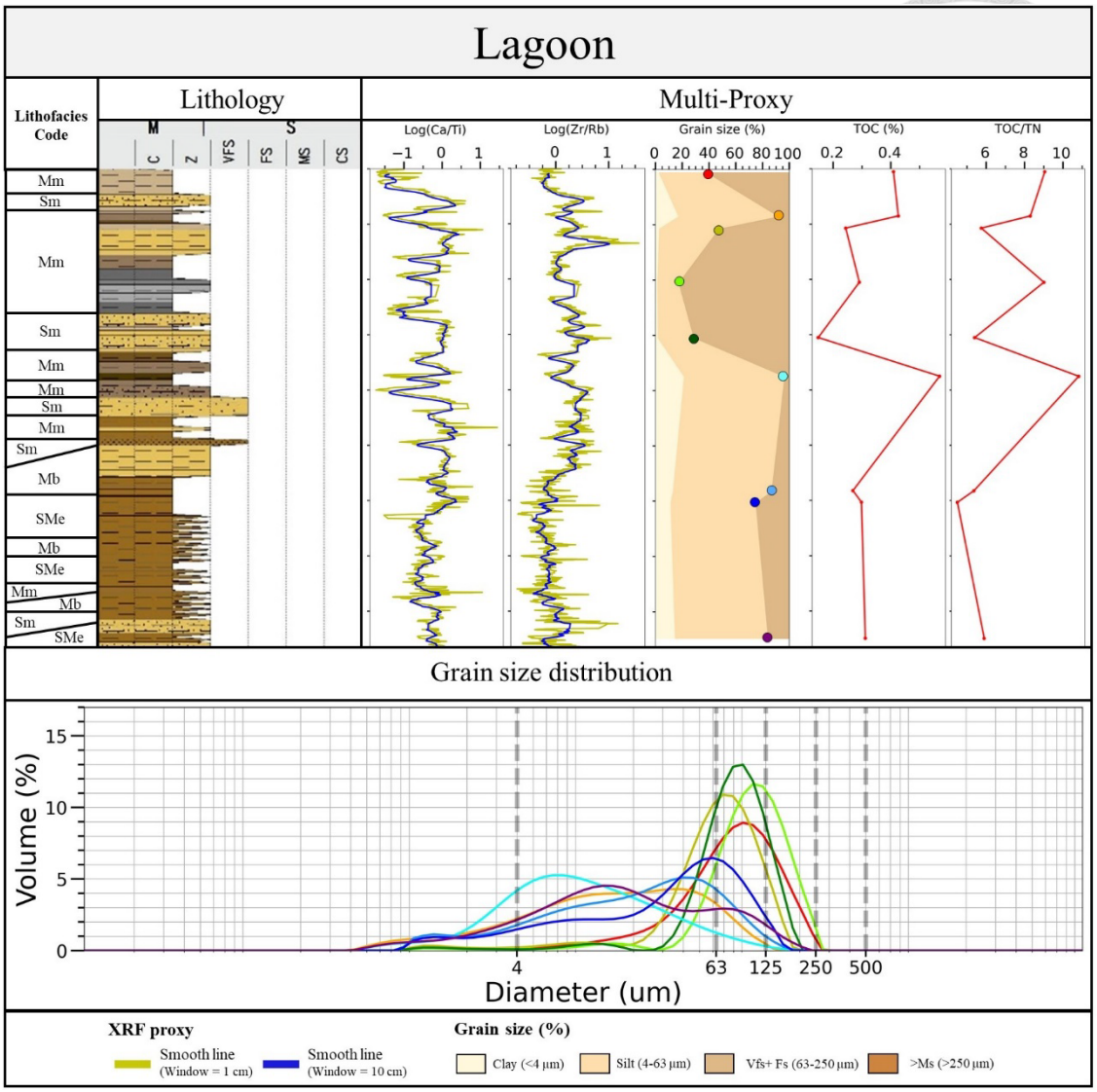

Figure 4.10 Lagoon facies. From left to right, the columns represent the lithofacies code, lithology, Log(Ca/Ti), Log(Zr/Rb), grain size percentage (%), TOC (%), and TOC/TN. The different colors in the grain size distribution chart below the table correspond to the grain size percentage (%) at various points on the graph. The smooth window with 1 cm and 10 cm are represented by yellow line and blue line. The color gradient from light to dark orange is used to represent the gradation from fine to coarse grain sizes. The sediment is classified into the following categories: clay, silt, the combination of Vfs and

doi:10.6342/NTU202302306

Fs, and grain sizes larger than Ms.

4.3.2.4 Tidal flat

The sediment is primarily composed of massive mud (Mm), ripple cross-laminated mud (Mr), and bioturbated mud (Mb), with interbeds of ripple cross-laminated sand (Sr), massive sand (Sm), horizontally bedded sand (Sh), cross-bedded sand (Sx), as well as rhythmic sand-mud interbed (SMr), erosional sand-mud interbed (SMe), carbon-bearing mud (Mc), and fossil-bearing mud (Mf). This facies is distributed between the sheltered zone behind barrier islands and the subtidal zone and can be divided into sand flats and mud flats. Sediment deposition is mainly controlled by tidal processes. In the sand flats, sediment transport occurs through traction, resulting in flattened bedding planes. In the mud flats, finer sediments are deposited through suspension settling, with some influence from wave action, leading to the development of wavy or lenticular textures. The textures commonly exhibit asymmetric patterns, indicating the influence of bidirectional water currents (cf. Klein, 1971; Weimer et al., 1982; Dalrymple et al., 1992).

In the Log(Ca/Ti) data, values for the tidal flat facies generally range from 0 to 0.5. However, due to the diverse nature of tidal flats, there may be some variations in the signals between sand flats and mud flats. Nonetheless, intermediate values can still be used to differentiate the tidal flat facies from nearby facies with relatively lower values, such as marsh or lagoon facies. For Log(Zr/Rb), values are typically around 0.5 in very

doi:10.6342/NTU202302306

fine sand intervals, and signals of sand mud interbed can be observed in tidal settings. However, the behavior in fine sand is still somewhat limited, and a clear trend of coarsening cannot be discerned. In terms of grain size composition, intermittent occurrences of higher percentages of silt and clay can be observed, indicating the influence of tidal processes in this deposited environment.

TOC values reach up to 0.6 % only in eroded mud layers affected by tidal action, while the rest remain below 0.5 %. In terms of the TOC/TN, the values in this section generally range between 4 and 8.

doi:10.6342/NTU202302306

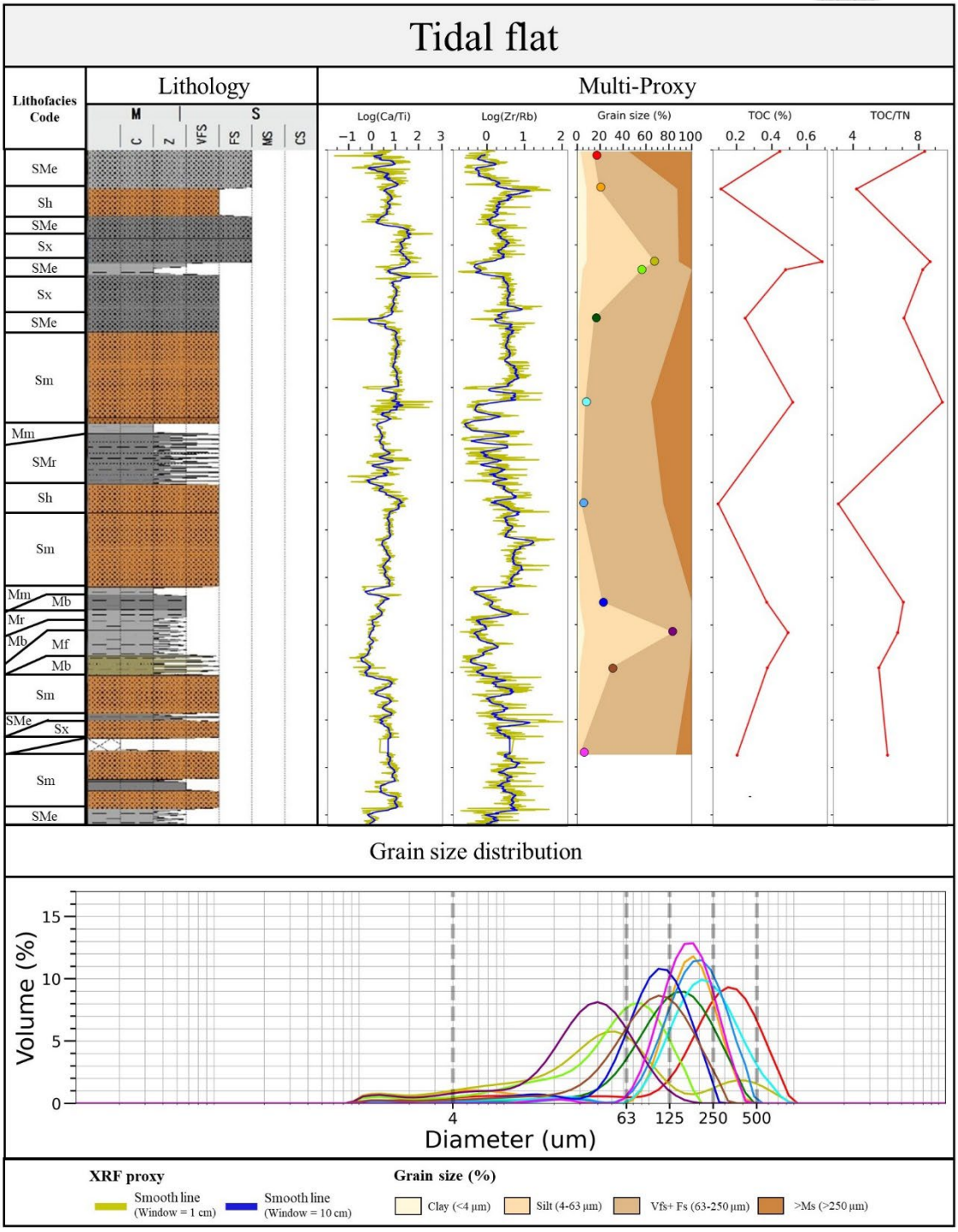

Figure 4.11 Tidal flat facies. From left to right, the columns represent the lithofacies code, lithology, Log(Ca/Ti), Log(Zr/Rb), grain size percentage (%), TOC (%), and TOC/TN. The different colors in the grain size distribution chart below the table correspond to the grain size percentage (%) at various points on the graph. The smooth window with 1 cm

doi:10.6342/NTU202302306

and 10 cm are represented by yellow line and blue line. The color gradient from light to dark orange is used to represent the gradation from fine to coarse grain sizes. The sediment is classified into the following categories: clay, silt, the combination of Vfs and Fs, and grain sizes larger than Ms.

4.3.2.5 Washover fan

The sediment is primarily composed of horizontally bedded sand (Sh), massive sand (Sm), ripple cross-laminated sand (Sr), and cross-bedded sand (Sx), with interbeds of fossil-bearing sand (Sf), carbon-bearing mud (Mc), rhythmic sand-mud interbed (SMr), or erosional sand-mud interbed (SMe). This facies is formed when storm surge waves cut through or overtop barrier islands, leading to the deposition of elongated leaf-shaped or tabular sand layers extending into the lagoon. The continuous action of storms helps increase the width of the barrier island or provide a suitable environment for marsh growth (cf. Schwartz, 1982; Thorbjarnarson et al., 1985; Reinson, 1992).

In the Log(Ca/Ti) data, the facies values are relatively stable, ranging from approximately 0.3 to 0.5, which is likely attributed to the sheltering effect of the barrier island. Log(Zr/Rb) mostly remains around 0.5, with occasional intervals showing values dropping to around -0.25 in the presence of sand-mud interbeds. In terms of grain size composition, the facies is dominated by very fine sand and fine sand, accounting for a high percentage of approximately 80%.

doi:10.6342/NTU202302306

In terms of TOC, organic mud layers within the very fine sand layers exhibit a TOC content greater than 1%, indicating a relatively calm marsh environment behind the barrier islands with limited sand supply from the sand bar and shoreface sediments. For TOC/TN, it follows a similar trend as TOC, suggesting a significant terrestrial organic matter source within the organic mud intervals.

Notably, the washover fan facies is the crucial facies in our study, its flattened signal can be recognized apparently in each core. This facies also indicates the wave action by the process of transgression, maximum flooding surface can be determined around the bottom of this facies.

doi:10.6342/NTU202302306

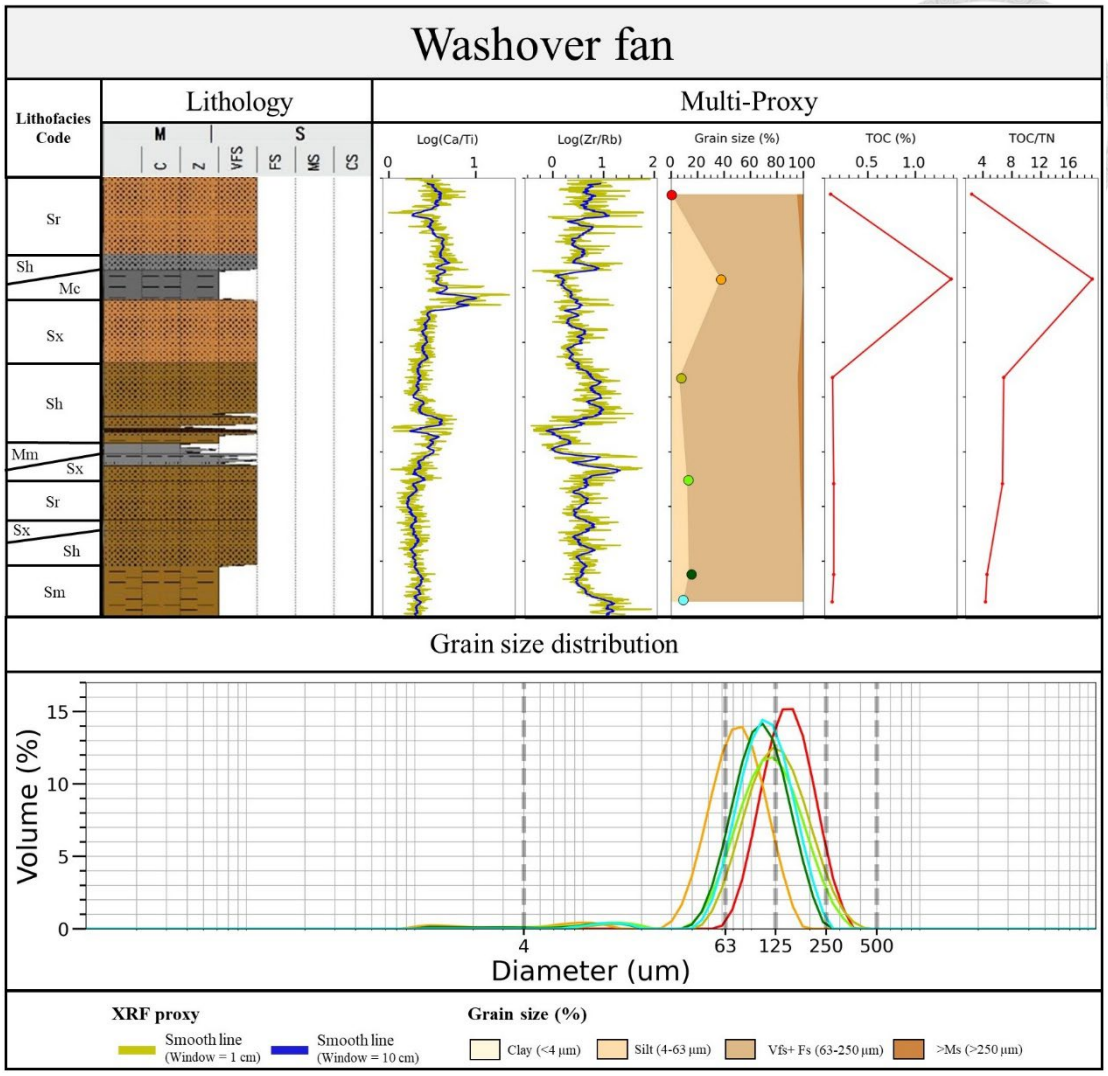

Figure 4.12 Washover fan facies. From left to right, the columns represent the lithofacies code, lithology, Log(Ca/Ti), Log(Zr/Rb), grain size percentage (%), TOC (%), and TOC/TN. The different colors in the grain size distribution chart below the table correspond to the grain size percentage (%) at various points on the graph. The smooth window with 1 cm and 10 cm are represented by yellow line and blue line. The color gradient from light to dark orange is used to represent the gradation from fine to coarse grain sizes. The sediment is classified into the following categories: clay, silt, the combination of Vfs and Fs, and grain sizes larger than Ms.

doi:10.6342/NTU202302306

4.3.2.6 Tidal inlet

The sediment is mainly composed of massive sand (Sm), cross-bedded sand (Sx), horizontally bedded sand (Sh), and ripple cross-laminated sand (Sr), with interbeds of fossil-bearing sand (Sf) and bioturbated mud (Mb). This facies represents a passage from the barrier island system to the open ocean (cf. De Swart & Zimmerman, 2008), similar to fluvial channels and tidal creeks, but with a higher abundance of fossilized shells and bioturbation. In the Log(Ca/Ti) data, the values are generally greater than 0.5 and can reach up to 1.5. The signal differs from the relatively stable high values observed in tidal creeks. Log(Zr/Rb) also exhibits higher values, mostly above 0.75 and reaching up to 1.25, indicating a relatively coarser grain size. The grain size composition shows a higher proportion of medium sand and coarser particles, as well as the presence of finer particles in the bioturbated mud (Mb) component. For The TOC content is relatively low, with values below 0.2%, and TOC/TN follows a similar trend to TOC.

doi:10.6342/NTU202302306

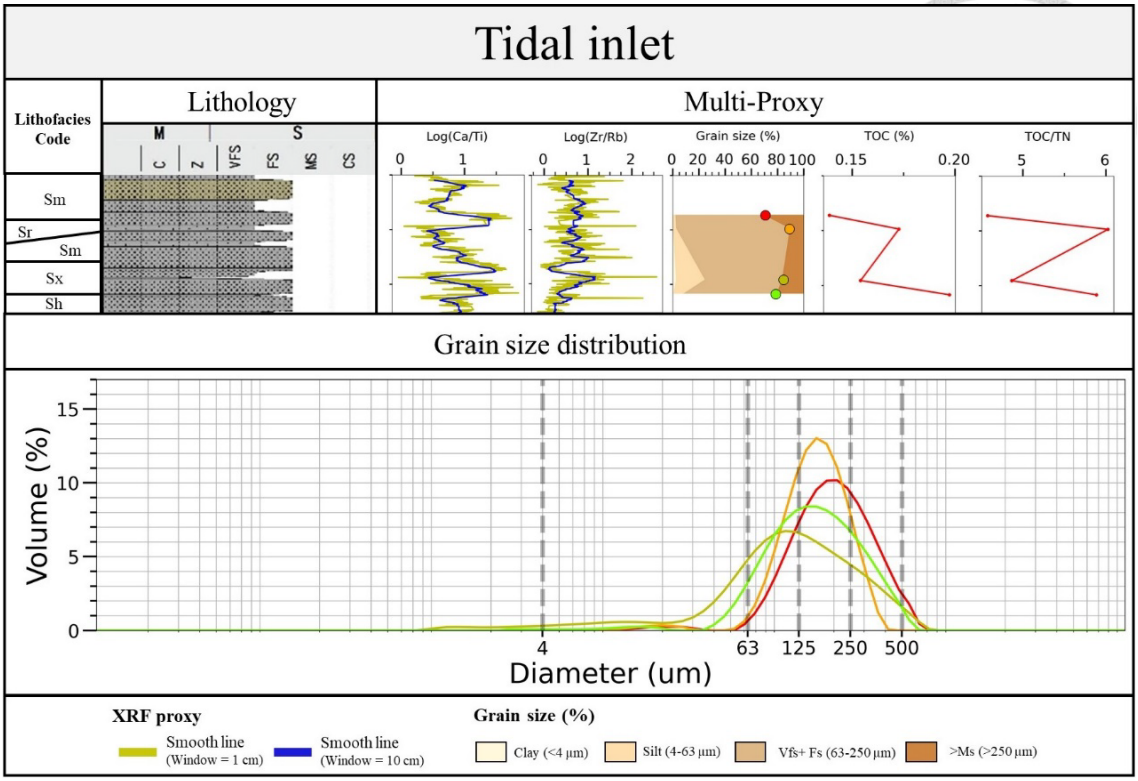

Figure 4.13 Tidal inlet facies. From left to right, the columns represent the lithofacies code, lithology, Log(Ca/Ti), Log(Zr/Rb), grain size percentage (%), TOC (%), and TOC/TN. The different colors in the grain size distribution chart below the table correspond to the grain size percentage (%) at various points on the graph. The smooth window with 1 cm and 10 cm are represented by yellow line and blue line. The color gradient from light to dark orange is used to represent the gradation from fine to coarse grain sizes. The sediment is classified into the following categories: clay, silt, the combination of Vfs and Fs, and grain sizes larger than Ms.

doi:10.6342/NTU202302306

5 Discussion

5.1 XRF proxy validation

Even though previous studies have provided insights into the application of XRF proxy (Richter et al., 2006; Wolters et al., 2010; Turner et al., 2015; Wu et al., 2020), it is crucial to compare them with other experiments to estimate the universality in our research area(Bloemsma et al., 2012).

Regarding Log(Ca/Ti), it exhibits a good correlation with total inorganic carbon($r = 0.67$, $p < 0.0001$), which represents the calcium carbonate, confirming that Ca/Ti can serve as a reliable proxy for marine environments (Figure 5.1).

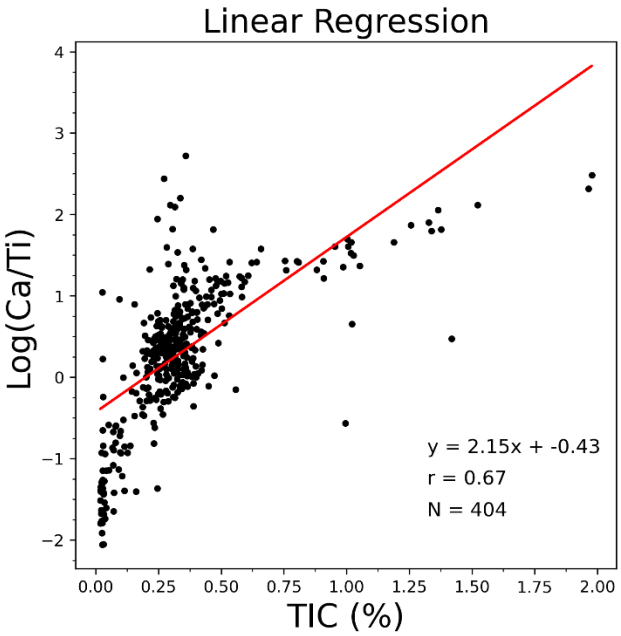

Figure 5.1 Correlation with Log(Ca/Ti) and TIC (%)

For Log(Zr/Rb), we found that the correlation with clay can reach -0.69 ($p < 0.0001$), and has a -0.73 ($p < 0.0001$) with silt, indicating a moderate to high correlation with the

doi:10.6342/NTU202302306

result of grain size analysis. However, as the limitation we encountered during the sedimentary facies identification, Log(Zr/Rb) lacks sensitivity to particles coarser than fine sand, as indicated by the correlation with medium sand in only 0.25. Nonetheless, when we aggregate particles coarser than very fine sand into a broader sand category, the distribution becomes more uniform, and we can still differentiate the particle sizes reasonably well, exhibiting a higher correlation with sand ($r = 0.75$, $p < 0.0001$).

We also discovered a similar correlation when using a sieve with a size of 63 micrometers ($r = 0.74$, $p < 0.0001$), and observed that higher TOC tends to occur more frequently in finer particle segments ($r = -0.69$, $p < 0.0001$), providing valuable sampling references (Figure 5.2).

doi:10.6342/NTU202302306

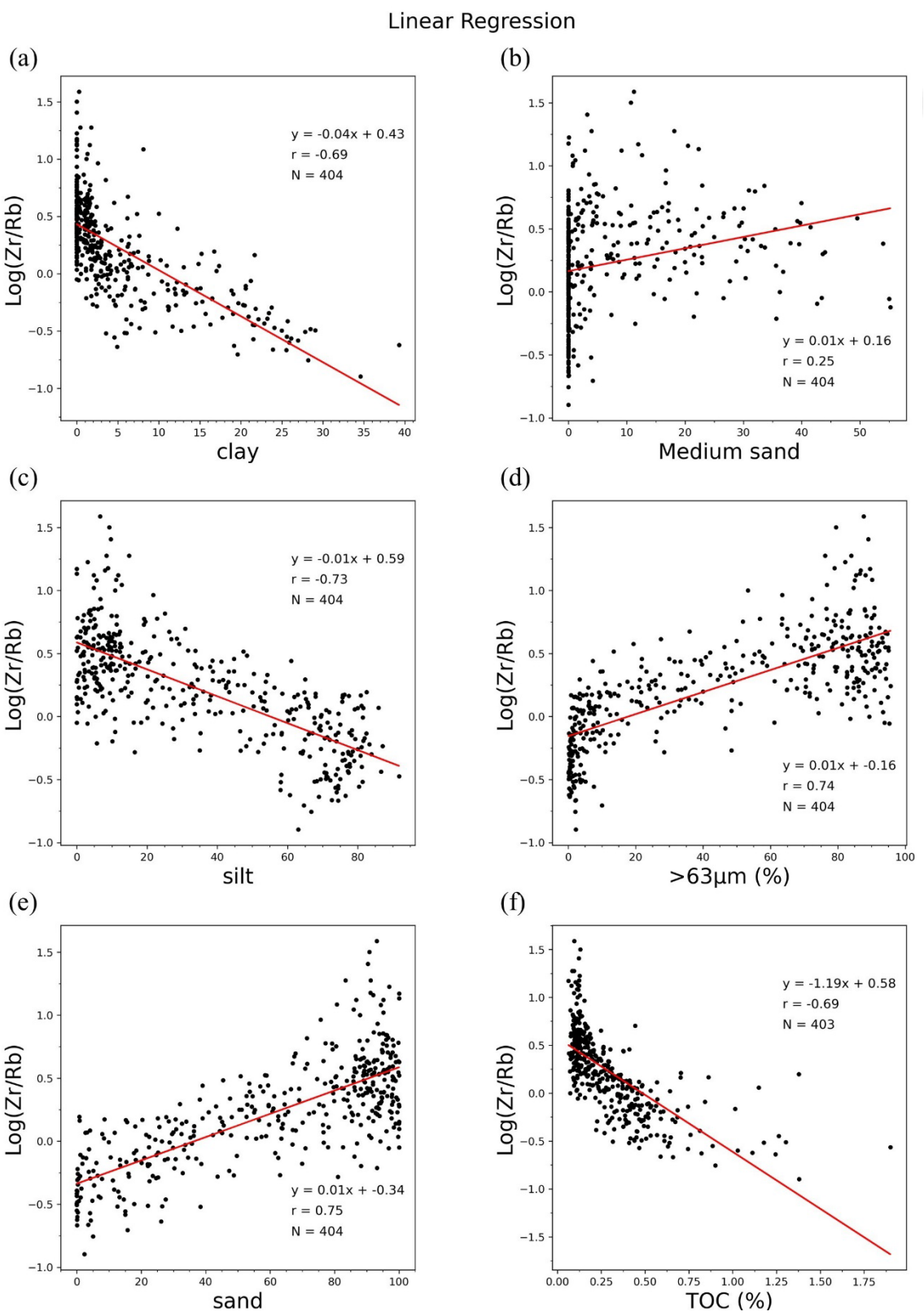

Figure 5.2 Correlation between Log(Zr/Rb) and the grain size distribution, TOC (%). (a) Correlation between Log(Zr/Rb) and clay. (b) Correlation between Log(Zr/Rb) and silt.

doi:10.6342/NTU202302306

(c) Correlation between Log(Zr/Rb) and sand. (d) Correlation between Log(Zr/Rb) and Ms. (e) Correlation between Log(Zr/Rb) and the particle size larger than 63 μm. (f) Correlation between Log(Zr/Rb) and TOC (%).

doi:10.6342/NTU202302306

5.2 Age model

After conducting radiometric dating, it was observed that more reasonable results could be obtained from shell and wood samples, therefore, the significantly older ages obtained from calcareous concretions and peat were removed from the sample list to ensure the acceptable dating results. However, the absolutely dated chronologies cannot be provided by conventional radiocarbon ages, calibrating with the calibration curve is needed to reconstruct the age model. The Marine20 and Intcal20 calibration curve can be used generally for shells and wood sample, but given that our study area corresponds to a barrier island system and terrestrial fluvial sedimentary environment, which is more inclined towards a semi-open marine setting, indicating that the Marine20 calibration curve might not be suitable for our samples. Instead, the Intcal20 calibration curve that integrated the result from both terrestrial and marine samples was adopted for calibrating (Reimer et al., 2020). Calib 8.2 software was employed to calibrate the conventional radiocarbon ages with the calibration curve to acquire the calibrated age (Stuiver & Reimer, 1993), using the High-Probability Density Range Method (HPD) to obtain the calibration ranges with relative probabilities expressed in percentages at the 95.4% (2σ) and 68.2% (1σ) probability levels (see Appendix 1) (Ramsey, 2009).

doi:10.6342/NTU202302306

Table 5.1 Calibrated result

Core	Depth (m)	Calibrated age (cal. yr. BP)	Environment	Sedimentation rate (cm/yr)
690	13.8	3889-3977	Marsh	0.47 ± 0.01
	34.5	8208-8346	Washover fan	
	41.4	8780-8832	Washover fan	1.39 ± 0.25
	46.2	9477-9527	Tidal flats	0.70 ± 0.05
691	11.1	4704-4754	Lagoon	0.45 ± 0.01
	22.9	7325-7364	Marsh	
	36.7	8317-8368	Tidal flats	1.38 ± 0.06
	44.6	9301-9383	Marsh	0.80 ± 0.05
692	19.8	6483-6561	Lagoon	1.20 ± 0.09
	29.8	7335-7384	Tidal flats	
	44.1	9194-9278	Tidal flats	0.76 ± 0.03
699	48.9	9483-9527	Tidal flats	1.30 ± 0.04
	71.7	11227-11281	Tidal flats	
	84.5	11875-12004	Tidal inlet	1.89 ± 0.25
700	48.6	9168-9272	Marsh	1.30 ± 0.27
	56.3	9760-9909	Tidal flats	
	60.6	10499-10574	Tidal flats	0.63 ± 0.10
	63.5	10722-10795	Tidal flats	1.46 ± 0.49
	79.9	11426-11607	Marsh	2.23 ± 0.37

doi:10.6342/NTU202302306

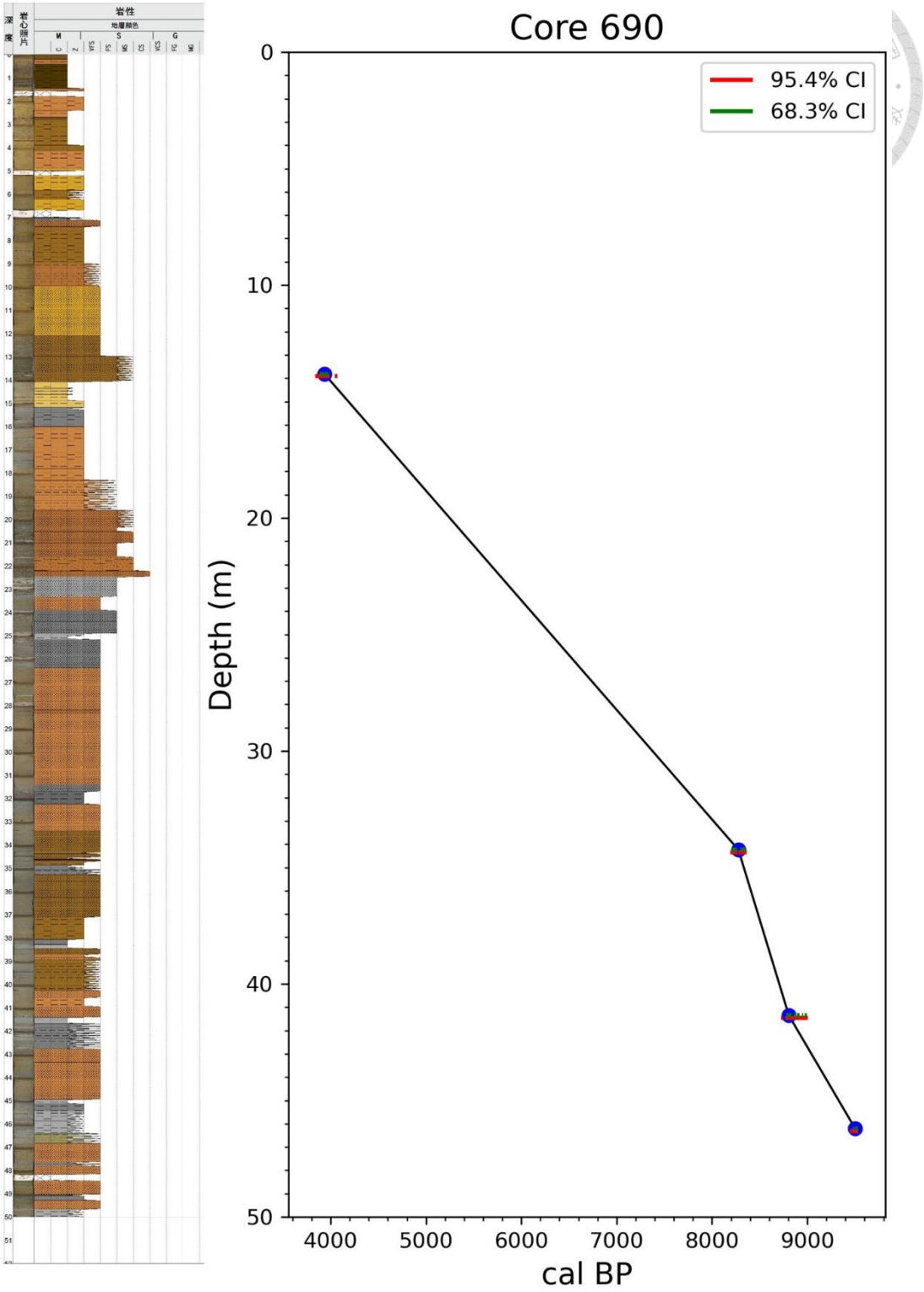

Figure 5.3 Age model of core 690 in 13.8-46.2 m-, covering the age from ca. 3800-9500 cal BP. The red lines represent the 95.4% confidence interval (CI), the green lines represent the 68.3% CI.

doi:10.6342/NTU202302306

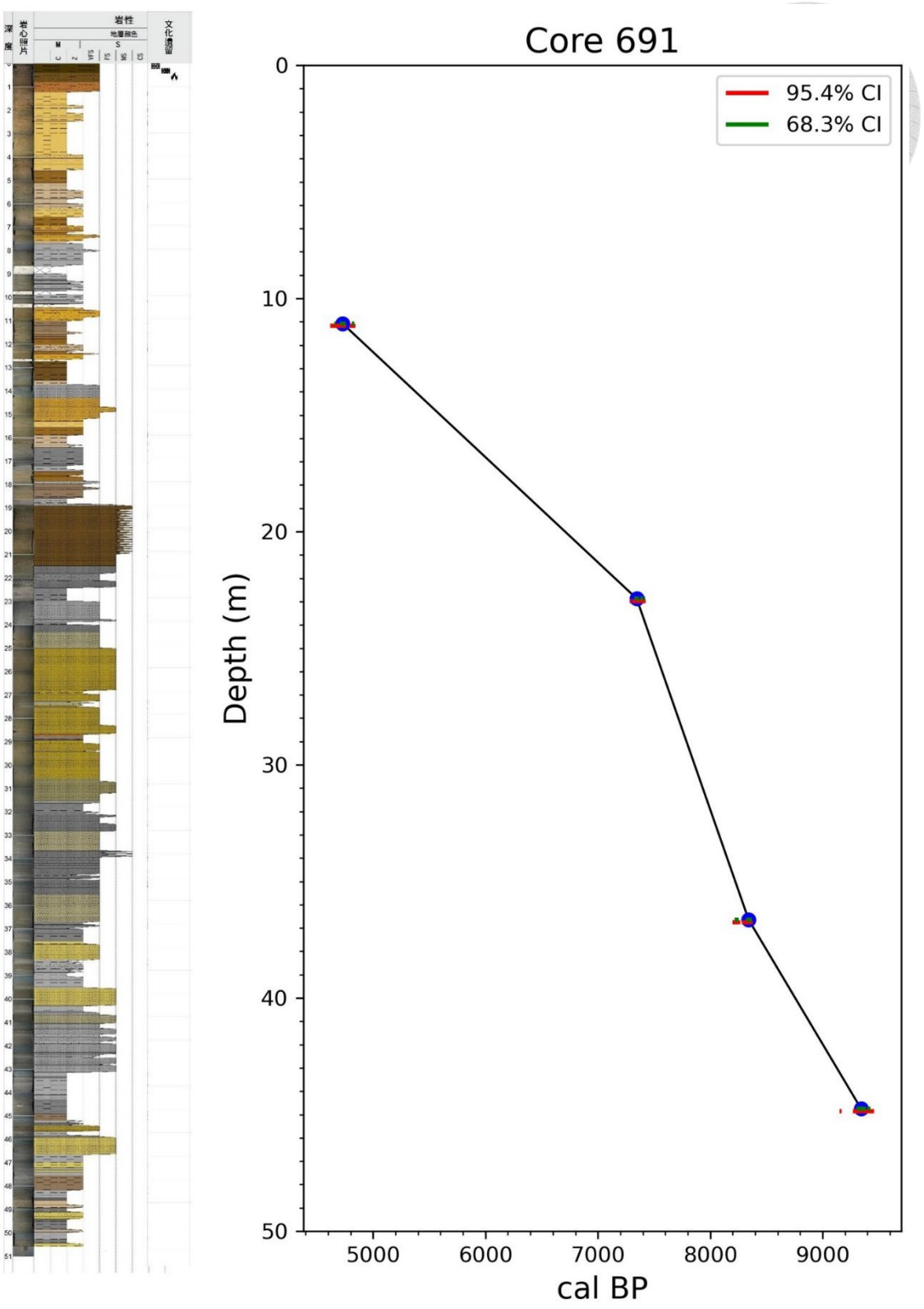

Figure 5.4 Age model of core 691 in 11.1-44.6 m, covering the age from ca. 4700-9400 cal BP. The red lines represent the 95.4% CI, the green lines represent the 68.3% CI.

doi:10.6342/NTU202302306

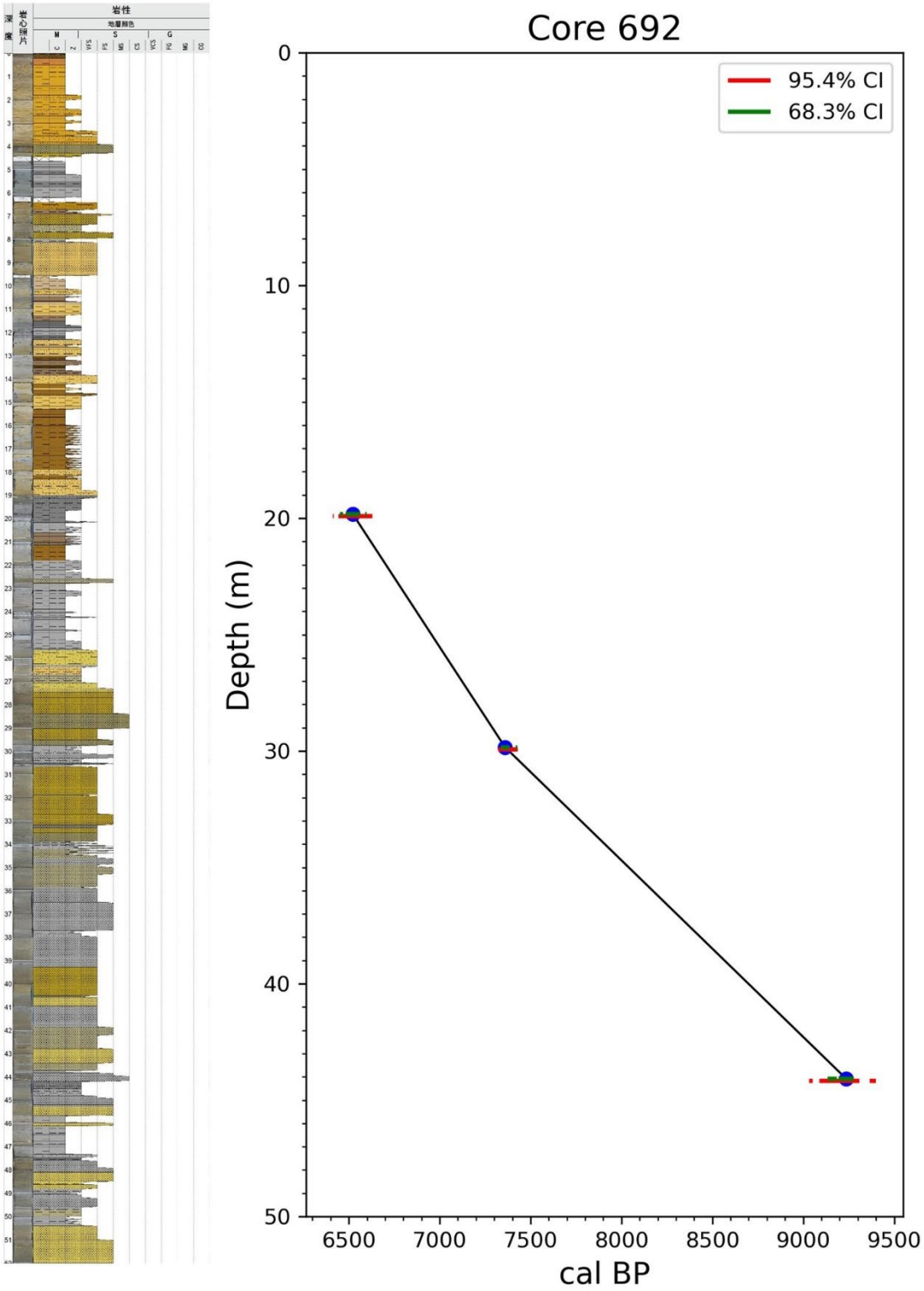

Figure 5.5 Age model of core 692 in 19.8-44.1 m, covering the age from ca. 6500-9300 cal BP. The red lines represent the 95.4% CI, the green lines represent the 68.3% CI.

doi:10.6342/NTU202302306

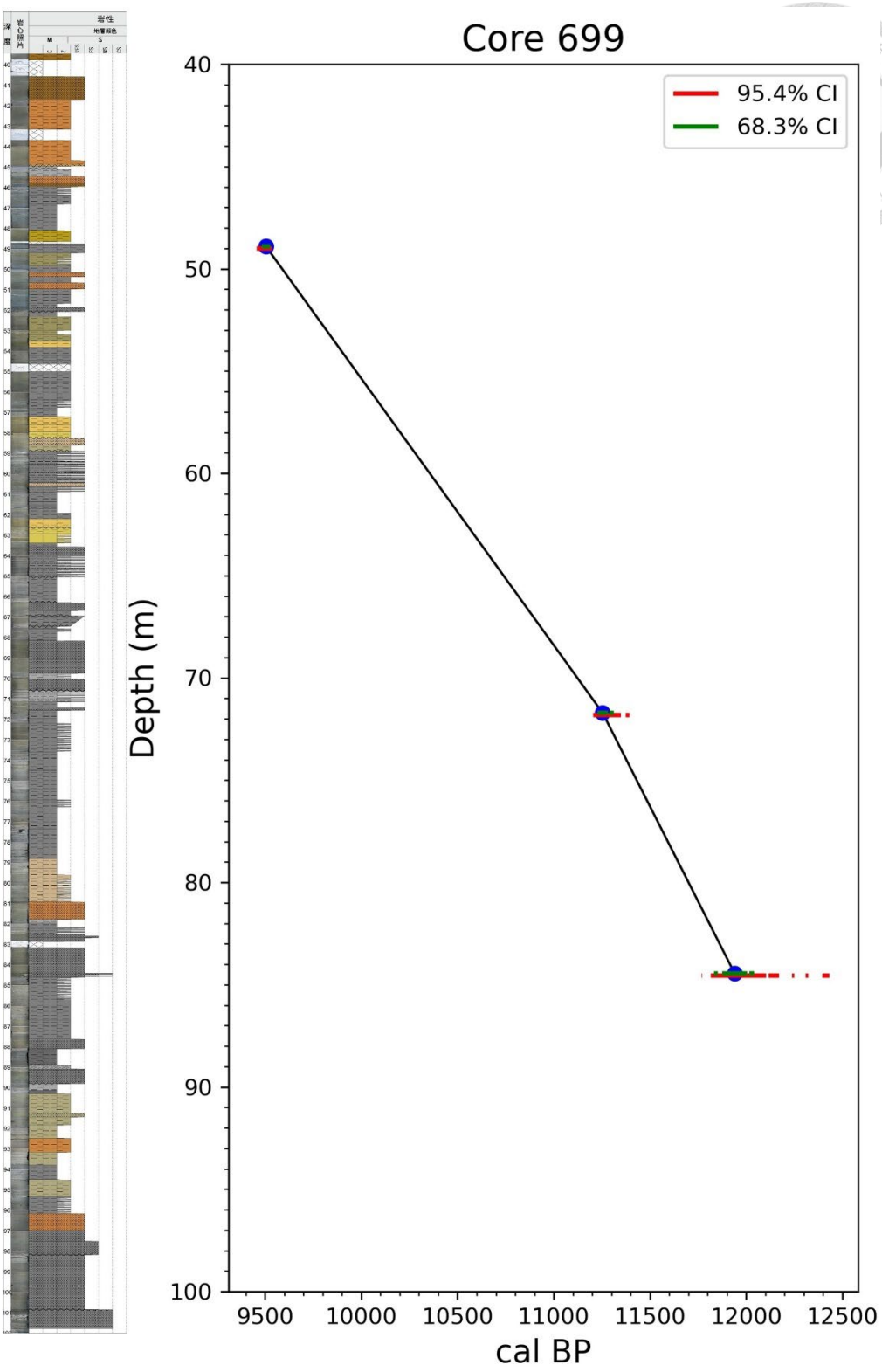

Figure 5.6 Age model of core 699 in 48.9-84.5 m, covering the age from ca. 9500-12000 cal BP. The red lines represent the 95.4% CI, the green lines represent the 68.3% CI.

doi:10.6342/NTU202302306

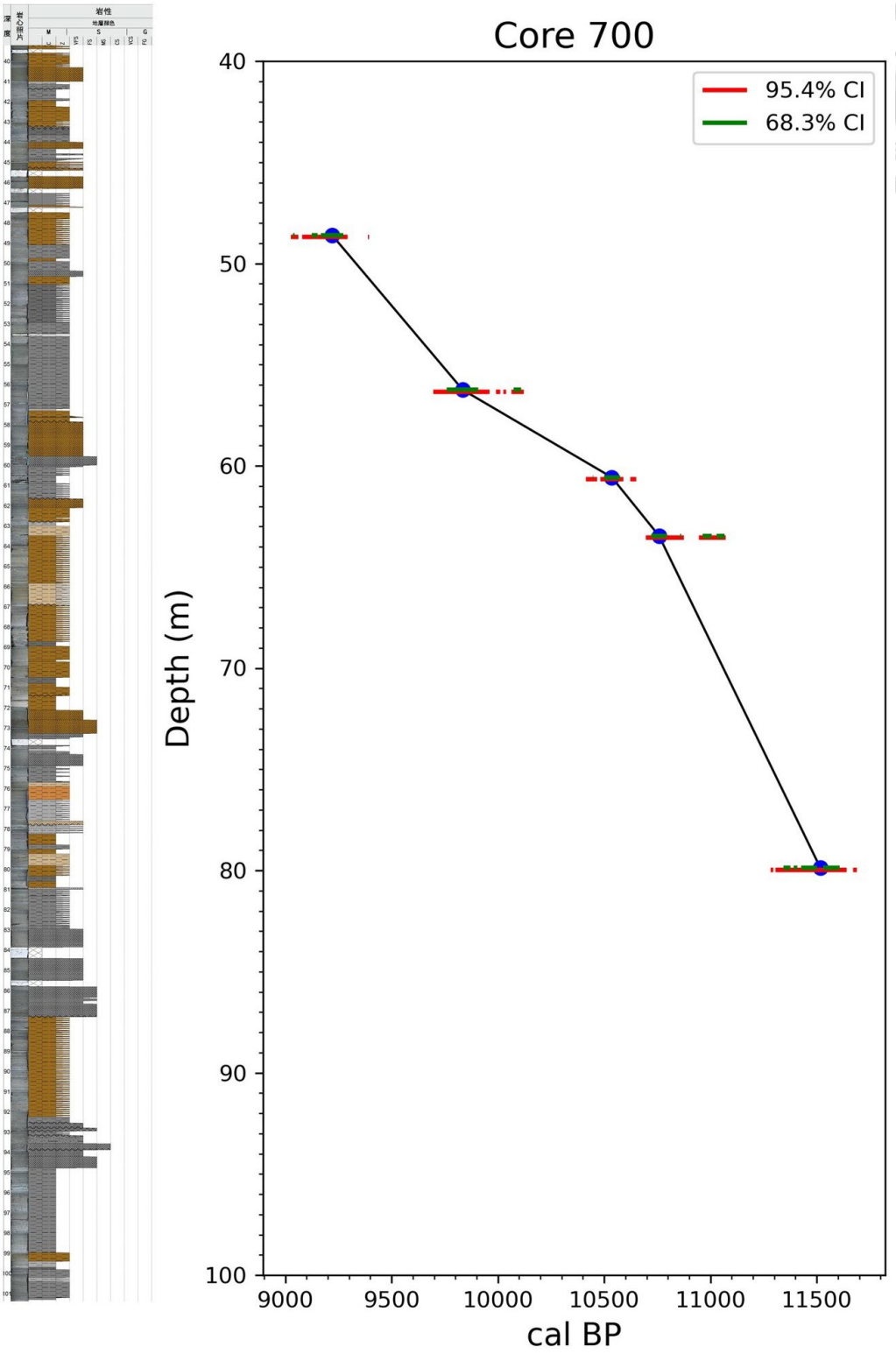

Figure 5.7 Age model of core 700 in 48.9-84.5 m, covering the age from ca. 9200-11600 cal BP. The red lines represent the 95.4% CI, the green lines represent the 68.3% CI.

doi:10.6342/NTU202302306

5.3 Profile comparison

Among the five long sediment cores used for analysis, the time period from 9300 to 4700 cal BP can be established using the 50 m-long Core 690, Core 691, and Core 692. The time period from 9300 to 12000 cal BP can be established using the 100 m-long Core 699 and Core 700. Therefore, we can define the boundary at 9300 cal BP based on these five cores.

Furthermore, within these five long cores located on the western side of the drilling area, a succession of washover fan facies representing transgressive phases that broke through or extended beyond the barrier island has been observed from around 9300 to 7300 cal BP. It can be inferred that the position of the maximum flooding surface lies at the top of these sand bodies, at the boundary between the overwash delta and adjacent tidal flats (Huang, 2001). This depositional facies is highly informative regarding our understanding of the marine influence during the transgressive phase.

Fortunately, as part of the project, two 100 m-long cores and six 50 m-long cores have been drilled, mostly on the eastern side of the drilling area (Figure 5.8). Although these cores have not undergone experiments and lack chronological data, it is still possible to infer changes in the sedimentary environment through the lithofacies analysis. Therefore, a comparison of these eastern cores and the five existing cores can be conducted. A cross-sectional profile can also be plotted to further investigate the extent

doi:10.6342/NTU202302306

of marine incursion since the Holocene.

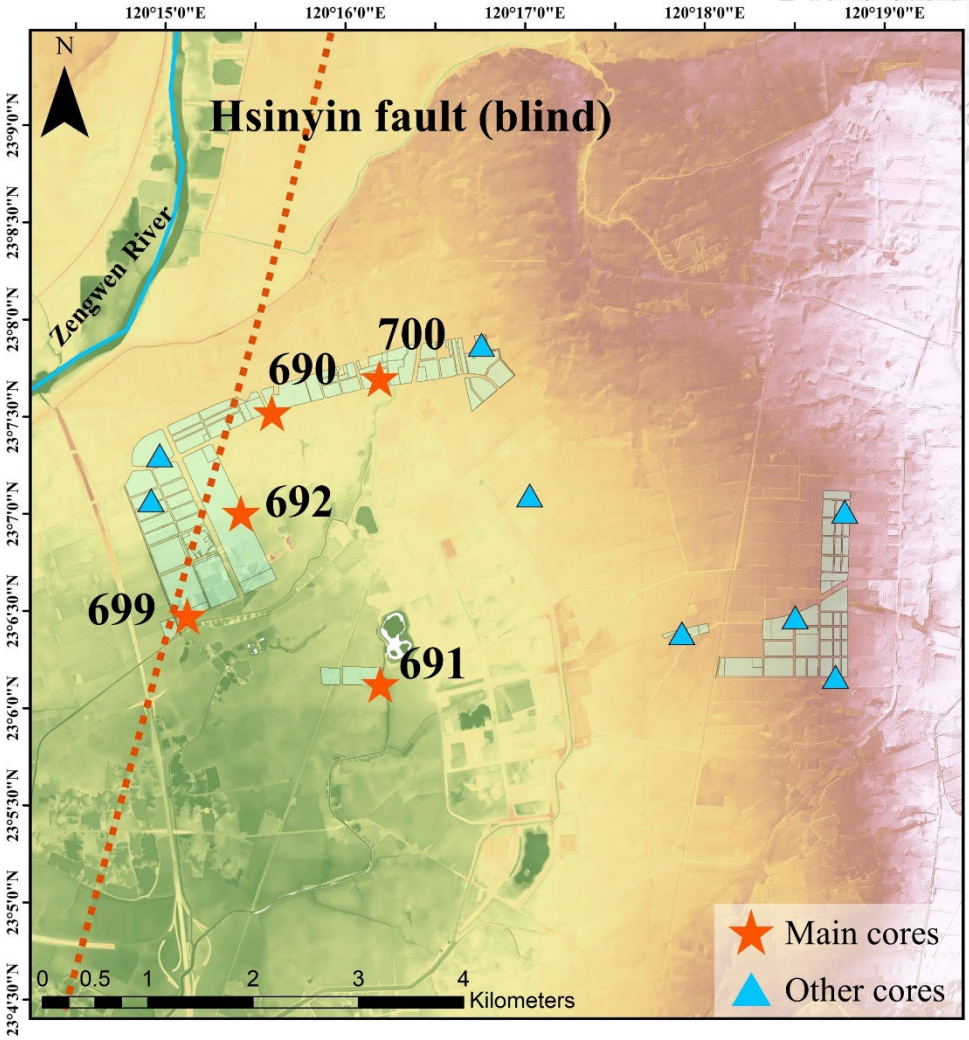

Figure 5.8 Other cores in the drilling area. A 5 m resolution DEM provided by SSC is utilized to represent the elevation changes around the Tainan Science Park. The green polygons represent the drilling area in the AO region, and the main cores for analysis are marked as red stars, the other cores are marked as blue triangles. Hsinyin Fault across the drilling region is adopted from Chen et al. (2004), represented by the red dashed line, and the bold light blue line depicts the Zengwen River.

doi:10.6342/NTU202302306

5.3.1 691-692-690 (Profile A)

Profile A is located on the western side of the drilling area and provides better age control, allowing for the estimation of the probable age of the maximum flooding surface (MFS). Based on the estimation of sedimentation rates, the MFS in core 691 is suggested to be around 9100 cal BP, while in core 692, it occurs at approximately 9300 cal BP. Core 690 reaches the MFS at the latest, around 8800 cal BP (Figure 5.9).

doi:10.6342/NTU202302306

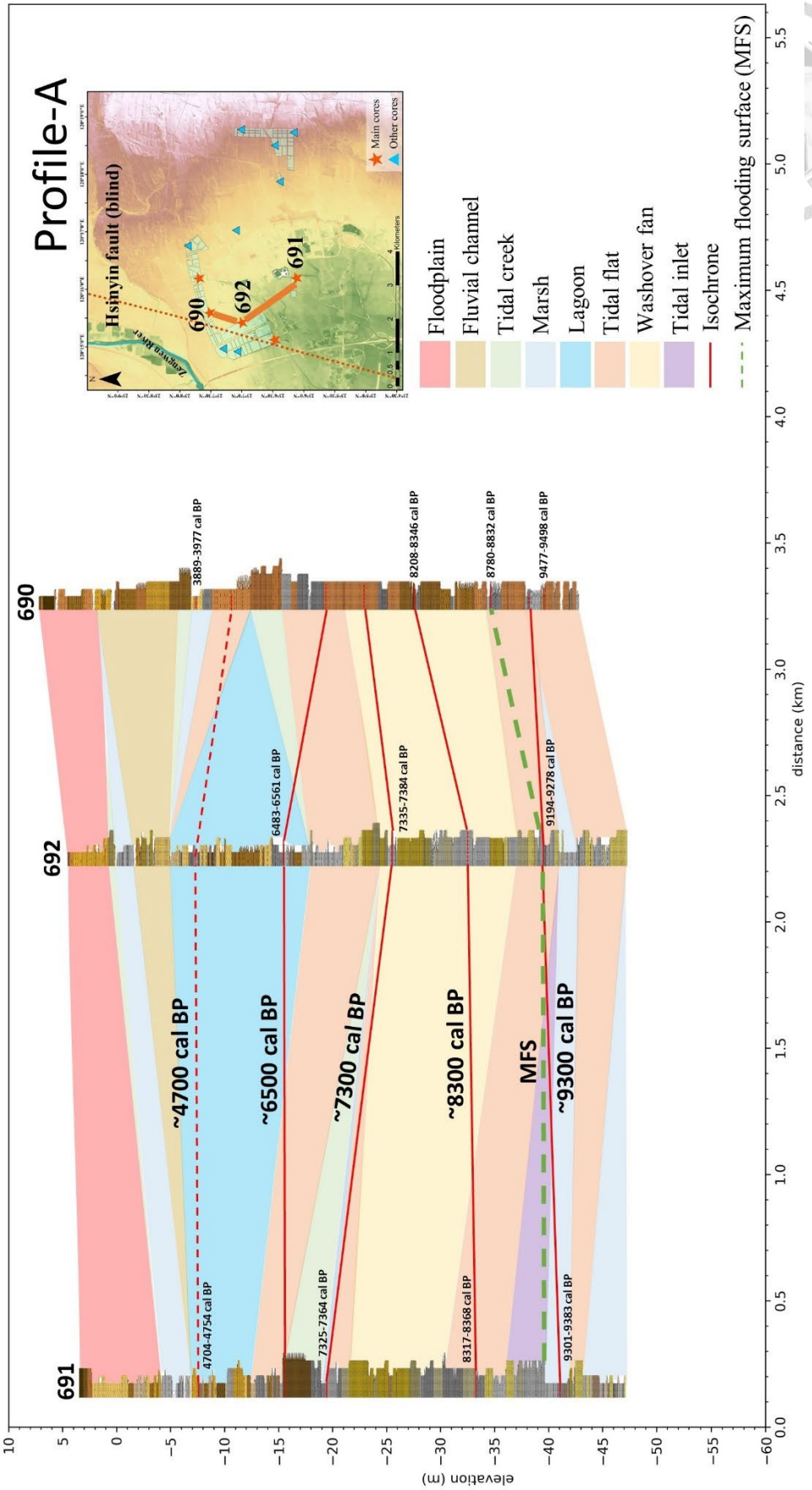

Figure 5.9 Profile A, the order from south to north is 691, 692, 690. The red-colored

doi:10.6342/NTU202302306

blocks represent floodplains, the deep yellow-colored blocks represent fluvial channels, the light green-colored blocks represent tidal creeks, the blue-colored blocks represent marshes, the light blue-colored blocks represent lagoons, the orange-colored blocks represent tidal flats, the yellow-colored blocks represent washover fans, and the purple-colored blocks represent tidal inlets. Additionally, the red lines represent isochrones (with dashed lines indicating uncertainty), and the green dashed lines represent the MFS.

5.3.2 691-699-692-690-700 (Profile B)

Profile B is located on the western side of the drilling area and connected to Core 699, offering the opportunity to observe earlier marine influences compared to Profile A. However, the lack of upper dating points in Cores 699 and 700 limits the consistency of the observed environmental changes. Both cores show the presence of washover fan facies, and the approximate depth of the MFS is inferred to be in the adjacent tidal flats where calcareous fossils are abundant (Figure 5.10).

5.3.3 696-690-700-695 (Profile C)

Profile C is situated on the northern side of the drilling area, similar to Profile B. The approximate depth of the MFS is also inferred to be in the tidal flats adjacent to the washover fan facies, where calcareous fossils are more abundant. Although the lateral extent of the washover fan facies lacks precise dating, a trend of eastward reduction can

doi:10.6342/NTU202302306

be observed (Figure 5.11).

doi:10.6342/NTU202302306

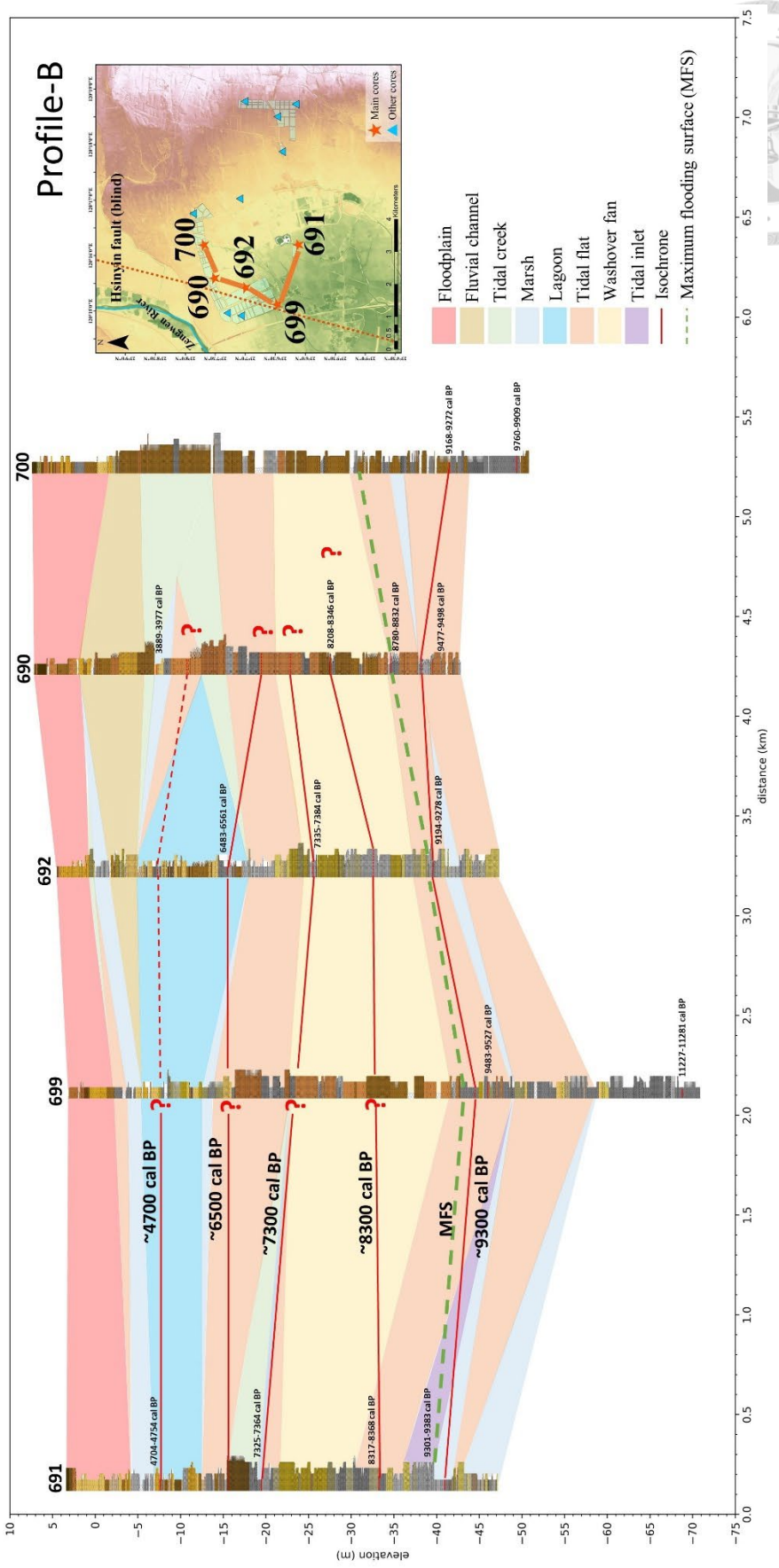

Figure 5.10 Profile B, the order from south to north is 691, 699, 692, 690, 700. The red-

doi:10.6342/NTU202302306

colored blocks represent floodplains, the deep yellow-colored blocks represent fluvial channels, the light green-colored blocks represent tidal creeks, the blue-colored blocks represent marshes, the light blue-colored blocks represent lagoons, the orange-colored blocks represent tidal flats, the yellow-colored blocks represent washover fans, and the purple-colored blocks represent tidal inlets. Additionally, the red lines represent isochrones (with dashed lines indicating uncertainty), and the green dashed lines represent the MFS.

doi:10.6342/NTU202302306

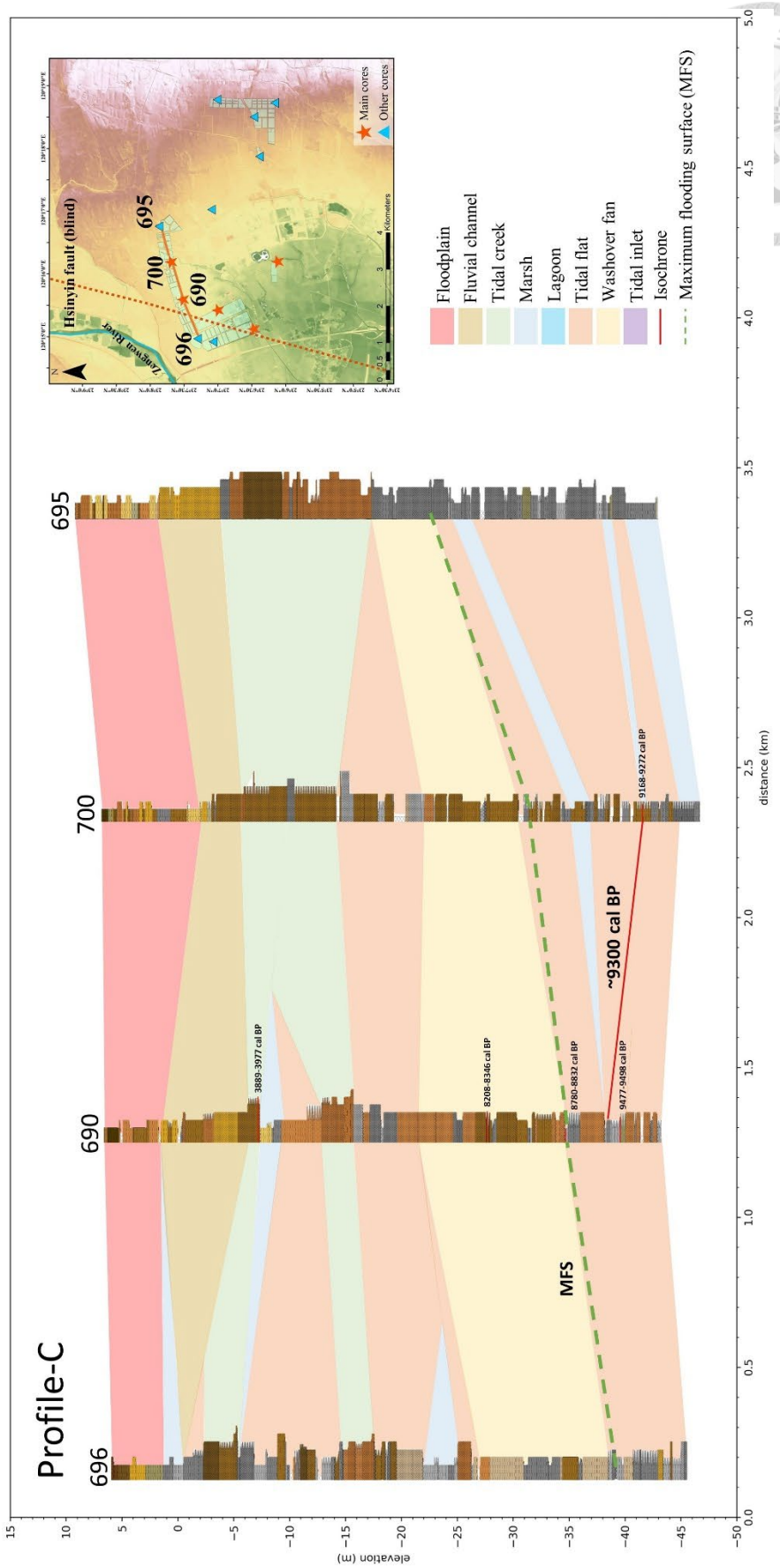

Figure 5.11 Profile C, the order from west to east is 696, 690, 700, 695. The red-colored

doi:10.6342/NTU202302306

blocks represent floodplains, the deep yellow-colored blocks represent fluvial channels, the light green-colored blocks represent tidal creeks, the blue-colored blocks represent marshes, the light blue-colored blocks represent lagoons, the orange-colored blocks represent tidal flats, the yellow-colored blocks represent washover fans, and the purple-colored blocks represent tidal inlets. Additionally, the red lines represent isochrones (with dashed lines indicating uncertainty), and the green dashed lines represent the MFS.

5.3.4 699-692-701-702 (Profile D)

Profile D is located in the central part of the drilling area, extending from Core 699 to the more inland Core 702. By observing the lateral extent of the washover fan facies, a clear trend of eastward reduction can be observed, allowing for an estimation of the marine influence. However, more chronological control is needed for the cores in the eastern part to correspond to the actual age (Figure 5.12).

5.3.5 699-691-697-693-698 (Profile E)

Profile E, extending from Core 699 to the more inland Core 698, is situated on the southern side of the drilling area. The interruption of the washover fan facies can be clearly observed between core 691 and core 697. Notably, core 698 shows the extension of a tidal channel to the west, possibly representing an intermediate zone between a river channel and a tidal channel, contrasting with the washover fan facies observed in core

doi:10.6342/NTU202302306

699 extending inland (Figure 5.13).

doi:10.6342/NTU202302306

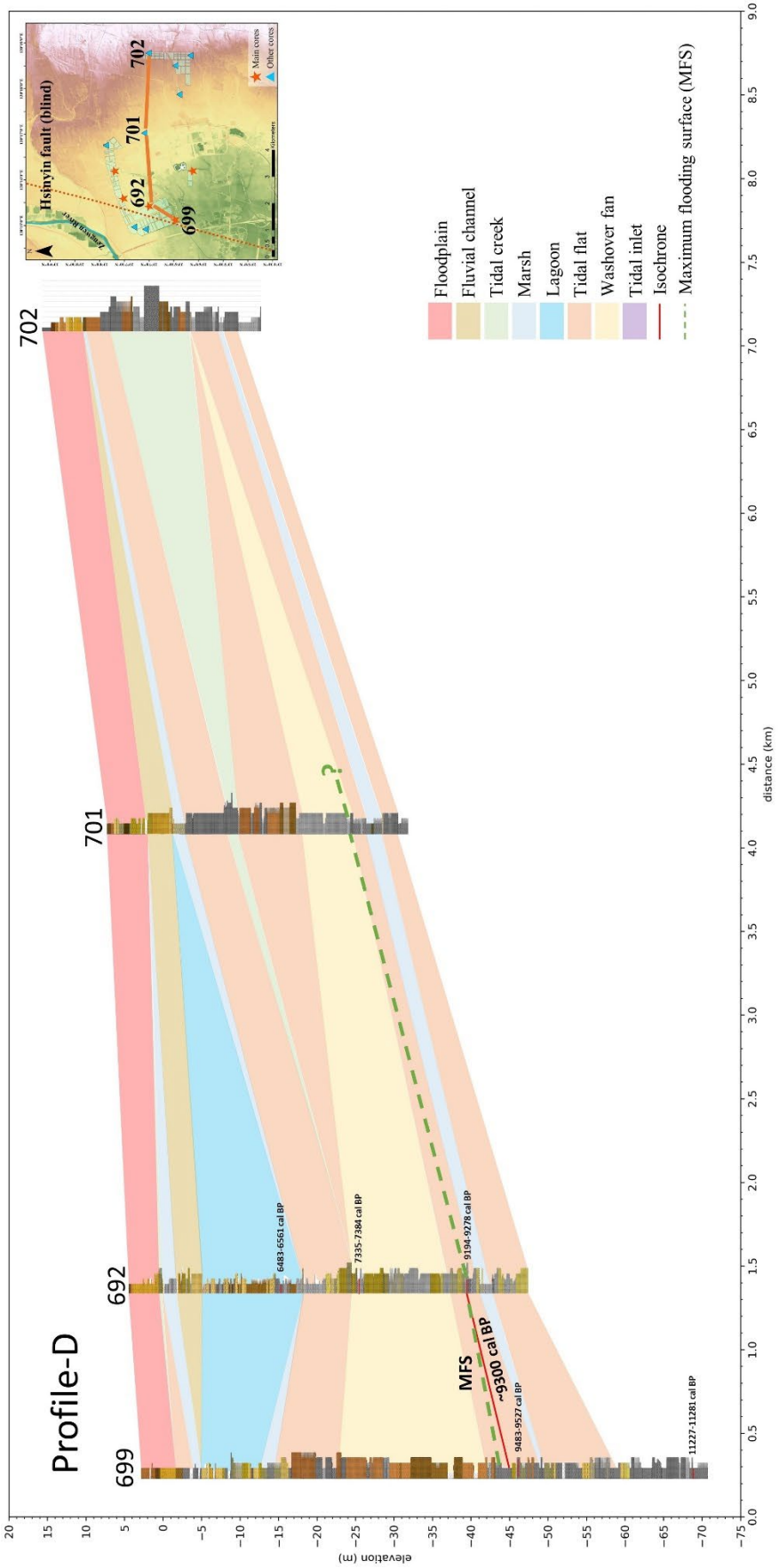

Figure 5.12 Profile D, the order from west to east is 699, 692, 701, 702. The red-colored

doi:10.6342/NTU202302306

blocks represent floodplains, the deep yellow-colored blocks represent fluvial channels, the light green-colored blocks represent tidal creeks, the blue-colored blocks represent marshes, the light blue-colored blocks represent lagoons, the orange-colored blocks represent tidal flats, the yellow-colored blocks represent washover fans, and the purple-colored blocks represent tidal inlets. Additionally, the red lines represent isochrones (with dashed lines indicating uncertainty), and the green dashed lines represent the MFS.

doi:10.6342/NTU202302306

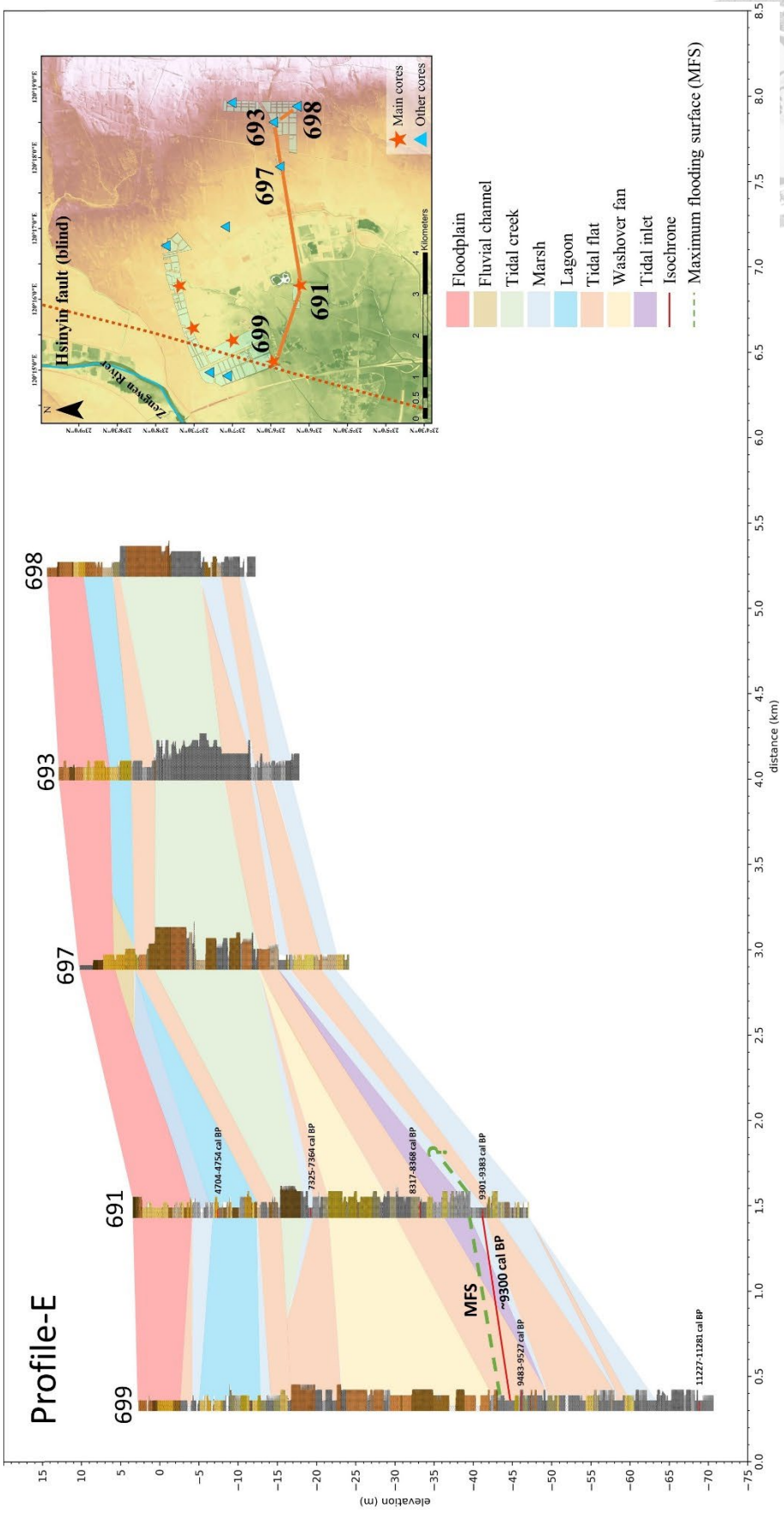

Figure 5.13 Profile E, the order from west to east is 699, 691, 697, 693, 698. The red-

doi:10.6342/NTU202302306

colored blocks represent floodplains, the deep yellow-colored blocks represent fluvial channels, the light green-colored blocks represent tidal creeks, the blue-colored blocks represent marshes, the light blue-colored blocks represent lagoons, the orange-colored blocks represent tidal flats, the yellow-colored blocks represent washover fans, and the purple-colored blocks represent tidal inlets. Additionally, the red lines represent isochrones (with dashed lines indicating uncertainty), and the green dashed lines represent the MFS.

5.4 The environmental changes around midddle-Holocene

The aforementioned environmental changes, except the dating data lacking from 4700 cal BP to the present, can be correlated with the cores in this research. The Holocene transgression can be observed in core 699 and 700, and the MFS is present in all cores. However, due to the lack of dating information after the maximum marine flooding of core 699 and 700, we primarily rely on core 690, 691, and 692 to investigate the post-maximum flooding environmental changes in this region. We also consider the distribution of archaeological sites and the profile comparisons to decipher the sedimentary systems.

The environmental changes are discussed at five time points: 9300, 8300, 7300, 6500, and 4700 cal BP (Figure 5.14). Around 9300 cal BP, most of our study area was predominantly tidal flat, with only core 691 located in a marsh environment. By around

doi:10.6342/NTU202302306

8300 cal BP, a washover fan, likely formed by wave action breaking through or bypassing a barrier island during the maximum flooding period emerged. This suggests that the tidal flats and marshes during this period were located closer to the sea, developing in the shelter of the barrier island. Around 7300 cal BP, a regression of the washover fan was observed, indicating reduced wave action in the area, while core 691 returned to a marsh environment. However, due to a lack of additional data from the intermediate area encompassed by these three cores, the extent of the sedimentary environment can only be roughly estimated. The disappearance of the washover fan around 6500 cal BP resulted from gradual landward processes. Simultaneously, during this period, the appearance of lagoon facies in core 692 and the occurrence of a coarser-grained tidal channel in core 691, accompanied by the tidal flat environment indicated by core 690, suggest that the tidal flats during this time were located closer to the landward side. This also indicates that the coastline gradually expanded westward, leading to the presence of more intertidal environments and a transition to a tidal-dominated setting. Around 4700 cal BP, a more pronounced westward expansion of the coastline can be observed, suggesting the emergence of more terrestrial environments in the eastern areas such as the Nankuanli (南關里) and Nankuanli East (南關里東) sites. It is also possible that suitable coastal environments for human habitation existed in the western areas such as Niuniaokang West (牛尿港西) and Sanpaopi South II (三寶埤南貳). Furthermore, when comparing the

doi:10.6342/NTU202302306

reconstructed sedimentary environment in the vicinity of Tainan Science Park with the work conducted by Huang (2001) in the Zengwen River basin from 9000-3000 cal BP (Figure 5.15), it becomes evident that detailed environmental changes and the relationship with archaeological sites can be discerned.

doi:10.6342/NTU202302306

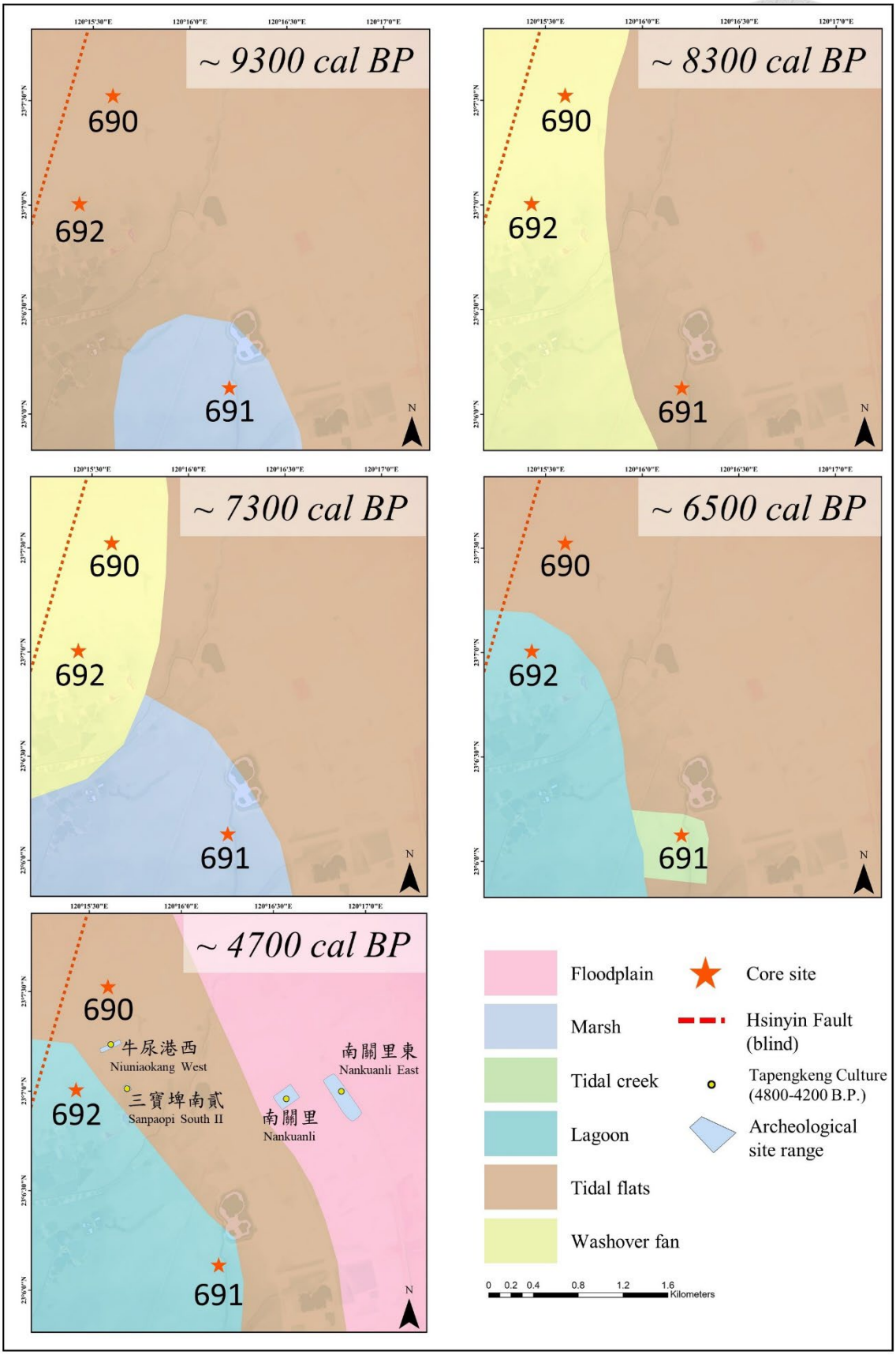

Figure 5.14 The environmental changes during the middle Holocene. The red-colored

doi:10.6342/NTU202302306

blocks represent floodplains, the light green-colored blocks represent tidal creeks, the light blue-colored blocks represent lagoons, the orange-colored blocks represent tidal flats, and the yellow-colored blocks represent washover fans. The core sites are marked as red stars. Hsinyin Fault across the drilling region is adopted from Chen et al. (2004), represented by the red dashed line. Additionally, the Tapengkeng archaeological sites are marked as yellow points, and the blue polygons represent the archaeological site range.

doi:10.6342/NTU202302306

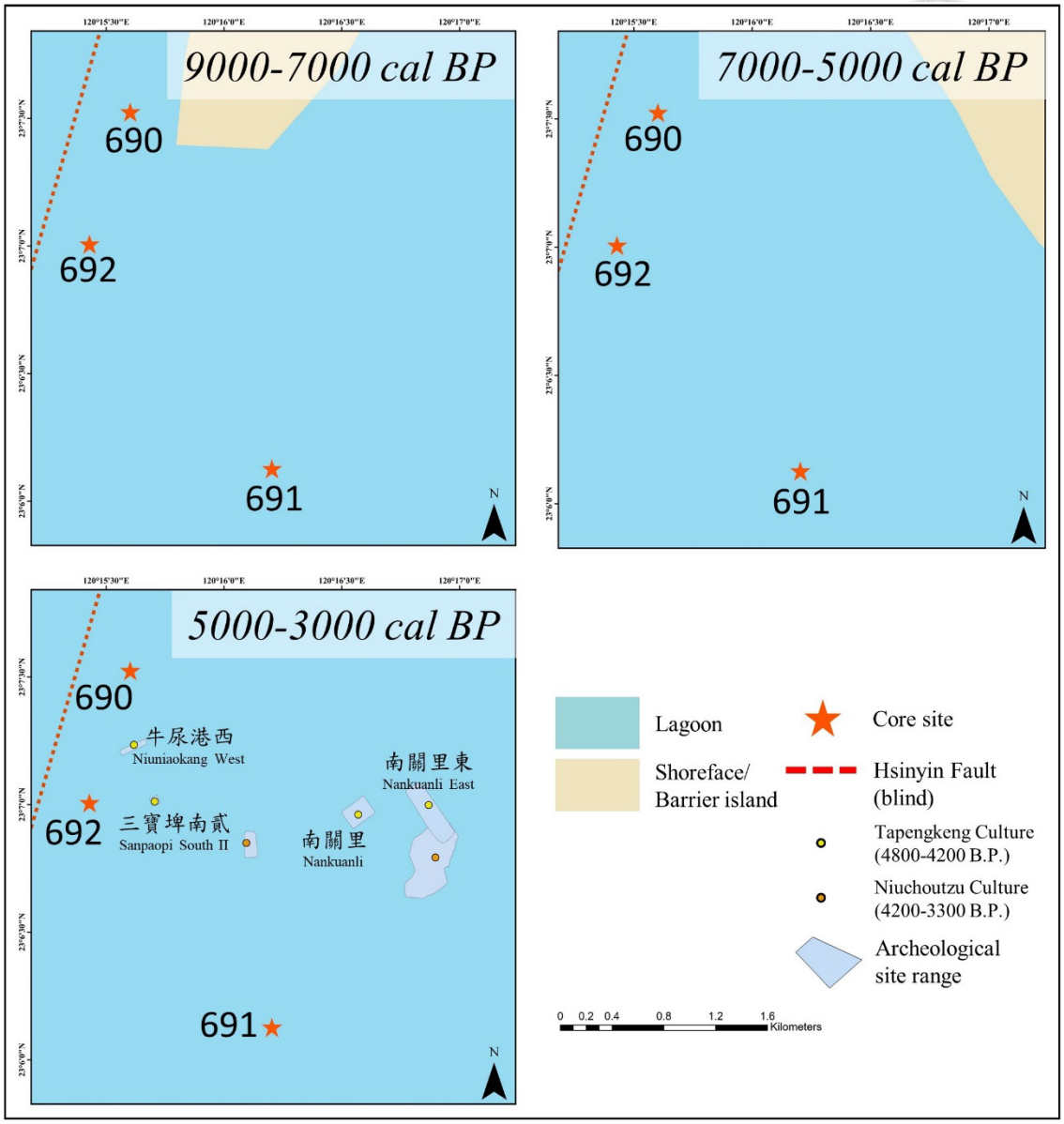

Figure 5.15 The environmental changes during the middle Holocene, adopted from Huang (2001). The light blue-colored blocks represent lagoons, and the dark yellow-colored blocks represent shoreface or barrier islands. The core sites are marked as red stars. Hsinyin Fault across the drilling region is adopted from Chen et al. (2004), represented by the red dashed line. Additionally, the Tapengkeng archaeological sites are marked as yellow points, the Niuchoutzu archaeological sites are marked as orange points, and the blue polygons represent the archaeological site range.

doi:10.6342/NTU202302306

6 Conclusions

By using the multi-proxy method, we can reconstruct paleoenvironments and provide a more comprehensive assessment, establishing sedimentary environments through cross-verification. The Log(Ca/Ti) enables the high-resolution relative calcium carbonate signals in sediment, exhibiting a strong correlation with total inorganic carbon. However, it is challenging to observe particles coarser than fine sand in the Log(Zr/Rb), but variations in particle size below the fine sand range prove to be highly sensitive and significantly correlated with laser particle size analysis and the proportion of coarse grains (>63 μm).

The Tainan Science Park region has already been the subject of numerous studies but lacks high-resolution sediment geochemical data, these geochemical data not only help us to identify different sedimentary facies in high-resolution data but also comparable for future XRF scanning in this area due to its similar trends. Moreover, the relatively stable Log(Ca/Ti) might indicate the presence of a wave-dominated washover fan facies, which can serve as an ongoing reference for assessing chemical signals related to marine incursion in the region.

Besides, collaborating with the elemental carbon analysis and grain size distribution also give us a more comprehensive way to identify different environment in the estuary-barrier island sedimentary system, detailed environmental transformation in Tainan

doi:10.6342/NTU202302306

Science Park during the middle Holocene can be established under this multi-proxy classification, and compared with the Tapengkeng archaeological sites.

However, there are two limitations in our study. One is the density of sampling, we conduct the element carbon and grain size analysis only in an interval average 1 m based on different characteristics of XRF proxy and core description. Although the data of different interval can be corresponded to the result of other experiments, it might be a little hard when we want to utilize the elemental carbon to classify different sedimentary facies, especially for lagoon and marsh that have abundant carbon due to the limited sample.

Another is the lack of dating results, which limits us to only use three sediment cores for comparing the environmental conditions. Despite the sedimentary sequence can be identified to postulate the general environmental transformation from 9300-4700 cal BP in other long cores, it still needs more dating results in this interval to acquire the time constraint. Moreover, the dating materials from cores prior to approximately 4700 cal BP are scarce due to the relative terrestrial realm. It also makes us hard to compare our multi-proxy result with the abundant archaeological sites early than Tapengkeng Culture. Hopefully, future studies will provide more age-related information to enhance our understanding of the region's paleoenvironmental changes.

doi:10.6342/NTU202302306

References

Aitchison, J. (1982). The Statistical Analysis of Compositional Data. In *Source: Jo urnal of the Royal Statistical Society. Series B (Methodological)* (Vol. 44, Issu e 2).

Aitchison, J., & Egozcue, J. J. (2005). Compositional data analysis: Where are we and where should we be heading? *Mathematical Geology*, *37*(7), 829–850. htt ps://doi.org/10.1007/s11004-005-7383-7

Bloemsma, M. R., Zabel, M., Stuut, J. B. W., Tjallingii, R., Collins, J. A., & Welt je, G. J. (2012). Modelling the joint variability of grain size and chemical co mposition in sediments. *Sedimentary Geology*, *280*, 135–148. https://doi.org/10. 1016/j.sedgeo.2012.04.009

Boothroyd, J. C., Friedrich, N. E., & McGinn, S. R. (1985). Geology of microtidal coastal lagoons: Rhode Island. *Marine Geology*, *63*(1–4), 35–76. https://doi.or g/10.1016/0025-3227(85)90079-9

Bown, T. M., & Kraus, M. J. (1987). Integration of channel and floodplain suites. I. Developmental sequence and lateral relations of alluvial paleosols. *Journal of Sedimentary Petrology*, *57*(4), 587–601.

Boyle, J. F. (2001). Inorganic Geochemical Methods in Palaeolimnology. In W. M. Last & J. P. Smol (Eds.), *Tracking Environmental Change Using Lake S*

doi:10.6342/NTU202302306

ediments (Vol. 2, pp. 83–141). Kluwer Academic Publishers, Dordrecht. https://doi.org/10.1007/0-306-47670-3_5

Chawchai, S., Chabangborn, A., Kylander, M., Löwemark, L., Mörth, C. M., Blaauw, M., Klubseang, W., Reimer, P. J., Fritz, S. C., & Wohlfarth, B. (2013). Lake Kumphawapi – an archive of Holocene palaeoenvironmental and palaeoclimatic changes in northeast Thailand. *Quaternary Science Reviews*, *68*, 59–75. https://doi.org/10.1016/J.QUASCIREV.2013.01.030

Chen, J., Yang, C., Liu, L., Ji, J., Balsam, W., Sun, Y., & Lu, H. (2006). Zr/Rb ratio in the Chinese loess sequences and its implication for changes in the East Asian winter monsoon strength. *Geochimica et Cosmochimica Acta*, *70*(6), 1471–1482. https://doi.org/10.1016/J.GCA.2005.11.029

Chen, Y.-G., & Liu, T.-K. (1996). Sea Level Changes in the Last Several Thousand Years, Penghu Islands, Taiwan Strait. In *QUATERNARY RESEARCH* (Vol. 45).

CHUN, S. S., & CHOUGH, S. K. (1995). The Cretaceous Uhangri Formation, SW Korea: lacustrine margin facies. *Sedimentology*, *42*(2), 293–322. https://doi.org/10.1111/J.1365-3091.1995.TB02104.X

Church, J. A. , J.M. Gregory, P. Huybrechts, M. Kuhn, K. Lambeck, M.T. Nhuan, D. Qin, & P.L. Woodworth. (2001). Changes in Sea Level. In Houghton et al.

doi:10.6342/NTU202302306

(Ed.), *Climate Change 2001: The Scientific Basis* (pp. 639–693).

Clifton, H. E., Hunter, R. E., & Phillips, R. L. (1971). Depositional structures and processes in the non-barred high-energy nearshore. *Journal of Sedimentary Re search*, *41*(3), 651–670. https://doi.org/10.1306/74D7231A-2B21-11D7-8648000 102C1865D

Cohen, A. S. (2003). Paleolimnology: The History and Evolution of Lake Systems. *Paleolimnology*. https://doi.org/10.1093/OSO/9780195133530.001.0001

Croudace, I. W., Löwemark, L., Tjallingii, R., & Zolitschka, B. (2019). Current per spectives on the capabilities of high resolution XRF core scanners. *Quaternar y International*, *514*, 5–15. https://doi.org/10.1016/j.quaint.2019.04.002

Croudace, I. W., Rindby, A., & Rothwell, R. G. (2006). ITRAX: Description and e valuation of a new multi-function X-ray core scanner. *Geological Society Spec ial Publication*, *267*, 51–63. https://doi.org/10.1144/GSL.SP.2006.267.01.04

Dalrymple, R. W., Zaitlin, B. A., & Boyd, R. (1992). Estuarine facies models; con ceptual basis and stratigraphic implications. *Journal of Sedimentary Research*, *62*(6), 1130–1146. https://doi.org/10.1306/D4267A69-2B26-11D7-8648000102C 1865D

Davies, S. J., Lamb, H. F., & Roberts, S. J. (2015). *Micro-XRF Core Scanning in Palaeolimnology: Recent Developments*. 189–226. https://doi.org/10.1007/978-9

doi:10.6342/NTU202302306

4-017-9849-5_7

De Swart, H. E., & Zimmerman, J. T. F. (2008). Morphodynamics of Tidal Inlet S ystems. *Https://Doi.Org/10.1146/Annurev.Fluid.010908.165159*, *41*, 203–229. ht tps://doi.org/10.1146/ANNUREV.FLUID.010908.165159

De Vries, J. L. , & Vrebos, B. A. R. (2002). Quantification of infinitely thick spec imens by XRF analysis. In R. E. , M. A. A. van Grieken (Ed.), *Handbook of X-Ray Spectrometry* (Second, pp. 341–405). Marcel Dekker.

Dott, R. H., & Bourgeois, J. (1982). Hummocky stratification: significance of its v ariable bedding sequences. *Geological Society of America Bulletin*, *93*(8), 663 –680. https://doi.org/10.1130/0016-7606(1982)93<663:HSSOIV>2.0.CO;2

Dypvik, H., & Harris, N. B. (2001). Geochemical facies analysis of fine-grained si liciclastics using Th/U, Zr/Rb and (Zr+Rb)/Sr ratios. *Chemical Geology*, *181*(1 –4), 131–146. https://doi.org/10.1016/S0009-2541(01)00278-9

Erban, L. E., Gorelick, S. M., & Zebker, H. A. (2014). Groundwater extraction, la nd subsidence, and sea-level rise in the Mekong Delta, Vietnam. *Environment al Research Letters*, *9*(8). https://doi.org/10.1088/1748-9326/9/8/084010

Fleming, E., Payne, J. L., Sweet, W. V., Craghan, M., Haines, J., Hart, J. A. F., St iller, H., & Sutton-Grier, A. (2018). *Chapter 8 : Coastal Effects. Impacts, Risk s, and Adaptation in the United States: The Fourth National Climate Assessm*

doi:10.6342/NTU202302306

ent, Volume II. https://doi.org/10.7930/NCA4.2018.CH8

Franzini, M., Leoni, L., & Saitta, M. (1972). A simple method to evaluate the m atrix effects in X-Ray fluorescence analysis. *X-Ray Spectrometry*, *1*(4), 151–154. https://doi.org/10.1002/XRS.1300010406

Frey, R. W., & Basan, P. B. (1985). Coastal Salt Marshes. *Coastal Sedimentary En vironments*, 225–301. https://doi.org/10.1007/978-1-4612-5078-4_4

Gregory, B. R. B., Patterson, R. T., Reinhardt, E. G., Galloway, J. M., & Roe, H. M. (2019). An evaluation of methodologies for calibrating Itrax X-ray fluoresc ence counts with ICP-MS concentration data for discrete sediment samples. *C hemical Geology*, *521*, 12–27. https://doi.org/10.1016/j.chemgeo.2019.05.008

Guyard, H., Chapron, E., St-Onge, G., Anselmetti, F. S., Arnaud, F., Magand, O., Francus, P., & Mélières, M. A. (2007). High-altitude varve records of abrupt e nvironmental changes and mining activity over the last 4000 years in the Wes tern French Alps (Lake Bramant, Grandes Rousses Massif). *Quaternary Scienc e Reviews*, *26*(19–21), 2644–2660. https://doi.org/10.1016/J.QUASCIREV.2007.07.007

Harms, J. C., Southard, J. B., Southard, J. B., & Walker, R. G. (1982). Structures and Sequences in Clastic Rocks. *Structure and Sequence in Clastic Rocks*. htt ps://doi.org/10.2110/SCN.82.09

doi:10.6342/NTU202302306

Hennekam, R., & De Rick, G. (2012). X-ray fluorescence core scanning of wet m arine sediments: methods to improve quality and reproducibility of high-resolu tion paleoenvironmental records. *Limnology and Oceanography: Methods*, *10* (12), 991–1003. https://doi.org/10.4319/LOM.2012.10.991

Hennessy, J. T., & Zarillo, G. A. (1987). The interrelation and distinction between flood-tidal delta and washover deposits in a transgressive barrier island. *Marin e Geology*, *78*(1–2), 35–56. https://doi.org/10.1016/0025-3227(87)90067-3

Ingram, W. C., Meyers, S. R., Brunner, C. A., & Martens, C. S. (2010). Late Pleis tocene–Holocene sedimentation surrounding an active seafloor gas-hydrate and cold-seep field on the Northern Gulf of Mexico Slope. *Marine Geology*, *278* (1–4), 43–53. https://doi.org/10.1016/J.MARGEO.2010.09.002

Itambi, A. C., von Dobeneck, T., & Adegbie, A. T. (2010). Millennial-scale precipi tation changes over Central Africa during the late Quaternary and Holocene: e vidence in sediments from the Gulf of Guinea. *Journal of Quaternary Science*, *25*(3), 267–279. https://doi.org/10.1002/JQS.1306

Jenkins, R., & De Vries, J. L. (1970). Practical X-Ray Spectrometry. *Practical X-R ay Spectrometry*. https://doi.org/10.1007/978-1-349-00055-5

Kido, Y., Koshikawa, T., & Tada, R. (2006). Rapid and quantitative major element analysis method for wet fine-grained sediments using an XRF microscanner.

doi:10.6342/NTU202302306

Marine Geology, *229*(3–4), 209–225. https://doi.org/10.1016/j.margeo.2006.03.002

Klein, G. de V. (1971). *A Sedimentary Model for Determining Paleotidal Range*. *82*, 2585–2592.

Kraus, M. J. (1987). Integration of channel and floodplain suites, II. Vertical relations of alluvial paleosols. *Journal of Sedimentary Petrology*, *57*(4), 602–612. https://doi.org/10.1306/212F8BB6-2B24-11D7-8648000102C1865D

Kraus, M. J., & Aslan, A. (1993). Eocene Hydromorphic Paleosols: Significance for Interpreting Ancient Floodplain Processes. *Journal of Sedimentary Research*, *63*(3), 453–463. https://doi.org/10.1306/D4267B22-2B26-11D7-8648000102C1865D

Kylander, M. E., Ampel, L., Wohlfarth, B., & Veres, D. (2011). High-resolution X-ray fluorescence core scanning analysis of Les Echets (France) sedimentary sequence: New insights from chemical proxies. *Journal of Quaternary Science*, *26*(1), 109–117. https://doi.org/10.1002/JQS.1438

Longhitano, S. G., Mellere, D., Steel, R. J., & Ainsworth, R. B. (2012). Tidal depositional systems in the rock record: A review and new insights. *Sedimentary Geology*, *279*, 2–22. https://doi.org/10.1016/J.SEDGEO.2012.03.024

Longman, J., Veres, D., & Wennrich, V. (2019). Utilisation of XRF core scanning

doi:10.6342/NTU202302306

on peat and other highly organic sediments. *Quaternary International*, *514*, 85–96. https://doi.org/10.1016/j.quaint.2018.10.015

Löwemark, L., Bloemsma, M., Croudace, I., Daly, J. S., Edwards, R. J., Francus, P., Galloway, J. M., Gregory, B. R. B., Steven Huang, J. J., Jones, A. F., Kylander, M., Luo, Y., Maclachlan, S., Ohlendorf, C., Patterson, R. T., Pearce, C., Profe, J., Reinhardt, E. G., Stranne, C., … Turner, J. N. (2019). Practical guidelines and recent advances in the Itrax XRF core-scanning procedure. *Quaternary International*, *514*, 16–29. https://doi.org/10.1016/j.quaint.2018.10.044

Löwemark, L., Chen, H. F., Yang, T. N., Kylander, M., Yu, E. F., Hsu, Y. W., Lee, T. Q., Song, S. R., & Jarvis, S. (2011). Normalizing XRF-scanner data: A cautionary note on the interpretation of high-resolution records from organic-rich lakes. *Journal of Asian Earth Sciences*, *40*(6), 1250–1256. https://doi.org/10.1016/j.jseaes.2010.06.002

Mark, S. Z., Abbott, M. B., Rodbell, D. T., & Moy, C. M. (2022). XRF analysis of Laguna Pallcacocha sediments yields new insights into Holocene El Niño development. *Earth and Planetary Science Letters*, *593*. https://doi.org/10.1016/j.epsl.2022.117657

Meyers, P. A. (1997). Organic geochemical proxies of paleoceanographic, paleolimnologic, and paleoclimatic processes. *Organic Geochemistry*, *27*(5–6), 213–250.

doi:10.6342/NTU202302306

https://doi.org/10.1016/S0146-6380(97)00049-1

Miall, A. D. (1977). A review of the braided-river depositional environment. *Earth -Science Reviews*, *13*(1), 1–62. https://doi.org/10.1016/0012-8252(77)90055-1

Miall, A. D. (1996). *The geology of fluvial deposits. Sedimentary facies, basin ana lysis, and petroleum geology*. 582.

Neumann, J. E., Emanuel, K., Ravela, S., Ludwig, L., Kirshen, P., Bosma, K., & Martinich, J. (2015). Joint effects of storm surge and sea-level rise on US Co asts: new economic estimates of impacts, adaptation, and benefits of mitigatio n policy. *Climatic Change*, *129*(1–2), 337–349. https://doi.org/10.1007/S10584-014-1304-Z/FIGURES/6

Olsen, T. R., Mellere, D., & Olsen, T. (1999). Facies architecture and geometry of landward-stepping shoreface tongues: the Upper Cretaceous Cliff House Sands tone (Mancos Canyon, south-west Colorado). *Sedimentology*, *46*(4), 603–625.

Ramsey, C. B. (2009). Bayesian Analysis of Radiocarbon Dates. *Radiocarbon*, *51* (1), 337–360. https://doi.org/10.1017/S0033822200033865

Reimer, P. J., Austin, W. E. N., Bard, E., Bayliss, A., Blackwell, P. G., Bronk Ra msey, C., Butzin, M., Cheng, H., Edwards, R. L., Friedrich, M., Grootes, P. M., Guilderson, T. P., Hajdas, I., Heaton, T. J., Hogg, A. G., Hughen, K. A., Kromer, B., Manning, S. W., Muscheler, R., … Talamo, S. (2020). The IntCal

doi:10.6342/NTU202302306

20 Northern Hemisphere Radiocarbon Age Calibration Curve (0–55 cal kBP). *Radiocarbon*, *62*(4), 725–757. https://doi.org/10.1017/RDC.2020.41

Reineck, H.-E., & Singh, I. B. (1980). Depositional Sedimentary Environments. *De positional Sedimentary Environments*. https://doi.org/10.1007/978-3-642-81498-3

Reineck, H.-E., & Wunderlich, F. (1968). CLASSIFICATION AND ORIGIN OF F LASER AND LENTICULAR BEDDING. *Sedimentology*, *11*(1–2), 99–104. htt ps://doi.org/10.1111/J.1365-3091.1968.TB00843.X

Reinson, G. E. (1992). Transgressive Barrier Island and Estuarine Systems. In R. G. Walker & N. P. James (Eds.), *Facies Models: Response to Sea Level Chan ge* (pp. 179–194).

Richter, T. O., Van Der Gaast, S., Koster, B., Vaars, A., Gieles, R., De Stigter, H. C., De Haas, H., & Van Weering, C. E. (2006). The Avaatech XRF Core Sca nner: technical description and applications to NE Atlantic sediments. In Roth well RG (Ed.), *New techniques in sediment core analysis* (Vol. 267, pp. 39–5 0). Geological Society, London, Special Publications. https://doi.org/10.1144/ G SL.SP.2006.267.01.03

Rohling, E. J., Fenton, M., Jorissen, F. J., Bertrand, P., Ganssen, G., & Caulet, J. P. (1998). Magnitudes of sea-level lowstands of the past 500,000 years. *Natur*

doi:10.6342/NTU202302306

e 1998 394:6689, *394*(6689), 162–165. https://doi.org/10.1038/28134

Rothwell, R. G., Croudace, I. W., Rothwell, R. G., & Croudace, I. W. (2015a). *Micro-XRF Studies of Sediment Cores: A Perspective on Capability and Application in the Environmental Sciences*. *17*, 1–21. https://doi.org/10.1007/978-94-017-9849-5_1

Rothwell, R. G., Croudace, I. W., Rothwell, R. G., & Croudace, I. W. (2015b). *Twenty Years of XRF Core Scanning Marine Sediments: What Do Geochemical Proxies Tell Us?* 25–102. https://doi.org/10.1007/978-94-017-9849-5_2

Rothwell, R. G., Hoogakker, B., Thomson, J., Croudace, I. W., & Frenz, M. (2006). Turbidite emplacement on the southern Balearic Abyssal Plain (western Mediterranean Sea) during Marine Isotope Stages 1–3: an application of ITRAX XRF scanning of sediment cores to lithostratigraphic analysis. *Geological Society Special Publication*, *267*, 79–98. https://doi.org/10.1144/GSL.SP.2006.267.01.06

Schwartz, R. K. (1982). Bedform and stratification characteristics of some modern small-scale washover sand bodies. *Sedimentology*, *29*(6), 835–849. https://doi.org/10.1111/J.1365-3091.1982.TB00087.X

Shala, S., Helmens, K. F., Jansson, K. N., Kylander, M. E., Risberg, J., & Löwemark, L. (2014). Palaeoenvironmental record of glacial lake evolution during th

doi:10.6342/NTU202302306

e early Holocene at Sokli, NE Finland. *Boreas*, *43*(2), 362–376. https://doi.org/10.1111/BOR.12043

Stuiver, M., & Reimer, P. J. (1993). CALIB rev. 8. In *Radiocarbon* (Vol. 35, pp. 215–230).

Sun, S.-C. (1964). Photogeologic Study Of The Tainan-Kaohsiung Coastal Plain Area, Taiwan. *Petroleum Geology of Taiwan*, *3*, 39–51.

Sun, S. C. (1970). Photogeologic study of the Tainan-Hsinying coastal plain, Taiwan. *Petroleum Geology of Taiwan*, *7*, 133–144.

Swift, D. J. P., Figueiredo, A. G., Freeland, G. L., & Oertel, G. F. (1983). Hummocky cross-stratification and megaripples; a geological double standard? *Journal of Sedimentary Research*, *53*(4), 1295–1317. https://doi.org/10.1306/212F8369-2B24-11D7-8648000102C1865D

Swift, D. J. P., Phillips, S., & Thorne, J. A. (2009). Sedimentation on Continental Margins, IV: Lithofacies and Depositional Systems. *Shelf Sand and Sandstone Bodies*, 89–152. https://doi.org/10.1002/9781444303933.CH4

Thomas, R. G., Smith, D. G., Wood, J. M., Visser, J., Calverley-Range, E. A., & Koster, E. H. (1987). Inclined heterolithic stratification—Terminology, description, interpretation and significance. *Sedimentary Geology*, *53*(1–2), 123–179. https://doi.org/10.1016/S0037-0738(87)80006-4

doi:10.6342/NTU202302306

Thorbjarnarson, K. W., Nittrouer, C. A., DeMaster, D. J., & McKinney, R. B. (1985). Sediment accumulation in a back-barrier lagoon, Great Sound, New Jersey. *Journal of Sedimentary Research*, *55*(6), 856–863. https://doi.org/10.1306/212F881E-2B24-11D7-8648000102C1865D

Turner, J. N., Jones, A. F., Brewer, P. A., Macklin, M. G., Rassner, S. M., Turner, J. N., Jones, · A F, Jones, A. F., Brewer, P. A., Macklin, · M G, Rassner, · S M, Macklin, M. G., & Rassner, S. M. (2015). *Micro-XRF Applications in Fluvial Sedimentary Environments of Britain and Ireland: Progress and Prospects*. *17*, 227–265. https://doi.org/10.1007/978-94-017-9849-5_8

Walker, R. G. (1984). Facies model: Geoscience Canada, Reprint Series, 1, Anisworth Press, 2nd edition, 317pp

Wang, M. J., Zheng, H. B., Xie, X., Fan, D. Du, Yang, S. Y., Zhao, Q. H., & Wang, K. (2011). A 600-year flood history in the Yangtze River drainage: Comparison between a subaqueous delta and historical records. *Chinese Science Bulletin*, *56*(2), 188–195. https://doi.org/10.1007/S11434-010-4212-2/METRICS

Weimer, R. J., Howard, J. D., & Lindsay, D. R. (1982). Tidal Flats and Associated Tidal Channels. *Sandstone Depositional Environments*. https://doi.org/10.1306/M31424C9

Weltje, G. J., Bloemsma, M. R., Tjallingii, R., Heslop, D., Röhl, U., & Croudace,

doi:10.6342/NTU202302306

I. W. (2015). *Prediction of Geochemical Composition from XRF Core Scanner Data: A New Multivariate Approach Including Automatic Selection of Calibration Samples and Quantification of Uncertainties*. 507–534. https://doi.org/10.1007/978-94-017-9849-5_21

Weltje, G. J., & Tjallingii, R. (2008). Calibration of XRF core scanners for quantitative geochemical logging of sediment cores: Theory and application. *Earth and Planetary Science Letters*, *274*(3–4), 423–438. https://doi.org/10.1016/j.epsl.2008.07.054

Wentworth, C. K. (1922). A Scale of Grade and Class Terms for Clastic Sediments. *The Journal of Geology*, *30*(5), 377–392. https://doi.org/10.1086/622910

Wolters, S., Zeiler, M., & Bungenstock, F. (2010). Early Holocene environmental history of sunken landscapes: Pollen, plant macrofossil and geochemical analyses from the Borkum Riffgrund, southern North Sea. *International Journal of Earth Sciences*, *99*(8), 1707–1719. https://doi.org/10.1007/S00531-009-0477-6/TABLES/4

Wu, L., Wilson, D. J., Wang, R., Yin, X., Chen, Z., Xiao, W., & Huang, M. (2020). Evaluating Zr/Rb Ratio From XRF Scanning as an Indicator of Grain-Size Variations of Glaciomarine Sediments in the Southern Ocean. *Geochemistry, Geophysics, Geosystems*, *21*(11), e2020GC009350. https://doi.org/10.1029/2020G

doi:10.6342/NTU202302306

C009350

Yu, S. B., Chen, H. Y., & Kuo, L. C. (1997) Velocity field of GPS stations in the Taiwan area. Tectonophysics, 274(1 3), 41 59. doi: 10.1016/s0040 1951(96)00 297 1

Zhang, X., Zhang, H., Chang, F., Ashraf, U., Peng, W., Wu, H., Liu, Q., Liu, F., Zhang, Y., & Duan, L. (2020). Application of Corrected Methods for High-Resolution XRF Core Scanning Elements in Lake Sediments. *Applied Sciences 2020, Vol. 10, Page 8012*, *10*(22), 8012. https://doi.org/10.3390/APP10228012

Reference (In Chinese)

Chang, J.-C. (張瑞津)、Shih, T.-T. (石再添)、Chen, H. (陳翰霖)(1996) A Study On Geomorphological Change Of Tainan Coastal Plain, Southwestern Taiwan：臺灣師範大學地理研究報告，第26期，第19–56頁。

Lin, C.-C. (林朝棨)(1961) Shell Mounds In Southwest Taiwan And Their Geohistorical Significance：國立台灣大學考古人類學刊，第15~16期，第49–94頁。

Lin, C.-C. (林朝棨)(1966) An Outline Of Taiwan's Quaternary Geohistory With A Special Discussion Of The Relation Between Natural History And Cultural History In Taiwan：國立臺灣大學人類學刊，第28期，第7–44頁。

Yang, C.-C. (楊志成)(2007) Seismogenic Structure of the Chiayi-Tainan Area and the Long-term Slip Rates of Frontal Thrusts in Southwestern Taiwan：國立台

doi:10.6342/NTU202302306

灣大學地質科學研究所博士論文，共116頁。

Yang, Y.-J. (楊詠然)(2016) Environment Evolution of the Western Coastal Plain in Taiwan Since the Last Glacial Maximum Period：國立台灣大學地質科學研究所碩士論文，共173頁。

Wang, C.-K. (王超國)(2009) Analysis of Geomorphologic Change and Evolution f or Tai-Jiang Inner Sea of Taiwan by Time Series Maps：國立台灣大學地質科學研究所碩士論文，共120頁。

Shih, T.-T. (石再添)(1979) Landforms and Their Evolution of the Chianan Liman Coast in Southwestern Taiwan：國立臺灣師範大學地理學研究報告，第五期，第11–48頁。

Kaim Ang (翁佳音)、Liu, Y.-C (劉益昌)、黃文博、許清保(2010) 台江國家公園及周緣地區人文歷史調查及保存之先期規劃成果報告。

Tsang, Cheng-hwa (臧振華)、Li, Kuang-Ti (李匡悌)、Chu, Cheng-Yi(朱正宜)(2004) 臺南科學工業園區道爺遺址未劃入保存區部分搶救考古計劃期末報告。

Tsang, Cheng-hwa (臧振華)、Li, Kuang-Ti (李匡悌)、李德仁、Chu, Cheng-Yi (朱正宜)(2007) 南部科學工業園區考古遺址搶救監測後續計畫期末報告。

Chen, Y.-G. (陳于高)(1993) Sea-level change and neotectonics in southern part of Taiwan region since late pleistocene：國立台灣大學地質科學研究所博士論文，共159頁。

doi:10.6342/NTU202302306

Chen, W.-S. (陳文山)、Sung, S.-H. (宋時驊)、Wu, L.-C. (吳樂群)、Hsu, H.-D. (徐澔德)、Yang, H.-C. (楊小青)(2004). Shoreline changes of Taiwan since the Last Glacial Maximum：考古人類學刊，第40–55頁。

Chen, W.-S. (陳文山)、Yang, C.-C. (楊志成)、Yang, H.-C (楊小青)(2009). How to reconstruct the late quaternary subsurfae stratigraphy of the Taiwan coastal plain：經濟部中央地質調查所特刊，第22期，第101–114頁。

Chen, W.-S. (陳文山), Yang, C.-C. (楊志成), Yang, H.-C. (楊小青), Wu, L.-C. (吳樂群), Lin, C.-W. (林啟文), Chang, H. C. (張徽正), Shih, R. (石瑞銓), Lin, W.-H. (林偉雄), Lee, Y.-H. (李元希), Shih, T.-S. (石同生), & Lu, S. (盧詩丁)(2004). Tectono-geomorphologic studies in the Chiayi-Tainan region in southwestern Taiwan and its implications for active structure：經濟部中央地質調查所彙刊，第53–77頁.

Huang, Y.-T. (黃郁婷)(2001). Upper Quaternary Sedimentary Environments and Sequence Stratigraphy of the Tsengwen-hsi River Basin , Chianan Plain：A Preliminary Study：國立台灣大學地質學研究所碩士論文，共158頁。

doi:10.6342/NTU202302306

Appendix

doi:10.6342/NTU202302306

Appendix 1 Probability of the calibrated age

Core	Depth (m)	Calibrated age (68.3 %, 1 σ)	Calibrated age (95.4 %, 2 σ)
690	13.8	3889-3936 cal BP (54.9 %) 3938-3977 cal BP (45.1 %)	3840-3988 cal BP (94.2 %) 4044-4071 cal BP (5.8 %)
	34.5	8208-8262 cal BP (45.5 %) 8301-8346 cal BP (54.5 %)	8193-8272 cal BP (48.8 %) 8277-8365 cal BP (51.2 %)
	41.4	8780-8832 cal BP (39.1 %) 8861-8885 cal BP (17.4 %) 8892-8918 cal BP (20.2 %) 8944-8956 cal BP (5.8 %) 8975-8997 cal BP (17.5 %)	8725-8740 cal BP (1.7 %) 8766-9007 cal BP (98.3 %)
	46.2	9477-9498 cal BP (48.4 %) 9503-9527 cal BP (51.6 %)	9449-9534 cal BP (100 %)
691	11.1	4653-4668 cal BP (15.7 %) 4704-4754 cal BP (56.6 %) 4811-4834 cal BP (27.7 %)	4620-4685 cal BP (23.2 %) 4687-4762 cal BP (48.5 %) 4792-4843 cal BP (28.3 %)
	22.9	7325-7364 cal BP (51 %) 7377-7403 cal BP (34.2 %) 7410-7421 cal BP (14.8 %)	7281-7295 cal BP (3 %) 7307-7425 cal BP (97 %)
	36.7	8216-8252 cal BP (37 %) 8317-8368 cal BP (63 %)	8198-8267 cal BP (38.4 %) 8282-8367 cal BP (61.6 %)
	44.6	9301-9383 cal BP (75.9 %) 9397-9423 cal BP (24.1 %)	9151-9168 cal BP (2.2 %) 9271-9458 cal BP (97.8 %)
692	19.8	6453-6469 cal BP (10.5 %) 6483-6561 cal BP (84.3 %) 6591-6598 cal BP (5.3 %)	6413-6417 cal BP (0.7 %) 6442-6629 cal BP (99.3 %)
	29.8	7335-7384 cal BP (86.7 %) 7419-7426 cal BP (13.3 %)	7322-7429 cal BP (100 %)
	44.1	9133-9184 cal BP (38 %) 9194-9278 cal BP (62 %)	9032-9051 cal BP (3.7 %) 9089-9309 cal BP (91.2 %) 9366-9400 cal BP (5.1 %)
699	48.9	9483-9527 cal BP (100 %)	9458-9536 cal BP (100 %)
	71.7	11227-11281cal BP (80.5 %) 11289-11313cal BP (19.5 %)	11204-11349 cal BP (94.5 %) 11373-11393 cal BP (5.5 %)
	84.5	11834-11854 cal BP (8.3 %) 11875-12004 cal BP (82.2 %)	11768-11772 cal BP (0.1 %) 11816-12104 cal BP (92.3 %)

doi:10.6342/NTU202302306

		12017-12041 cal BP (9.6 %)	12118-12170 cal BP (3 %) 12239-12249 cal BP (0.5 %) 12309-12322 cal BP (0.6 %) 12395-12433 cal BP (3.5 %)
700	48.6	9037-9045 cal BP (4.6 %) 9124-9151 cal BP (19.7 %) 9168-9272 cal BP (75.7 %)	9027-9061 cal BP (9.2 %) 9079-9293 cal BP (90.4 %) 9389-9393 cal BP (0.5 %)
	56.3	9760-9909 cal BP (85.2 %) 10075-10110 cal BP (14.8 %)	9695-9960 cal BP (81 %) 9990-10011 cal BP (3.1 %) 10025-10039 cal BP (1.5 %) 10063-10122 cal BP (14.4 %)
	60.6	10447-10450 cal BP (2.5 %) 10499-10574 cal BP (97.5 %)	10413-10468 cal BP (17.1 %) 10481-10590 cal BP (78.5 %) 10624-10650 cal BP (4.4 %)
	63.5	10722-10795 cal BP (44.3 %) 10857-10863 cal BP (2.6 %) 10964-11005 cal BP (28.9 %) 11029-11066 cal BP (24.2 %)	10697-10876 cal BP (52.2 %) 10945-11072 cal BP (47.8 %)
	79.9	11344-11375 cal BP (15.5 %) 11392-11408 cal BP (7.8 %) 11426-11502 cal BP (40.2 %) 11531-11607 cal BP (36.5 %)	11283-11295 cal BP (1.2 %) 11306-11641 cal BP (95.8 %) 11670-11689 cal BP (3.1 %)

doi:10.6342/NTU202302306

Appendix 2 Legend. The smooth window with 1 cm and 10 cm are represented by yellow line and blue line. The color gradient from light to dark orange is used to represent the gradation from fine to coarse grain sizes. The sediment is classified into the following categories: clay, silt, the combination of Vfs and Fs, and grain sizes larger than Ms. In addition, the red-colored blocks represent floodplain, the deep yellow-colored blocks represent fluvial channels, the light green-colored blocks represent tidal creeks, the blue-colored blocks represent marshes, the light blue-colored blocks represent lagoons, the orange-colored blocks represent tidal flats, the yellow-colored blocks represent washover fans, and the purple-colored blocks represent tidal inlets.

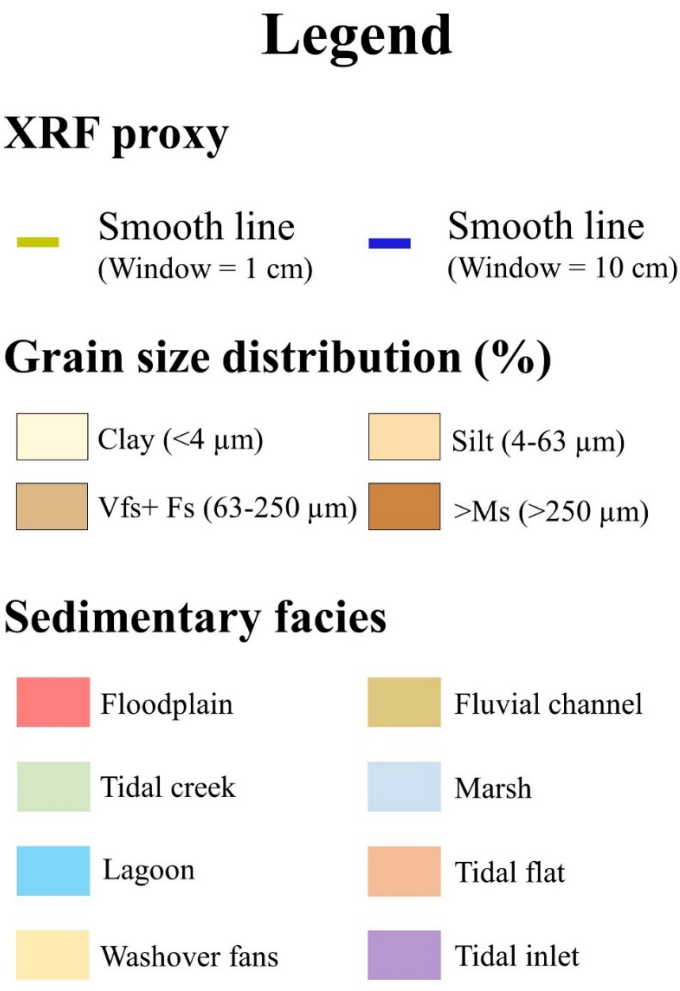

doi:10.6342/NTU202302306

Appendix 3 Sedimentary facies of Core 690 (0-25 m). From left to right, the columns represent the AMS ^{14}C dating results, lithology, lithofacies code, Log(Ca/Ti), Log(Zr/Rb), grain size distribution, TOC (%), TOC/TN, and the color blocks of sedimentary facies.

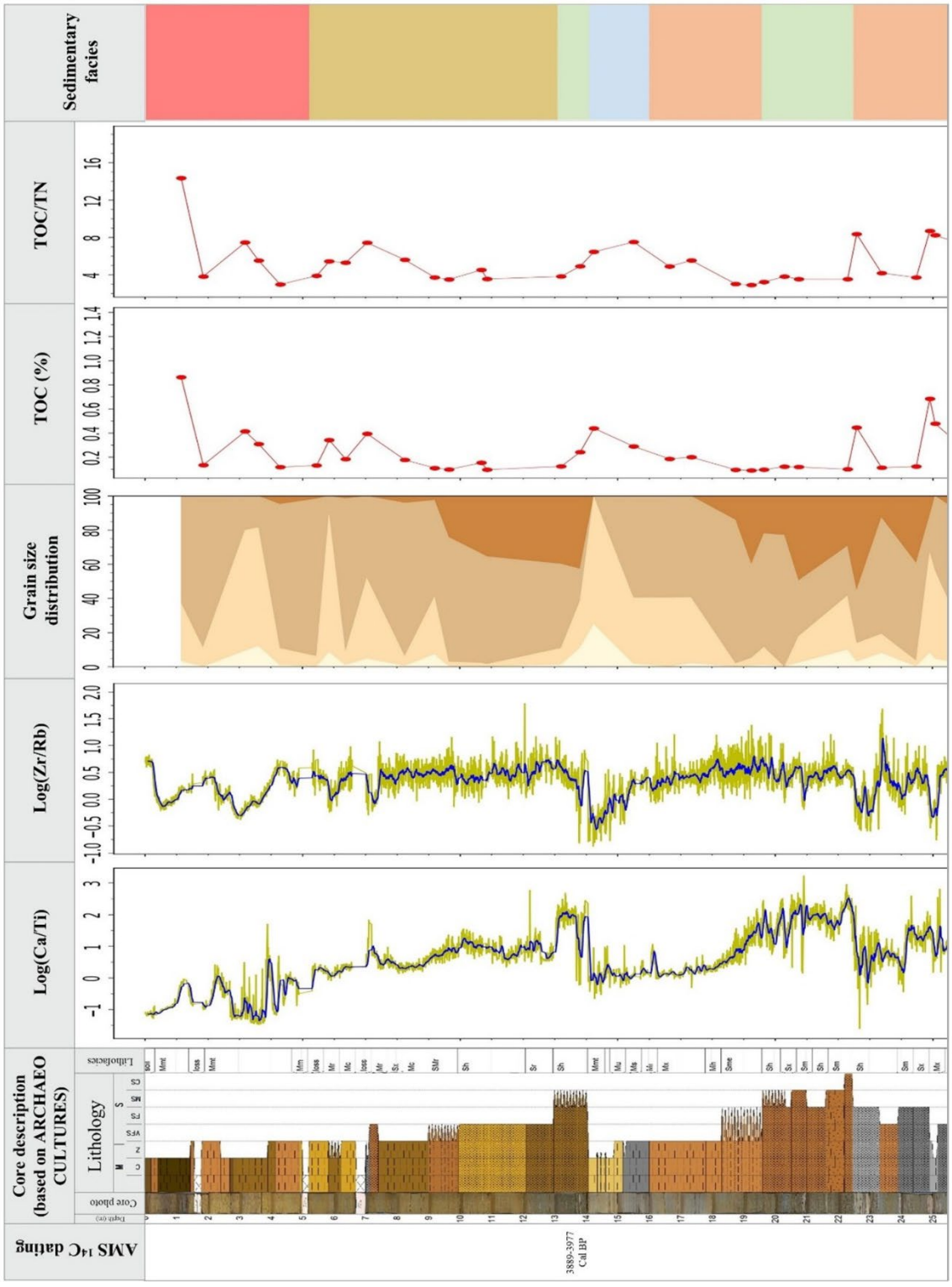

doi:10.6342/NTU202302306

Appendix 4 Sedimentary facies of Core 690 (25-50 m). From left to right, the columns represent the AMS ^{14}C dating results, lithology, lithofacies code, Log(Ca/Ti), Log(Zr/Rb), grain size distribution, TOC (%), TOC/TN, and the color blocks of sedimentary facies.

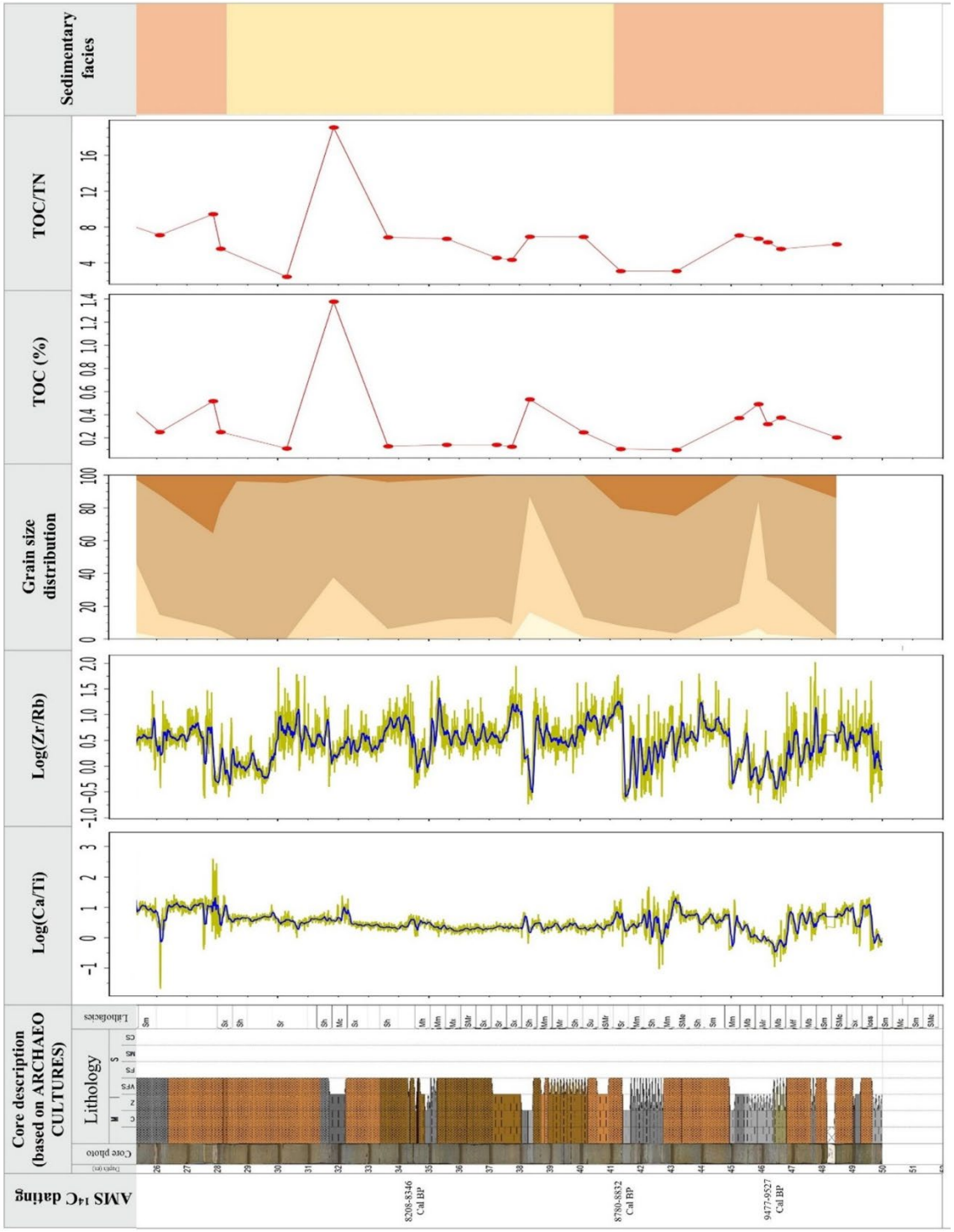

doi:10.6342/NTU202302306

Appendix 5 Sedimentary facies of Core 691 (0-25 m). From left to right, the columns represent the AMS ^{14}C dating results, lithology, lithofacies code, Log(Ca/Ti), Log(Zr/Rb), grain size distribution, TOC (%), TOC/TN, and the color blocks of sedimentary facies.

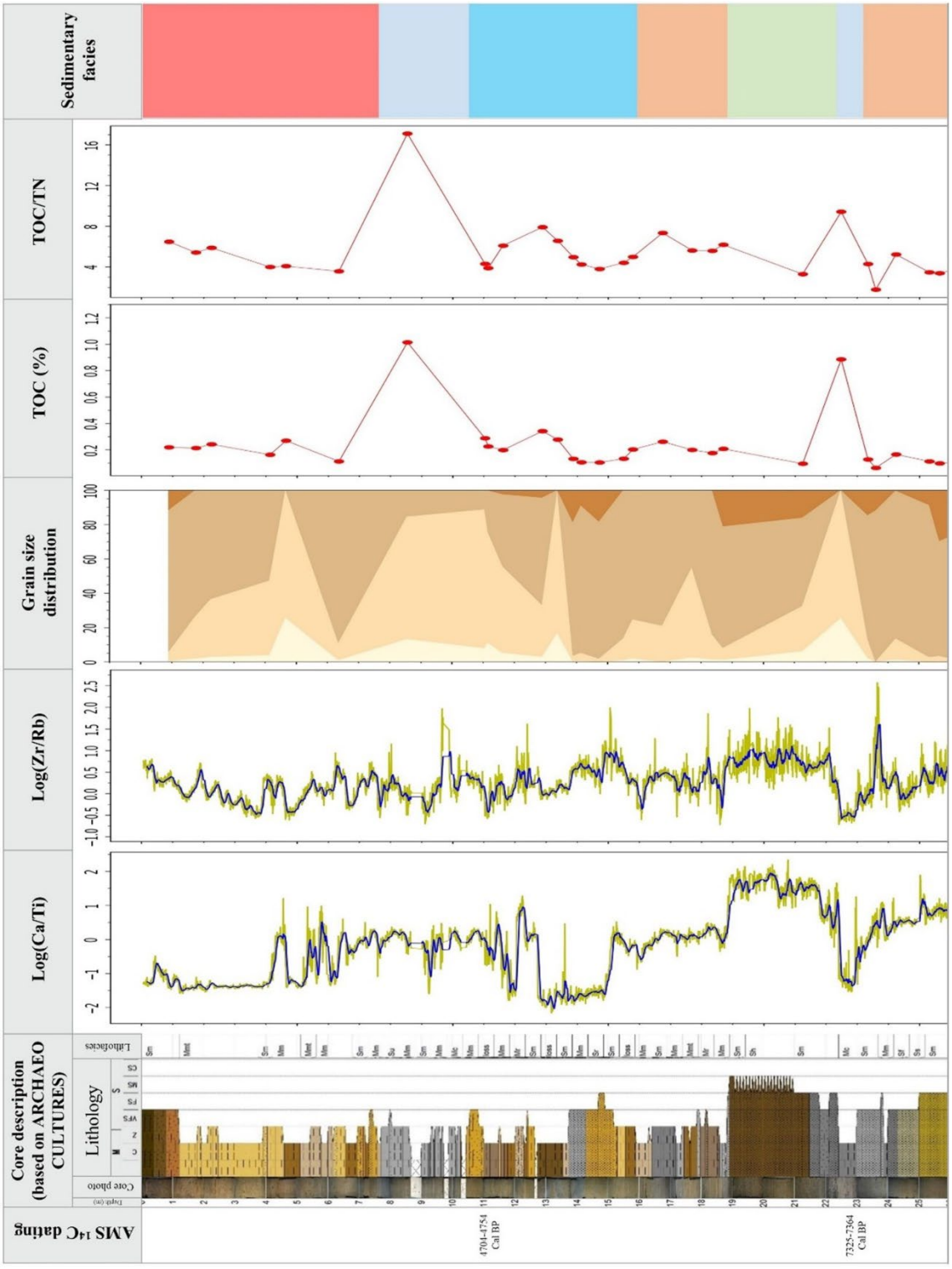

doi:10.6342/NTU202302306

Appendix 6 Sedimentary facies of Core 691 (25-50 m). From left to right, the columns represent the AMS ^{14}C dating results, lithology, lithofacies code, Log(Ca/Ti), Log(Zr/Rb), grain size distribution, TOC (%), TOC/TN, and the color blocks of sedimentary facies.

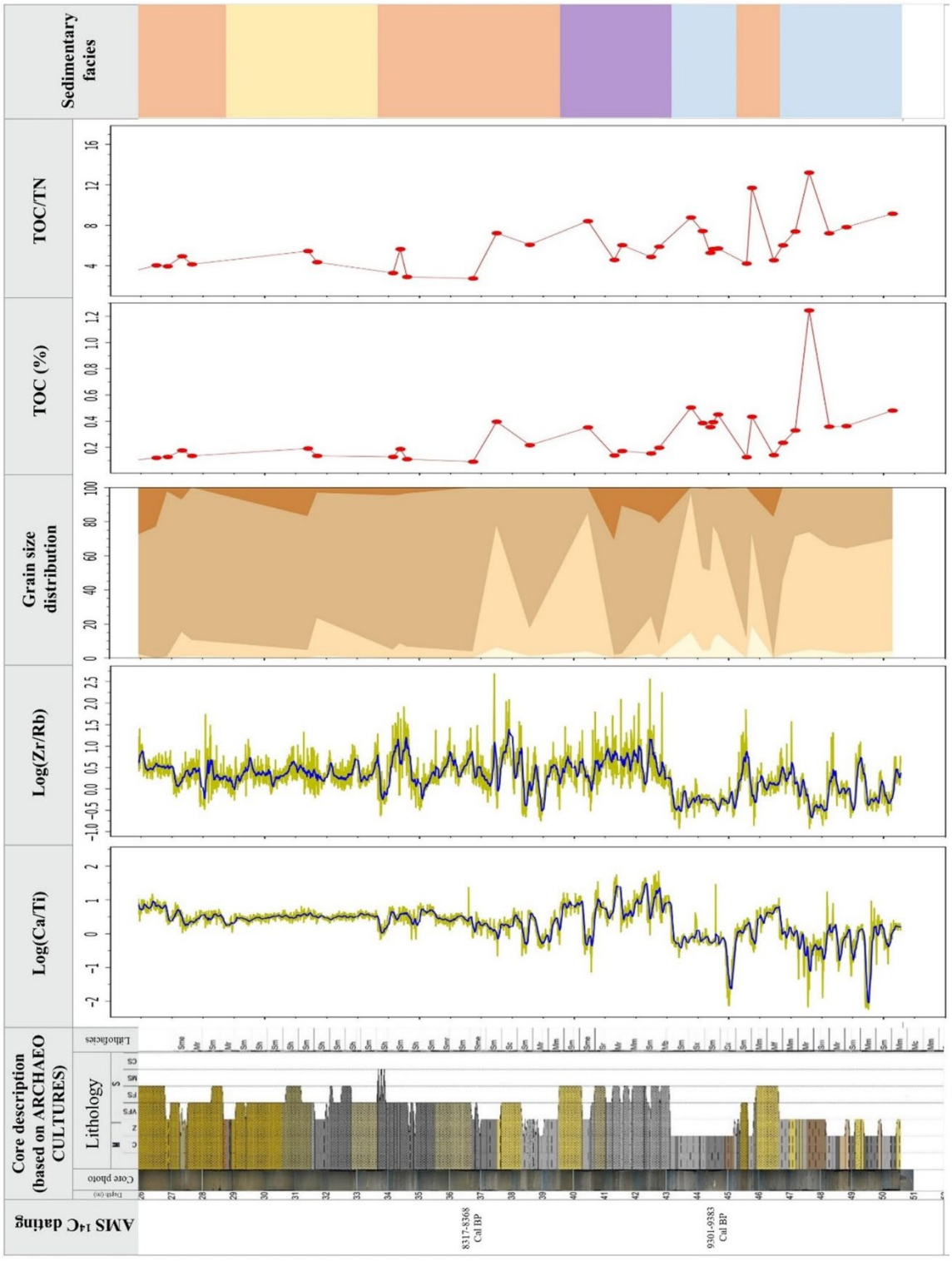

doi:10.6342/NTU202302306

Appendix 7 Sedimentary facies of Core 692 (0-25 m). From left to right, the columns represent the AMS ^{14}C dating results, lithology, lithofacies code, Log(Ca/Ti), Log(Zr/Rb), grain size distribution, TOC (%), TOC/TN, and the color blocks of sedimentary facies.

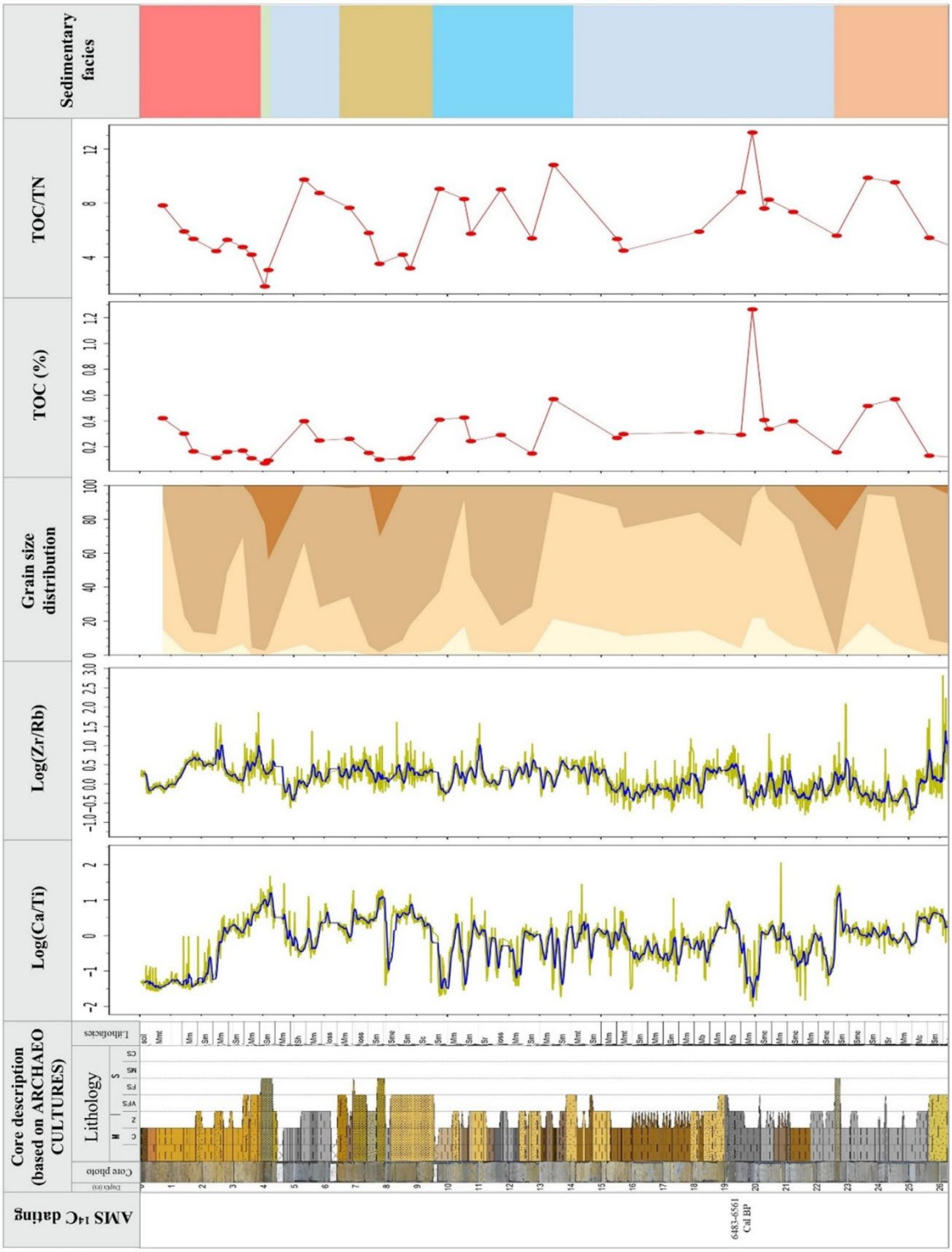

doi:10.6342/NTU202302306

Appendix 8 Sedimentary facies of Core 692 (25-50 m). From left to right, the columns represent the AMS ^{14}C dating results, lithology, lithofacies code, Log(Ca/Ti), Log(Zr/Rb), grain size distribution, TOC (%), TOC/TN, and the color blocks of sedimentary facies.

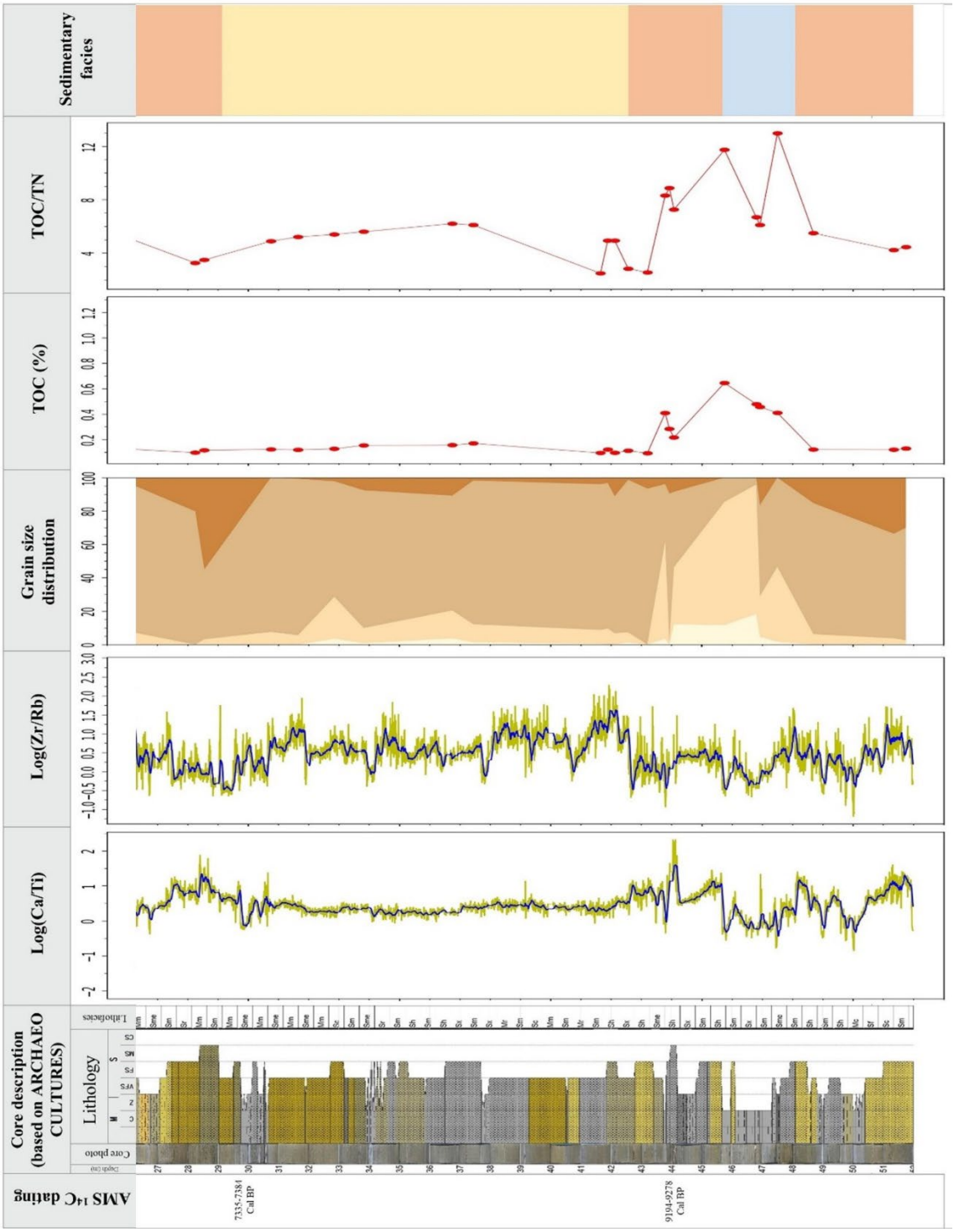

doi:10.6342/NTU202302306

Appendix 9 Sedimentary facies of Core 699 (0-50 m). From left to right, the columns represent the AMS ^{14}C dating results, lithology, lithofacies code, Log(Ca/Ti), Log(Zr/Rb), grain size distribution, TOC (%), TOC/TN, and the color blocks of sedimentary facies.

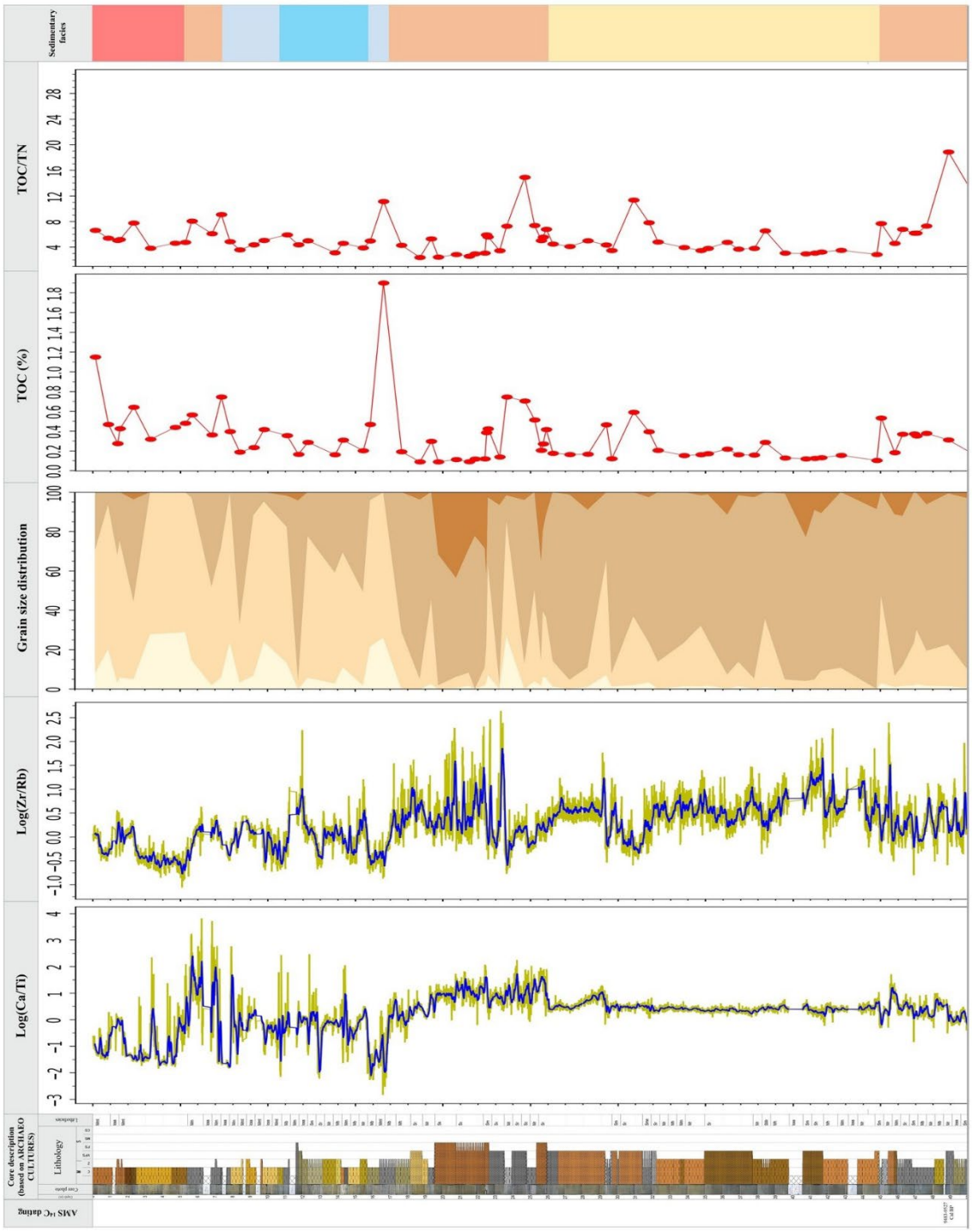

doi:10.6342/NTU202302306

Appendix 10 Sedimentary facies of Core 699 (50-100 m). From left to right, the columns represent the AMS ^{14}C dating results, lithology, lithofacies code, Log(Ca/Ti), Log(Zr/Rb), grain size distribution, TOC (%), TOC/TN, and the color blocks of sedimentary facies.

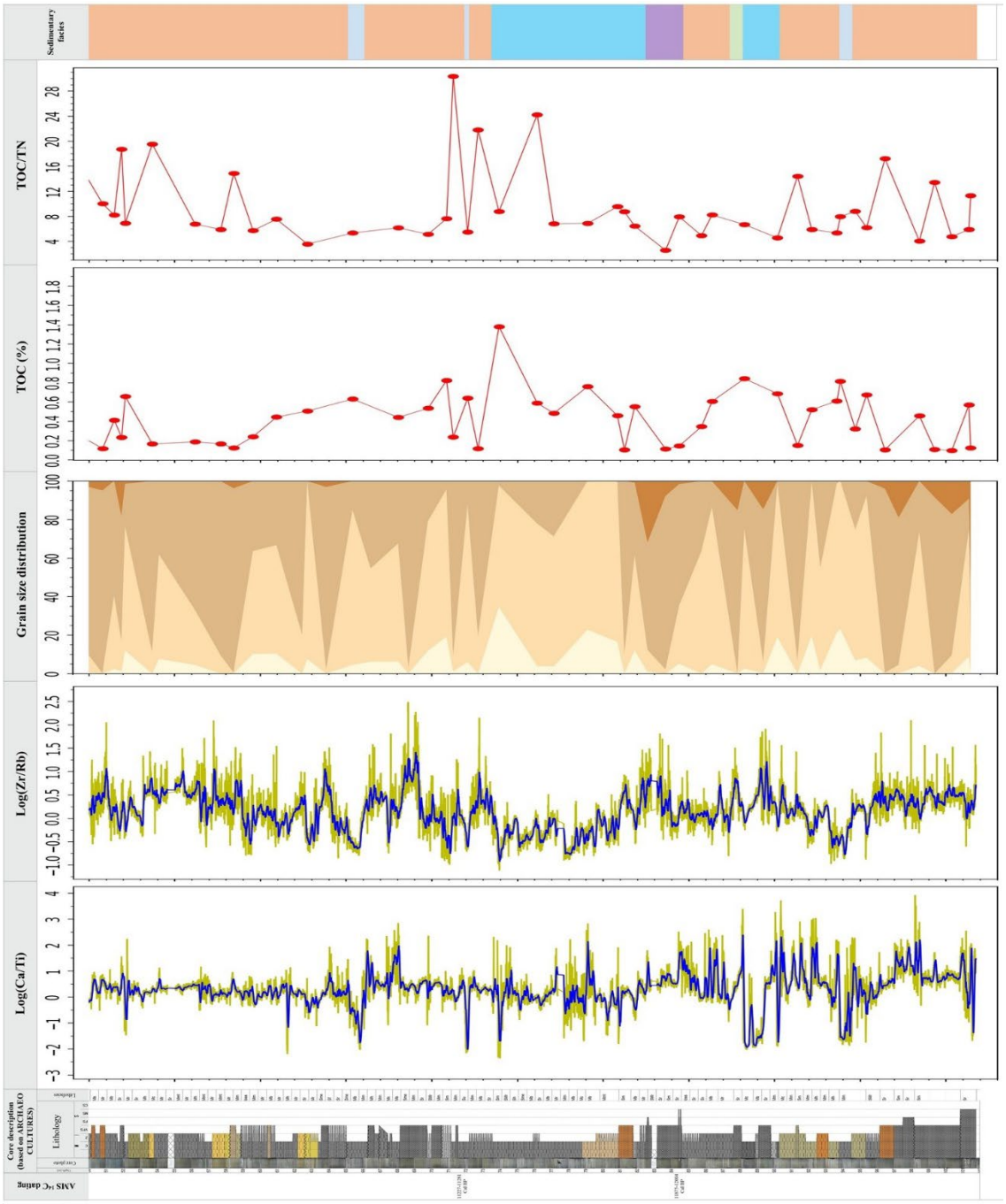

doi:10.6342/NTU202302306

Appendix 11 Sedimentary facies of Core 700 (0-50 m). From left to right, the columns represent the AMS ^{14}C dating results, lithology, lithofacies code, Log(Ca/Ti), Log(Zr/Rb), grain size distribution, TOC (%), TOC/TN, and the color blocks of sedimentary facies.

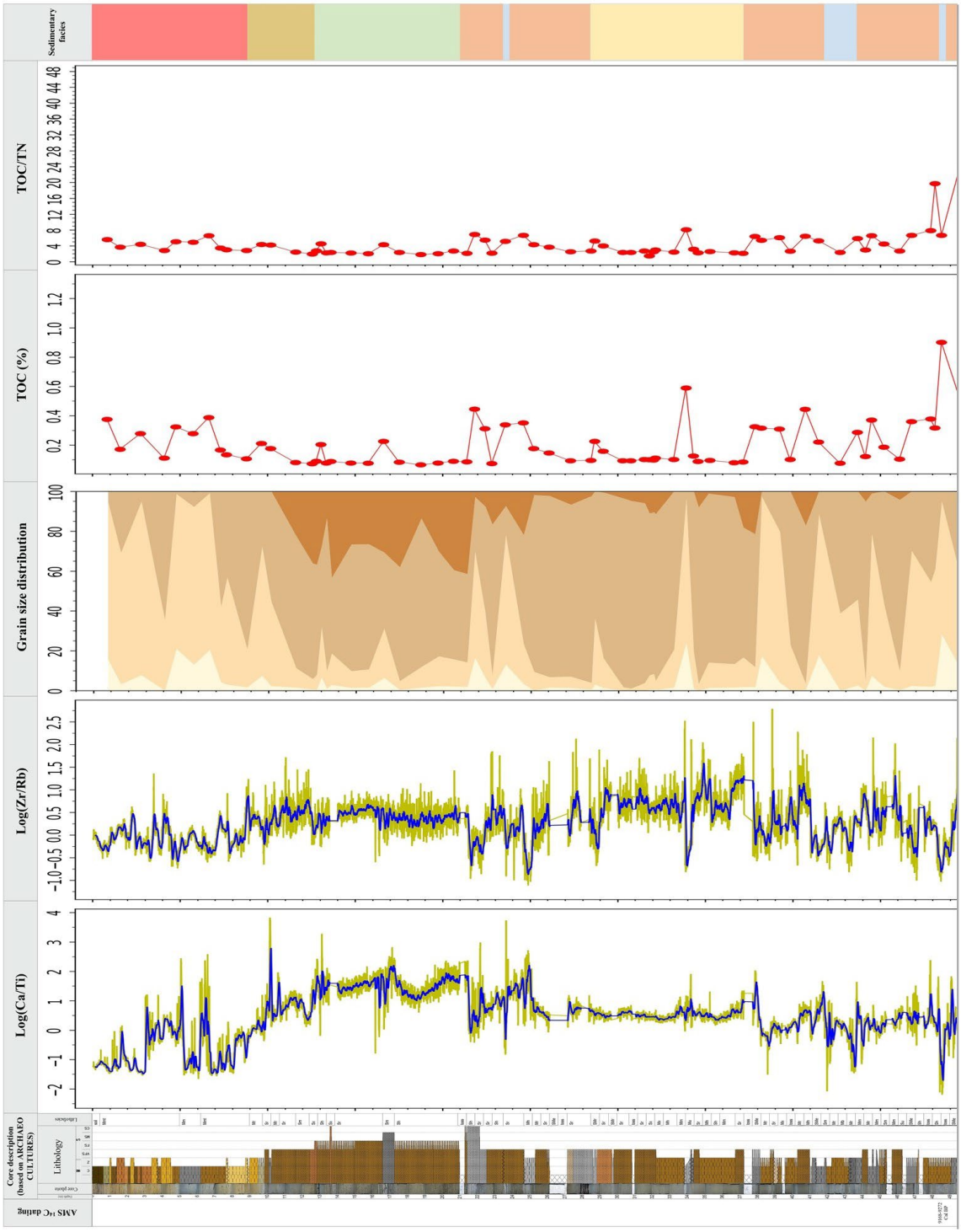

doi:10.6342/NTU202302306

Appendix 12 Sedimentary facies of Core 700 (50-100 m). From left to right, the columns represent the AMS ^{14}C dating results, lithology, lithofacies code, Log(Ca/Ti), Log(Zr/Rb), grain size distribution, TOC (%), TOC/TN, and the color blocks of sedimentary facies.

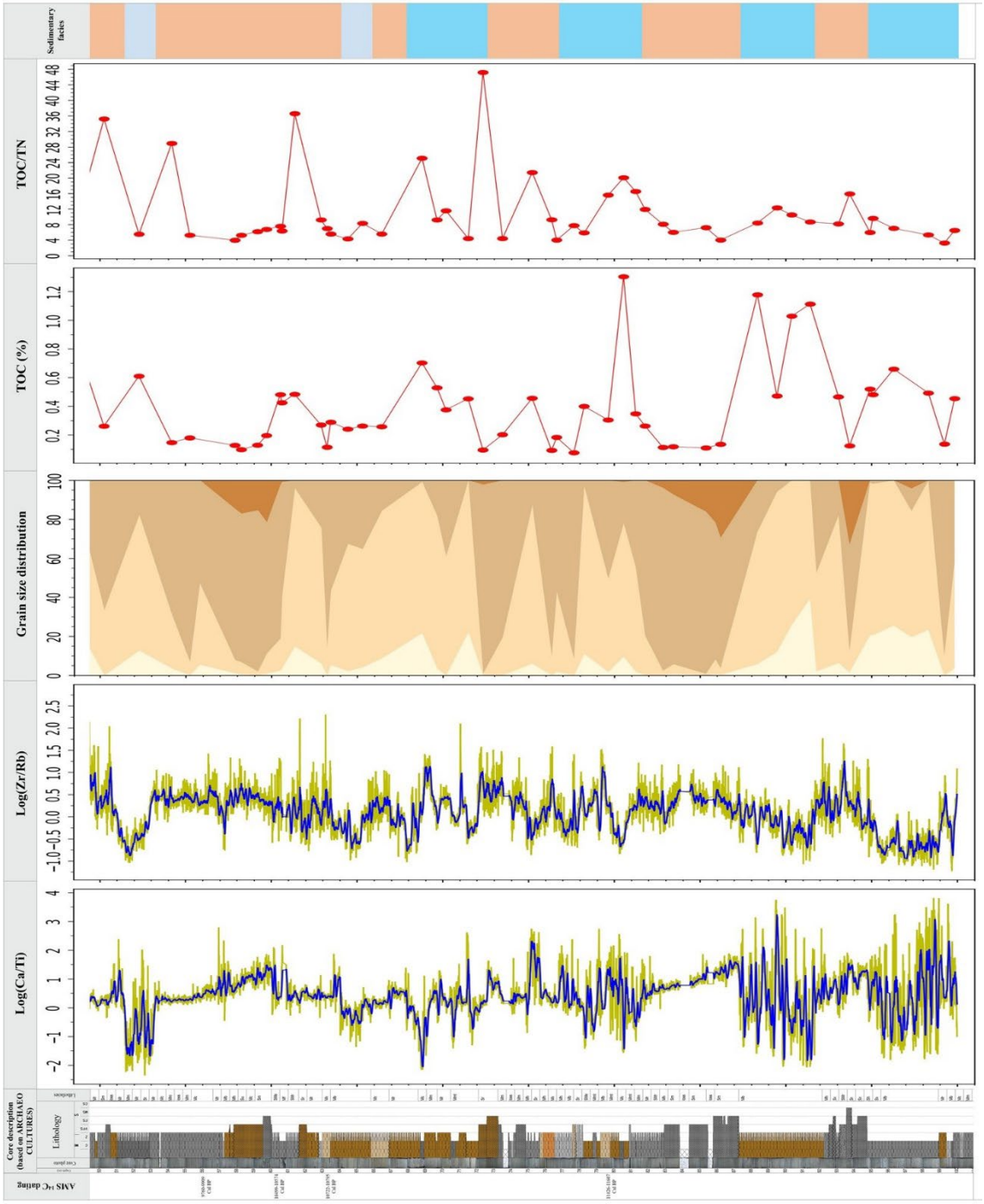

doi:10.6342/NTU202302306

Appendix 13 QR code of research data

doi:10.6342/NTU202302306